UNIVERSITAT DE BARCELONA

# Holographic optical tweezers systems for biophysical experiments

Jordi Andilla i Salla

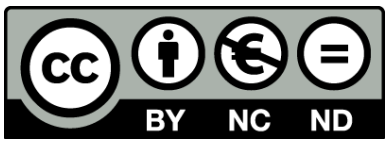

Universitat de Barcelona
Departament de Física Aplicada i Òptica
Programa de doctorat Tècniques instrumentals de la Física i la Ciència de Materials
Bienni 2002/2004

# Holographic Optical Tweezers Systems for Biophysical Experiments

Memòria de tesi presentada el Desembre de 2008 per
Jordi Andilla i Salla
per optar al títol de Doctor en Física.
Dirigida per la Dra. Estela Martín Badosa i el Dr. Mario Montes Usategui

# Pròleg

## Resum del treball en català

La tècnica de les pinces òptiques (optical tweezers) ha estat i és en l'actualitat àmpliament utilitzada en nombrosos camps científics per la seva capacitat de manipulació de partícules microscòpiques, així com per la possibilitat de mesurar la força aplicada en aquesta manipulació. El seu rang d'aplicació està comprès entre les desenes de micres i el centenar de nanòmetres pel que fa a la mida de les partícules, i en l'ordre dels centenars de pico-Newtons pel que fa a les forces màximes aplicades i mesurades. Aquest rang d'aplicació ha donat a aquesta tècnica una rellevància notable, doncs en aquests ordres de magnitud es donen molts processos en l'entorn de la biologia molecular. Les pinces òptiques han permès, per exemple, mesurar la força realitzada per motors moleculars o determinar les propietats mecàniques de bio molècules, com per exemple l'elasticitat de l'ADN o la força necessària per l'encapsulament del material genètic d'un virus.

L'evolució de la tècnica, des que va ser presentada per Artur Ashkin el 1970 fins a l'actualitat, ha estat constant i en diferents fronts. La tècnica, originalment presentada utilitzant dos feixos de llum contraposats, va ser simplificada utilitzant un sol feix però altament focalitzat. L'interès en la manipulació de les partícules, així com la possibilitat de treballar simultàniament amb més d'un objecte, ha provocat la introducció de diferents elements en el disseny original de les pinces òptiques, com per exemple miralls rotatoris, moduladors acusto-òptics, o pantalles de cristall líquid (LCD). El potencial de la tècnica ha arribat a suscitar l'interès d'empreses que comencen a oferir sistemes de pinces òptiques que poden ser incorporats directament en microscopis comercials.

En l'actualitat, existeix una tendència en augmentar el grau de complexitat dels experiments de pinces òptiques, sent necessari, en cada cas, un sistema experimental específic. El treball que presentem en aquesta memòria, explora la possibilitat d'aplicar la tècnica de les pinces òptiques hologràfiques com a sistema universal de manipulació tridimensional de múltiples objectes microscòpics. Bàsicament, un sistema de pinces hologràfiques consisteix en un làser expandit per un telescopi, per il · luminar un LCD que modifica el feix per mitjà d'un holograma de fase. Aquest feix és reduït per un segon telescopi a la mida de la pupil · la

de sortida d'un objectiu de microscopi d'alta apertura numèrica; aquest objectiu forma la trampa en el pla de la mostra a la vegada que serveix per visualitzar-la.

L'estudi comença amb la caracterització de la modulació de les LCDs utilitzades en la generació de trampes òptiques hologràfiques. Hem desenvolupat un sistema de caracterització automàtic en termes del formalisme de les matrius de Jones, que ens permet trobar la configuració de modulació de fase, utilitzada habitualment en la generació de patrons de trampes hologràfiques. Les LCD utilitzades en aquest treball (Holoeye LC-2500R i Hamamatsu X10468-3) són del tipus LCoS (Liquid Crystal on Silicon) i funcionen per reflexió. La curvatura de la superfície de la pantalla introdueix aberracions al sistema que modifiquen la forma de la trampa òptica resultant, disminuint la seva capacitat d'atrapament. Hem determinat la curvatura del Holoeye LC-2500R utilitzant dos mètodes diferents. En primer lloc, s'ha comprovat que l'aberració de la part central de la pantalla es pot entendre com a astigmatisme de primer ordre i s'ha corregit afegint la fase d'una lent toroïdal al modulador. El segon mètode, més acurat, consisteix en utilitzar un mesurador de front d'ona Shack-Hatmann per trobar la curvatura de tota la superfície de la LCD, i corregir-la fins a valors de $\lambda/16$.

Les dues LCDs esmentades han estat utilitzades, amb les seves longituds d'ona respectives ($532\,nm$ i $1064\,nm$), en els sistemes de pinces òptiques hologràfiques, dissenyats i construïts en base a dos models diferents de microscopis comercials: un Motic AE31 amb un objectiu d'immersió en oli de $1.25NA$, i un Nikon TE2000, amb un objectiu de $1.3NA$ d'immersió en oli i un de $1.25NA$ d'immersió en aigua. Amb aquests sistemes s'han pogut atrapar i manipular simultàniament vàries microesferes de poliestirè de mides compreses entre els $200\,nm$ i els $5\,\mu m$ de diàmetre. L'efecte de les característiques òptiques de cada element del sistema, així com les seves posicions, ha estat simulat numèricament per tal d'analitzar els factors més rellevants en la qualitat de les trampes òptiques resultants. Hem comprovat que l'efecte de les aberracions introduïdes pel sistema expansor són més importants que en el cas del sistema reductor. La simulació numèrica de l'objectiu d'immersió en aigua en el rang de l'infraroig ens ha permès comprovar que l'efecte del canvi de valor de l'índex de refracció de les diferents lents que el composen, no perjudica la qualitat de les trampes, tot i que l'objectiu està corregit per longituds d'ona visible. S'obtenen trampes en el límit de difracció en profunditats en la mostra de fins a $270\,\mu m$. De totes maneres, trobem un petit canvi en la posició del pla d'enfocament respecte el visible, que ha de ser corregit per tal que el pla de visualització de la mostra amb què treballem i el pla d'enfocament de les pinces òptiques coincideixin.

Hem programat i estudiat les característiques dels algoritmes de Gerchberg-Saxton, de lents i prismes, i de màscares aleatòries, per el càlcul d'hologrames per generar patrons de trampes arbitraris. L'algoritme de Gerchberg-Saxton requereix un gran temps de càlcul, però proporciona una eficiència energètica en el patró de trampes elevada. D'altra banda, el mètode de màscares aleatòries proporciona una velocitat de càlcul elevada però l'eficiència energètica es

veu reduïda. Per últim, el mètode de lents i prismes està a mig camí dels dos anteriors però té el problema afegit per patrons amb simetries que donen efectes indesitjats en el resultat. Els algoritmes de les màscares aleatòries i el de lents i prismes han estat implementats en un programa que permet la generació i control de la posició en temps real de la posició de les trampes en les tres dimensions. Aquesta interfície incorpora un sistema que permet clicar sobre la imatge de la mostra per posicionar la trampa i moure-la de manera interactiva.

Per últim, el nostre sistema de pinces òptiques hologràfiques ha estat adaptat per tal de realitzar experiments en els terrenys de la biologia cel · lular i molecular. En el cas de biologia cel · lular, hem establert i mantingut, durant mesos, una línia cel · lular del tipus NG-108. Hem modificat els protocols de cultiu, congelació i descongelació per tal d'adaptar-los als medis i característiques pròpies del laboratori de cultiu cel · lular dels Serveis Cientificotècnics de la Universitat de Barcelona. Hem construït un equipament especial que manté la temperatura, humitat i pH de la mostra, possibilitant la interacció amb les pinces òptiques quan es treballa en el microscopi durant hores. Hem creat nous protocols per tal de transportar les cèl · lules des del laboratori de cultiu fins al laboratori òptic sense danyar-les.

Hem utilitzat el sistema en l'estudi del transport intracel · lular en cèl · lules vives. Hem utilitzat la interfície de control per generar una trampa òptica sobre una vesícula transportada per un motor molecular i aturar el seu moviment. A partir d'un resultat previ presentat per Ashkin, hem pogut estimar la força que és capaç d'exercir el motor molecular atrapat, en desplaçar la vesícula. Amb aquest resultat ens permet suposar que el motor molecular que movia la vesícula era una dineina citoplasmàtica.

Per últim, hem reproduït un experiment d'estirament de molècula individual per estudiar les propietats elàstiques de la molècula d'ADN, utilitzant el sistema de pinces òptiques hologràfiques. La concordança amb les dades obtingudes amb experiments no hologràfics demostra que les pinces hologràfiques poden ser utilitzades en aquest tipus d'experiments. En el futur caldrà millorar alguns aspectes del nostre sistema com l'estabilitat temporal de les trampes i avaluar la seva precisió.

# Contents

# Chapter 1

# Introduction

Long time ago humans acquired the capability to manipulate objects and surrounding environment to improve their way of life. This capability is the basis of technology. Technological discoveries helped humans in controlling their environment and every invention or discovery increased the global knowledge. That knowledge also contributed to the generation of new innovations. This cycle was repeated again and again along time following intricate paths and sometimes taking unexpected directions. As in the particular case of this work: when in November of 1957 laser was invented, probably, neither Gould, Schawlow nor Townes would have imagined that nowadays their invention became the basis to study the structure and behavior of cells or bio-molecules by using optical tweezers. Every small step along this path from laser to optical tweezers contributed to reach that surprising outcome. The work presented below is our small and modest contribution to that development.

## 1.1 Historical context

It is usually considered that the beginning of optical tweezers is related to observations of the comet's tail deflection by Johannes Kepler in the early 17th century [Ash72]. Kepler theorized that the radiation pressure of light makes the comet's tail point away from the sun. Two centuries later, in 1871, James Clerk Maxwell published his famous equations from where the radiation pressure effect can be derived. This effect, due to the small forces generated, could not be shown in a controlled experiment until very early in the 20th century thanks to Piotr Lebedev. Unfortunately, technology of the moment was not ready to make a real use of this result. We have to wait until the decade of 70's to find real applications of this interesting property of light and matter. Space race between the Soviet Union and the United States started in 1957 with the launch of Sputnik 1. On a parallel track, in 1960, the first working laser was demonstrated. These two independent events are curiously related with another two events that also occurred close in time and are related with the radiation pressure effect. The robotic space probe Mariner 10 was launched in 1973. NASA successfully used radiation pressure to control the motion of the probe by tilting its solar

panels [nas78]. It was the first time when light pressure was used to modify the attitude of a space probe. This concept had been used long time ago by science fiction authors to navigate with solar sails around the universe without any fuel consumption.

Laser appearance opened a wide field of new technologies used in industry, multimedia or in science environments and Arthur Ashkin, who is considered the father of optical tweezers, reported in 1970 acceleration of micro-sized particles using the force of radiation pressure from a continuous focused laser beam [Ash70]. Acceleration produced by the laser beam was enough to obtain levitation of micro spheres. In this paper it is also presented the first counter-propagating optical trap consisting of two focused beams facing each other. In the region of the beam's focus, micro-sized beads could be trapped.

In 1986, Ashkin again [ADBC86] reported optical trapping of micro-sized dielectric particles by a single laser beam. In this case, the dielectric particles were trapped because of the negative pressure exerted by light when passing through the particle (see section 2.1.1 for details). This greatly simplified the original setup enabling the direct adaptation into standard microscopes. One year later, the application of optical forces to trap viruses and bacteria [AD87], as well as single cells [ADY87], were presented. These two papers demonstrated not only the capability to trap cells, viruses, bacteria or organelles within cells: use of infrared (NdYAG:1064nm) lasers to generate the optical trap avoided the destruction of biological objects, opening the possibility to use optical tweezers in microbiology.

Following this trend, a few years later S. Block [Blo90] discussed optical tweezers as a full-hedged biophysical technique. His article does an exhaustive review of optical trapping techniques and suggests the capability to quantify the mechanical forces exerted by molecular motors. In parallel, Ashkin *et al.* presented the measurement of the force generated by a molecular motor when transporting an organelle [ASD$^+$90]. This force was calculated determining the minimal optical force needed to stall the organelle transport. Another example was presented in 1993 by Kuo and Sheetz in [KS93]; they directly measured the pulling force of a single kinesin molecule using the same technique. These experiments were the beginning of a long series of studies of physical properties of bio-molecules. In order to obtain more precision in these experiments and to be able to corroborate theoretical models, new techniques were developed. By use of an interferometric technique based on Nomarski microscopy, Svoboda *et al.* [SSSB94] demonstrated small steps in kinesin movement. In the same vein, Finer *et al.* [FSS94] used the deflection of the laser beam when passing through a dielectric particle to determine the force exerted by the trap. However, this method was not completely understood until 1998, when Gittes and Schmidt [GS98] gave a theoretical explanation.

The basic feature of optical tweezers is obviously its trapping capability. Therefore, if a trap is gradually moved, the trapped particle will move too. This possibility enables this technology to manipulate micro-sized objects without mechanical contact. It is easy to see

that by tilting the laser beam with respect to the focusing lens, displacements of the final trap can be obtained. Going a step backward and looking at S. Block paper [Blo90] we can find several ways to tilt the beam by means of moving lenses, rotating mirrors or by inserting acousto-optic deflectors into the system. In 1992, Misawa *et al.* [MSK+92] extended standard optical tweezers obtaining a dual trap system. The idea consisted on splitting up a single beam into two beams. Each beam was manipulated separately by an independent pair of galvanometric mirrors. Finally, the beams were joined again into the same optical path, achieving two separate traps steered independently. Later, this concept was expanded by Visscher *et al.* [VBK93] using a pair of steerable mirrors to move a single beam through different positions and an acousto-optic modulator as a fast beam shutter to select the positions of the desired traps. This technique allows generation of multiple traps, but the drawback is that light is present in each position only for a certain period of time. An alternative to the galvanometric mirrors were the acousto-optic deflectors. These devices were used to steer single traps [SFCS96] and also divide the beam [VGB96] in a similar way to Visscher's proposal, but without mechanical movements. In [GTDW04] a highly improved system was presented to obtain up to six traps with laser refreshment frequencies of around 10kHz. The main limitation of these systems is that steering of optical traps can be done only in two dimensions. In order to overcome this constraint a telescope can be added to modify the focus position of the final trap. Fällman and Axner [FA97] presented a combined idea to obtain a fully steerable dual optical tweezers system. It consisted in splitting a beam, as presented in [MSK+92], and adding two adjustable independent telescopes in each beam path to control the focus of the traps. The combination of these strategies can introduce new features to optical tweezers systems to perform particular experiments. As a recent example, Noom *et al.* [NBMW07] combined acousto optical deflectors with beam splitting and telescopes to obtain four fully 3D steerable optical traps. However, the complexity of these systems clearly limits the possibility to expand them to a large number of traps.

To obtain multiple traps, diffractive optical elements can be added into the beam path as an alternative method to split the beam. Diffractive elements are thin phase plates that operate by means of interference and diffraction to produce arbitrary distributions of light. These elements can generate arrays of traps without any time sharing [DG98]. Once again an important limitation exists: diffractive optical elements are static elements; arbitrary complex patterns of light can be created but, the whole element must be changed to modify the shape of the pattern.

In order to obtain dynamic capabilities and non-shared traps, Reicherter *et al.* [RHWT99] used a Liquid Crystal Device (LCD) as a phase modulator. Similarly to diffractive elements, LCDs can modify the phase of light to obtain the desired pattern of traps. The most important difference with diffractive elements is that LCDs can be easily programmed and updated dynamically by means of computer control [HST97]. The technology consisting in combining digital holography with optical tweezers systems is known as holographic optical tweezers. Its main disadvantage is the large computational cost to generate the holograms. LCDs and

optical tweezers have also been successfully combined to steer multiple optical traps using a different technology: Eriksen *et al.* [EDG02] used a generalized phase contrast method to generate trap patterns. The method uses an LCD to modify the phase of light and, then, by using a phase contrast filter, the phase modification is converted into an intensity pattern which is sent to the sample plane through the microscope objective to obtain the desired trap pattern. This is a direct method, no computation is needed, but it can only generate two-dimensional trap patterns.

Until now only a standard Gaussian beam (TEM00) has been considered, but there are many other types of beams that can be used. Because of their interesting properties, Laguerre-Gaussian beams [LYC04] or Bessel beams [AGCSD01] may be created by introducing special phase plates into the beam path. With this kind of beams the application possibilities of optical trapping increase. In the case of Laguerre-Gaussian beams the generated trap has a doughnut-like shape that transfers angular momentum to the trapped particle. For the Bessel beam the trap becomes invariant along the optical axis within a certain distance, producing an elongated trap in the axial direction. Due to their capabilities, LCDs are often used to dynamically generate these special beams. As an example, Curtis *et al.* [CKG02] used computer-generated holograms displayed on an LCD to obtain multiple Laguerre-Gaussian traps at different positions simultaneously and also combined with standard optical traps.

Optical tweezers technology would not stir up this notable interest without its force measurement capability. In the same way as atomic force microscopes or magnetic tweezers, optical tweezers may be used as tools to study properties, behaviors, or characteristics of micro-sized objects. Variations of light's momentum are directly related to the applied force and can be measured by analyzing the light refracted by the sample. The work presented by Gittes and Schmidt [GS98] demonstrated that if a single trap is used and the trapped particle is spherical, the position of the center of mass of the interference pattern obtained in the back focal plane of the lens that collects the refracted light is linearly proportional to the optical force applied on the particle. This technique has been widely used and it has been greatly optimized. A problem arises when using multiple traps: the obtained interference pattern contains mixed information of several traps at the same time, making it useless to determine the force for each trap by determining the position of the center of mass of the pattern. In order to solve this problem Belloni *et al.* [BMMS08] recently presented an interesting technique based on video analysis that gives quite a good precision. They analyzed the image of the trapped beads instead of the interference pattern to determine the force applied by the trap.

Optical tweezers make possible the study of mechanical and structural properties of biopolymers at the single-molecule level. S.B. Smith *et al.* [SCB96] presented a method to study the elastic properties of DNA. Each end of a single DNA molecule was attached to a separate microscopic bead. The first bead was held by suction by means of a glass micropipette and the second one was held by an optical trap. Elastic forces exerted by the DNA

strand were determined by means of the deflection of the beam [FSS94]. Several studies have been performed using the same setup configuration, but studying RNA instead of DNA [CRJ+05] or other bio-molecules [SCB03]. D. E. Smith *et al.* [STS+01] studied a complex molecular motor that packs the DNA of bacteriophage $\phi$29 virus into its capsid, developing a large force ($\sim 50pN$), which would be used during the infection process. Substitution of the pipette by a second optical trap was proposed to improve this kind of experiments, increasing the mechanical stability of the setup [AGS+05] and thus its precision [MCI+06].

Another important field of study is cell mechanics and cell motility. Papers like [DS95] or [KSH+07] determined the force made by the cell when moving against a bead trapped by an optical trap. In these papers, the mechanism of neural growth cone motility when extending its lamellipodia or filopodia was studied. Optical tweezers can also be used for conditioning behaviors of growing cells. In [EBS+02], Ehrlicher *et al.* guided growth cones of neural cells. A similar experiment was performed by Burnham *et al.* [BWRM07], but leading fungi growth instead of neural growth.

Also, the manipulation capabilities of optical traps opened the possibility to study microscopic objects under controlled conditions. As an example, Ashkin and Dziedzic [ADY87] studied the division of a yeast cell when trapped by optical tweezers. Combination with other techniques such as fluorescence [DKM+04], confocal microscopy [VBK93], Raman spectroscopy [Pet07], microdissection [CEV97], or special fluorescence [CMVP07] have been successfully performed, and have added new interesting features to these technologies. Use of optical tweezers has also been proposed as an interesting way to control the micro-machinery that may be needed in micro-fluidics [Gri03]. For example, by using Laguerre-Gaussian beams an artificial micro-pump can generate a controlled flow [LWS+06]. A similar example can be found in [GO01], inducing angular momentum to micro-machinery to spin small wheels.

The relevance of optical tweezers from the first report by Ashkin in 1970 [Ash70] has grown steadily. Manipulation and force determination of micro-sized particles leaded this growth, but new technologies and applications to optimize the system, as well as design of new experiments, are currently promoting the development of optical tweezers. This relevance is shown in figure 1.1a, where we plot the number of articles at the Institute for Scientific Information (ISI) database with the topic "Optical Tweezers" from 1989 until now, and in figure 1.1b, where we can see the number of citations of two of the most important papers by Ashkin about optical tweezers.

## 1.2 Thesis outline

Many important processes in cell biology are mediated by complex bio-molecules. The 3D structure of these molecules is relevant to give them specialized functionality. Several experiments using atomic force microscopy or optical tweezers have been performed to study the properties of these structures in order to understand how these bio-molecules work. Recent

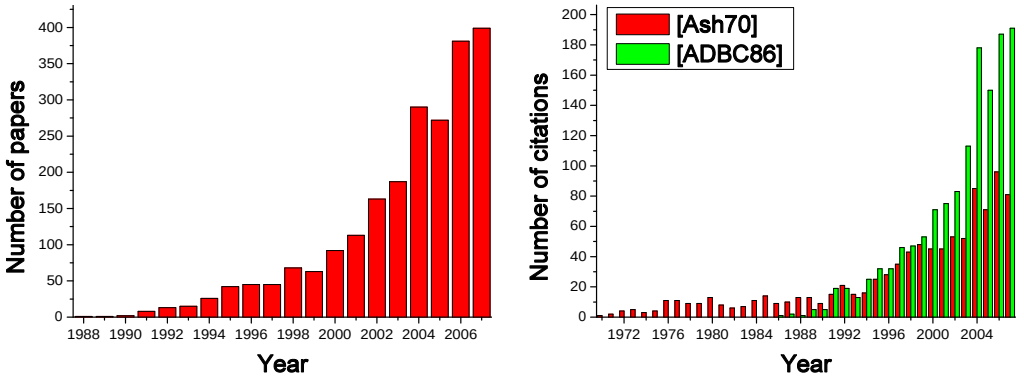


Figure 1.1: a) Number of articles about optical tweezers b) Number of papers citing Ashkin

experiments, as presented in [BSG+03] or [NBMW07], required a very complex strategy to succeed in their proposal. The first one required steering of three beads simultaneously and 3D manipulation. In the second one, control of four traps was necessary. Use of holographic optical tweezers, seems appropriate to open new possibilities or make experiments simpler. In this work, we present a holographic optical tweezers workstation with two possible configurations, being capable of performing experiments with alive mammalian cells and with single bio-molecules, respectively. It will be demonstrated that holographic tweezers are suitable to perform experiments in both fields. The study of the whole system is divided into four parts:

- Holographic modulation. Introduction of an LCD adds new features to the system, but also new constraints on the design, which are studied and evaluated. Use of LCDs requires calibration of the modulation response and flatness compensation to obtain high quality beams and traps, and high efficiency. This information must be included eventually in the computed hologram that will generate the trap pattern.

- Optical design. Many optical elements are used in a holographic optical tweezers setup. Analysis of the position and characteristics of these elements into the system is performed to improve the quality of holographic optical traps and its total efficiency. Finally, a complete simulation of the system including the actual characteristics of each element is provided and experimentally corroborated.

- Control, calibration and analysis software. An important part of the work presented here is the development of specific software to generate holograms which will produce the desired trap pattern at the sample. A custom interface has been designed to interact with them. The capabilities of this interface include real-time 3D manipulation, generation of multiple traps forming arbitrary patterns and generation of Laguerre-Gaussian beams. Other programs are also described, which have been developed to calibrate optical traps and record data from the experiment.

- Biological procedures and workstations. Maintenance of mammalian cell lines and DNA

manipulation on the microscope stage requires special equipment. Two special workstations have been designed adapted to a commercial inverted microscope, such that experiments with alive mammalian cells and individual DNA molecules can be performed, respectively. The adaptation of protocols for cells maintenance as well as the working protocol for the DNA experiment are described. Finally, experimental results of the study of the molecular motors involved in the vesicular transport inside living cells and DNA elastic forces are presented and discussed.

## 1.3 Dissertation structure

The structure of this dissertation is based on an article compilation. After the list of publications and communications to conferences, presented below, the theory involved in the whole work is described, giving details of the individual parts that form the system. This description is followed by the discussion about the results obtained with both workstations, and the dissertation ends with the conclusions of the work. The articles and proceedings are presented in the appendix, followed by the reference list.

### 1.3.1 Publications list

LCD calibration

1. J. Andilla, E. Martín-Badosa and S. Vallmitjana, (2008) "Prediction of phase-mostly modulation for holographic optical tweezers"; Opt. Commun., 281, 3786-3791
Impact factor 2007: 1.314

2. C. López-Quesada, J. Andilla and E. Martín-Badosa, (2008) "Correction of aberration in holographic optical tweezers using a Shack-Hartmann sensor"; Appl. Opt. Publish pending
Impact factor 2007: 1.701

Optical design

3. E. Pleguezuelos, J. Andilla, A. Carnicer, E. Martín-Badosa, S. Vallmitjana and M. Montes-Usategui, (2006) "Design of a low-cost interactive holographic optical tweezer system"; SPIE Proceedings, 6326, 63262Q-1/9

4. E. Martín-Badosa, M. Montes-Usategui, A. Carnicer, J. Andilla, E. Pleguezuelos and I. Juvells, (2007) "Design strategies for optimizing holographic optical tweezers set-ups"; J. Opt. A: Pure Appl. Opt., 9, S267-S277
Impact factor 2007: 1.752

Hologram computation algorithms

5. M. Montes Usategui, E. Pleguezuelos, J. Andilla and E. Martín-Badosa, (2006) "Fast generation of holographic optical tweezers by random mask encoding of Fourier components"; Opt. Express, 14, 2101-2107
Impact factor 2007: 3.709

6. M. Montes-Usategui, E. Pleguezuelos, J. Andilla, E. Martín-Badosa and I. Juvells, (2008) "Algorithm for computing holographic optical tweezers at video rates"; SPIE Proceedings, 6326, 63262X-1/10

7. E. Pleguezuelos, A. Carnicer, J. Andilla, E. Martín-Badosa and M. Montes-Usategui, (2007) "HoloTrap: Interactive hologram design for multiple dynamic optical trapping"; Comput. Phys. Commun., 176, 701-709
Impact factor 2007: 1.842

Biophysical applications

8. A. Farré-Flaquer, C. López, J. Andilla, E. Martín-Badosa and M. Montes-Usategui, (2008) "Holographic optical manipulation of motor-driven membranous structures in living NG-108 cells"; J. Opt. A: Pure Appl. Opt., Publish pending
Impact factor 2007: 1.752

### 1.3.2 Communications to conferences in chronological order

I. Juvells, S.Vallmitjana, S. Bosch, A. Carnicer, M. Montes, E. Martín, J. Ferré, I. Labastida, F. Rodríguez, J. Pérez, R. Tudela, J. Sancho, E. Pleguezuelos, S. Arcos and J. Andilla, "Actividad investigadora del Grup de Recerca en Òptica Física de la Universidad de Barcelona", 7ª Reunión Nacional de Óptica, Santander, Oral, (2003)

I. Juvells, A. Carnicer, S. Vallmitjana, M. Montes-Usategui, E. Martín-Badosa, I. Labastida, R. Tudela, E. Pleguezuelos and J. Andilla, "Dynamic Holographic Optical Tweezers using full-complex codification in Spatial Light Modulators", XX Trobades Científiques de la Mediterrània (Fotònica: ciència i tecnologia de la llum), Maó (Menorca), Poster, (2004)

J. Andilla, E. Martín-Badosa and S. Vallmitjana, "Characterization of a reflective spatial light modulator by determination of its Jones matrix", V Reunión Iberoamericana de Optica y VII Encuentro Latinoamericano de Optica, Láseres y sus Aplicaciones. (RIAO/OPTILAS 04), Isla de Margarita, Oral (2004)

E. Martín-Badosa, M. Montes-Usategui, J. Andilla, E. Pleguezuelos, I. Labastida, S. Vallmitjana, I. Juvells and A. Carnicer, "Generation of holographic optical tweezers with arbitrary modulation operating curves", Diffractive Optics 2005, Warsaw (Poland), Oral (2005)

J. Andilla, E. Martín-Badosa and S. Vallmitjana, "Automatic Characterization of a Reflective Spatial Light Modulator", 5th International Workshop on Information Optics; Wio'06, Toledo, Oral, (2006)

J. Andilla, A. Carnicer, A. Farré, I. Juvells, I. Labastida, E. Martín-Badosa, M. Montes-Usategui, E. Pleguezuelos and S. Vallmitjana. "Trampas ópticas dinámicas utilizando moduladores espaciales de luz", 8ª Reunión Nacional de Óptica, Alacant, Poster (2006)

E. Pleguezuelos, J. Andilla, M. Montes-Usategui, I. Labastida, R. Tudela and A. Carnicer. "Holotrap: un software de generación de trampas ópticas holográficas en tiempo real", 8ª Reunión Nacional de Óptica, Alacant, Poster (2006)

M. Montes-Usategui, E. Pleguezuelos, J. Andilla and E. Martín-Badosa. "Algoritmo rápido de generación de trampas ópticas holográficas", 8ª Reunión Nacional de Óptica, Alacant, Poster (2006)

A. Carnicer, I. Juvells, J. Andilla and E. Pleguezuelos. "Performance of the reconstructed traps in a tilted-based-modulator holographic optical tweezers setup", EOS Topical Meeting on Diffractive Optics, Barcelona, Poster (2007)

C. López, F. Gómez-Morales, J. Andilla and E. Pleguezuelos, E. Martín-Badosa. "Shack-Hartmann wave front sensor applied to aberration correction in holographic optical tweezers", EOS Topical Meeting on Diffractive Optics, Barcelona, Poster (2007)

C. López, J. Andilla, M. Montes-Usategui and E. Martín-Badosa. "Correction of aberrations in holographic optical tweezers using a Shack-Hartmann wavefront sensor", 2008 conference on Nonlinear Microscopy and Optical Control, Münster (Germany) Poster (2008)

M. S. Roth, J. Andilla, E. Martín-Badosa and A. Carnicer "Software assisted design of a holographic optical tweezers system", EOS Annual Meeting 2008, Paris, Poster (2008)

J. Andilla, M. S. Roth, E. Martín-Badosa, S. de Lorenzo, F. Ritort, M. Montes-Usategui and A. Carnicer. "Design of Holographic Optical Tweezers for Application in Single-molecule Experiments", XXIV Trobades Científiques de la Mediterrània (Fisica a les ciències de la vida), Maó (Menorca), Oral (2008)

A. Farré, C. López-Quesada, J. Andilla and M. Montes-Usategui. "Explorant els mecanismes del trànsit Vesicular en cèl.lules vives mitjançant pinces òptiques", XXIV Trobades Científiques de la Mediterrània (Fisica a les ciències de la vida), Maó (Menorca) , Oral (2008)

# Chapter 2

# Discussion

This chapter summarizes the theoretical foundations of holographic optical tweezers. In our case, the optical tweezers we use are the so-called single beam optical tweezers. From this fundamentals, a detailed description of the whole system used is given. Software programs, biological protocols and methods to perform the experiments are also described to complete the explanation of the workstation. Finally, a thorough discussion of all parts is made.

## 2.1 Fundamentals and description

### 2.1.1 Optical tweezers theory

The radiation pressure phenomenon is the basis of optical trapping, and thus we can make a simple calculation to determine the typical size of particles that can be manipulated with optical tweezers. When light interacts with an object, part of the light's momentum is transferred to the object, and conservation of momentum requires that the object must undergo an equal and opposite momentum change. The resulting force is just the momentum change per second. For a light source of frequency $\nu$, photon's energy is $h\nu$ and thus photon's momentum equals $h\nu/c$. We can determine the number of photons per second in a beam of power $P$ as $P/h\nu$. Then, if we assume a total reflection of light on the object, the momentum's change will be twice the initial photon's momentum. So, the force produced by the beam is:

$$F = \frac{P}{h\nu}\frac{2h\nu}{c} = \frac{2P}{c} \tag{2.1}$$

This means that with a $10\,mW$ laser beam the force applied with perfect reflection is in the range of tens of pico Newtons. We can compare this force with the acceleration due to gravity. A sphere of density $10g/cm^3$ and $1\,\mu m$ of radius has a mass of $\sim 5 \cdot 10^{-14}kg$; if light exerts a force of $5 \cdot 10^{-11}N$, acceleration induced on the sphere is $1000\,m/s^2$, equivalent to $100$ times the acceleration of gravity. So, even though, in most practical situations the transfer of momentum would be much less efficient than that of perfect reflection. This result

defines the range of sizes on the micro-meter scale. Interestingly, we also find that forces involved in many important processes in molecular and cell biology are in the pico Newton range: for example, ligand-receptor binding ($200\,pN$ biotin-streptavidin), DNA conformation state change ($\sim 60\,pN$), protein unfolding ($15\,pN$ RNA polymerase), and molecular motor stall forces ($6\,pN$ kinesin) [SCB03]. These examples show the range of applications where optical trapping technology can be applied.

Single beam optical tweezers, presented by Ashkin *et al.* in [ADBC86], consists of a Gaussian laser beam strongly focused by a high numerical aperture microscope objective into a sample. As shown in figure 2.1, the tweezing effect of optical traps on a sphere can be explained using ray optics (when the radius of the sphere ($a$) is much larger than the wavelength of light). If a dielectric sphere is displaced from the center of the beam, a net force, produced by the deflection of light, will accelerate the bead towards the original position (fig. 2.1a). A similar effect occurs if the bead is out of focus (fig. 2.1b).

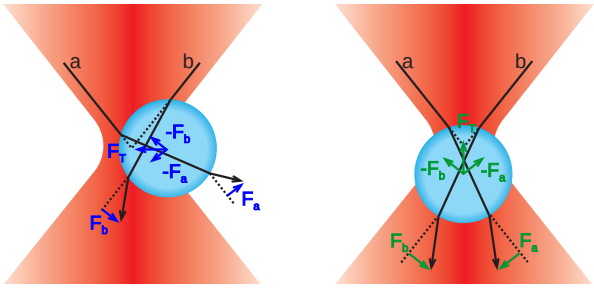


Figure 2.1: Total forces ($F_T$) produced by the momentum change of the rays $a$ and $b$ ($F_a$,$F_b$), when a bead is displaced form the equilibrium position a) Perpendicular to the optical axis b) Along the optical axis.

However, when a strict theoretical description is desired, the wavelength $\lambda$ of the laser beam plays an important role and must be taken into account. To solve Maxwell's equations to find a mathematical description of optical tweezers phenomena requires working in separate regimes. Optical force calculations in the Rayleigh regime ($\lambda \gg a$) use a dipole model [HA96], where the particle is considered just as a point dipole in an electric field. In the Mie regime ($\lambda \ll a$), the force is calculated by means of reflected and refracted light in the sphere, following Snell's law. However, when $\lambda \sim a$, numerical calculation of the electric field is needed. Some approaches have been proposed, using the Generalized Lorenz-Mie Theory (GLMT),in [RGG94], or an extension of the Rayleigh-Debye theory in, [RS01].
In the Rayleigh and Mie regimes the theory predicts two force components that are involved in the trapping effect: the scattering force and the gradient force. The scattering force ($\mathbf{f}_{sca}$) is an always positive force and pushes the bead in the direction of the beam, while the gradient force ($\mathbf{f}_{gra}$) always points towards the focus of the beam; the total force is the vector sum of the two components:

$$\mathbf{f}(\mathbf{r}) = \mathbf{f}_{sca}(\mathbf{r}) + \mathbf{f}_{gra}(\mathbf{r}) \tag{2.2}$$

The trapping effect will only occur if the gradient force is larger than the scattering force [ADBC86], otherwise scattering force would push the bead forward and no stable axial

trapping would be obtained. The gradient force is proportional to the gradient of light intensity. Large intensity gradients are obtained by using high numerical aperture microscope objectives, which strongly focus the beams. It is worth mentioning that, to maximize the trapping efficiency, the whole area of the exit pupil of the objective should be illuminated because rays passing through the external part of the entrance pupil make higher angles and, thus, they provide larger gradient forces.

In figure 2.2 we can see the scattering, the gradient and the total force in the Mie approximation exerted on a $2\,\mu m$ glass bead using $10\,mW$ of laser beam and an objective with $NA = 1$. Figure 2.2a depicts the force exerted when the bead is displaced along the propagation axis and figure 2.2b shows the force when the displacement is in the perpendicular direction. The zero position corresponds to the focus of the beam and the equilibrium position is reached when the total force is equal to zero; notice that in the axial case the equilibrium position is beyond the focus, because of the scattering force. In both cases, it exists an almost linear region between force and displacement which is typical of harmonic systems. This behavior is really convenient for measuring the force, because if the slope of this linear region is determined (known as trap stiffness $k$), the applied force $F$ on the bead can be determined by measuring its displacement $x$ from the equilibrium position, from: $F = -k \cdot x$.

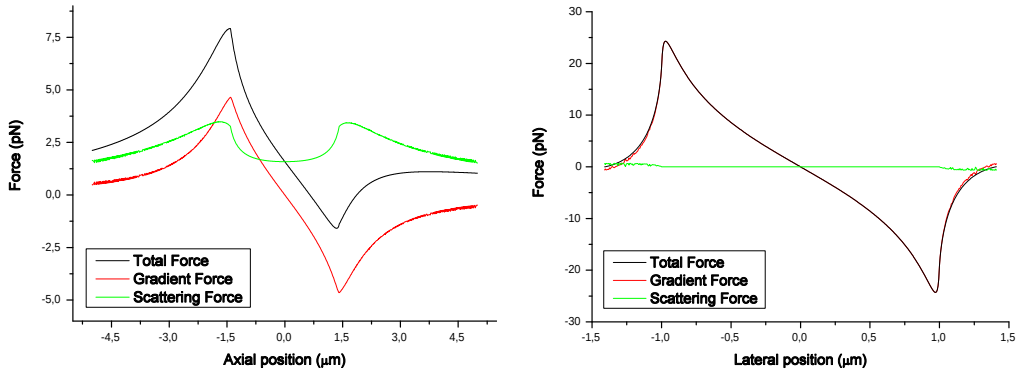


Figure 2.2: a) Force along the optical axis b) Force perpendicular to the optical axis

### 2.1.2 Holographic optical tweezers

In Fresnel approximation, we can mathematically describe the relation between the complex amplitude of the electric field before a lens and the corresponding complex amplitude on the focus plane of that lens as a Fourier transform [Goo96]. This consideration is the basis of Fourier holography, in which the complex information of a beam reflected by an object can be stored on a substrate (hologram); when this substrate is illuminated we obtain a beam that has the information of the original object. Reicherter *et al.* [RHWT99] used an LCD to introduce computer generated holograms into an optical tweezers setup. These holograms store the information of the inverse Fourier transform of a desired pattern of traps. However, LCDs can only modify the complex amplitude of the beam in a limited number of values. We can describe an LCD essentially as a matrix of independent liquid crystal cells (pixels),

sandwiched between two electrodes, such that each pixel can modify the amplitude and/or the phase of the incoming light. The way in which an LCD modifies the light wavefronts is based on the birefringent properties of liquid crystals and the polarization of light [YG99]. These properties can be modified by changing the electric field applied between the two electrodes. Usually, voltages between the electrodes are set by driving electronics with 8 bit resolution, which only define 256 possible states (often represented by gray levels) of the liquid crystal. LCDs can be configured to modify only the amplitude of light, only the phase or a combination of both. Possible configurations depend on the properties of the birefringent material, the polarization of the incident light and, if present, the orientation of a linear polarizer placed after the LCD [MB98]. The configuration that modifies only the phase of the beam (Phase-only configuration) is commonly used to generate holographic tweezers because of its efficiency and the simplicity of hologram computation.

Essentially, computer generated holograms used in holographic optical tweezers consist on the phase values of the inverse Fourier transform of a certain pattern. The holograms are calculated using a discrete Fourier transform that provides phase values at every $i$ and $j$ discrete position that will be written to the corresponding pixel on the LCD. The scale of the final hologram must be included in the Fourier transform by using a scale factor $\xi$ which is related to the characteristics of the setup [Ple06]. Equation

$$\Phi(i,j) = \arg\left(FT_{\xi}^{-1}\left(H\left(u,v\right)\right)\right) \tag{2.3}$$

describes how a phase hologram $\Phi$ can be obtained. $H(u,v)$ is the desired pattern of traps being $u$ and $v$ the spatial positions in the sample, $FT^{-1}$ is the inverse discrete Fourier transform, and $\Phi(i,j)$ contains the phase values that will be represented by every $i$ and $j$ pixel of the LCD. Results obtained by using the phase of an arbitrary complex hologram have, in general, low trap efficiency and may have some problems when reconstructed [CSS05]. In section 2.2.1 we will discuss some algorithms to achieve better results.

### 2.1.3 Force calibration

As we have seen in section 2.1.1, we can find a range of distances, when a bead is displaced out of the center of the trap, where it exists a direct proportionality between the force exerted by the trap and that displacement. The stiffness constant $k$ can be determined with several methods. Capitanio *et al.* [CRB+02] presented a comparison between different calibration methods and evaluated their advantages and disadvantages. All the methods analyzed in their paper use the experimental setup proposed by Svoboda and Block in [SB94a], but can be directly applied with our experimental setup, which is based on the work presented by Finer *et al.* in [FSS94]. A bead trapped in an optical trap acts as a scattering particle (see fig. 2.1) and modifies the beam. If this beam is collected by a lens it forms a pattern in its back focal plane. The position of the center of mass of this pattern is directly related with the position of the bead, as demonstrated in [GS98] in the Rayleigh regime, and demonstrated for the Mie regime in [SCB03]. The position of the center of mass can be determined with a

position sensor as a Quadrant Photo Detector (QPD) or a Position Sensitive Detector (PSD). However, the signal provided by these detectors is a voltage which should be accurately calibrated, because it critically depends on the characteristics of the system, such as the focal lengths or the distances between the optical elements. Signal in volts and position are proportional in a certain region around the equilibrium position. We will call $\beta$ to the proportionality constant. As commented above, in the linear region (see fig. 2.2) the force is proportional to the displacement from the equilibrium position $F = -k \cdot x$. Then, the total force will be provided by the calibration factor $\beta$, the trap stiffness $k$ and the detector signal $V$ as

$$F(V) = -k \cdot \beta \cdot V \tag{2.4}$$

The factor $\beta$ can be determined by moving it in controlled and known steps a bead stuck to the glass that holds the sample (usually a glass coverslip of around 170 microns thick). This method is only valid if the experiment following the calibration is performed very close to the coverslip, so that the experimental conditions are nearly the same.

To determine the trap stiffness we use a method based on the work by Svoboda *et al.* presented in [SSSB94]. The motion of a micro-sized bead in a harmonic potential can be described in terms of the Einstein-Ornstein-Uhlenbeck theory of the Brownian motion [BSF04]. Using this theory in the frequency domain it can be demonstrated that the expected value of the power spectral density of the signal is a Lorentzian function:

$$\begin{aligned} P(f) &= \frac{1}{2\pi} \frac{D}{f_c^2 + f^2} \\ D &= \frac{k_B T}{\gamma} \\ f_c &= \frac{k}{2\pi\gamma} \end{aligned} \tag{2.5}$$

The parameters that characterize this function are the low frequency plateau $D$ and the corner frequency $f_c$ (fig. 2.3), where $k_B$ is the Boltzman constant, $T$ is the absolute temperature and $\gamma$ is the Stokes friction coefficient. Using this method, the trap stiffness $k$ can be determined from $f_c$ and is independent from position calibration. Fortunately, this method also allows to determine the factor $\beta$, which can be calculated from the value of the measured plateau $D_V$ and the theoretical value $D$ calculated from equation 2.5, using $D = D_V \cdot \beta^2$. The drawback of this method is that $\gamma$ must be known, usually, it is approximated to the nominal value determined in ideal conditions.

### 2.1.4 Biology

Cell structure and molecular motors

The cell is the structural and functional unit of all known living organisms. In a very basic picture, the cell can be described as a closed membrane that contains the cytosol with

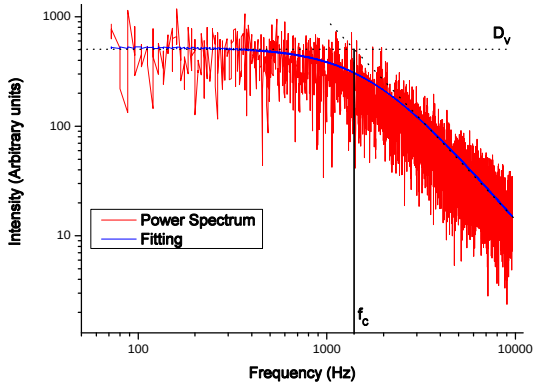


Figure 2.3: Power spectrum Lorentzian fitting

organelles and the cytoskeleton. The cytoskeleton, consisting of actin filaments, microtubules and intermediate filaments provides the cell its mechanical structure. This structure is continuously modified and in constant activity. Organelle transport along actin filaments and microtubules is carried out by specialized motor proteins. These proteins use the energy provided by the conversion of ATP into ADP to change its tertiary chemical structure and realize a translocation [AJL+02]. Motor proteins related with the cytoskeleton are classified in three large families: myosins, which are related with actin filaments; kinesins, which travel along the microtubules carrying organelles towards the plus end of the microtubule, where the activity is larger; and finally, dyneins, which are also related to microtubules and organelle transport but move in the opposite direction. A single myosin can exert a force of $3-4\,pN$ [FSS94], a kinesin produces up to $6\,pN$ [SB94b] and a single dynein can exert forces up to $1.1\,pN$ [MCL+04]. However, biological processes like organelle transport often imply several molecular motors working coordinately, producing larger forces.

### Single molecules

The structure of biological molecules and specially proteins can become extremely complex. By combining the twenty different types of amino acids we can find proteins formed by huge polypeptide chains defining labyrinthine three dimensional structures. The structure provides a specific behavior and defines the protein's functional nature. Other molecules, such as DNA, formed by combination of four types of nucleotides, presents simpler basic structures. These nucleotides form two type of base pairs which are packed in the well-known double-helix structure. The important parameters in DNA stretching experiments are the number of base-pairs ($bp$) of the strand and its contour length ($l_0$). The elastic properties of DNA strands have been successfully modeled using the worm-like chain model, which characterizes the polymer elastic properties using a single parameter, the persistence length [BWA+99]. When the molecule is stretched beyond the contour length the overstretching state is reached and the standard double helix structure is broken, undergoing a phase-state transition, characterized by a plateau in the elastic response of the molecule [SCB96]. Also, other states of the helical DNA conformation can be found in accordance to the highly adaptability of the DNA [BSG+03].

## 2.2 Results

### 2.2.1 Holographic optical tweezers setup

This section details the Holographic Optical Tweezers system used to perform biophysical experiments. The analysis of the system is divided into three independent parts: LCD's characterization, analysis of the characteristics the position and of the optical elements, and finally description of the software used to generate the holograms used as interface to control the trap. However, because the same optical setup has been used to perform two different type of experiments, the specific hardware used for each one is presented in section 2.2.2.

#### LCD calibration

In this work, two different LCDs are used, a Holoeye LC-R 2500 and a Hamamatsu X10468-3. Both devices are based on Liquid Crystal on Silicon (LCoS) technology. The basic structure of this kind of LCDs consists of a liquid crystal sandwiched between a transparent electrode and an integrated circuit grown on a Silicon substrate. Because of this arrangement, the integrated circuit acts as a mirror while the characteristics of the beam are modified due the liquid crystal. Some relevant characteristics of the two modulators are summarized in table 2.1.

| | Holoeye | Hamamatsu |
|---|---|---|
| Pixels | 1024 × 768 (XGA) | 800 × 600 (SVGA) |
| Pixel pitch | 19 $\mu m$ | 20$\mu m$ |
| Fill factor | $93\%$ | $95\%$ |
| Working wavelength | 532 nm | 1064 nm |

Table 2.1: LCD characteristics

The modulation response of each device changes with the angle of incidence of light; we have set an angle of $45^\circ$ for the Holoeye LCD and of $10^\circ$ for the Hamamatsu LCD. However, the most important characteristic that differentiates both LCD is the nature of the liquid crystal layer. Behavior of reflective LCDs has been studied and modeled by Lu and Saleh in [LS04] and more specifically for LCoS LCDs by Yang and Lu in [YL99], using the Jones matrix formalism. The polarization states of the crystal are defined in terms of the twisting angle ($\Phi$), the birefringence ($\Delta = n_e(V) - n_o$ which extraordinary index depends on the voltage between electrodes) and the wavelength of light ($\lambda$). Equation

$$J(\Phi,\beta) = \exp(-i2\beta)\begin{pmatrix} \left(\frac{\Phi}{\alpha}\right)^2 + \left(\frac{\beta}{\alpha}\right)^2 \cos 2\alpha - i\left(\frac{\beta}{\alpha}\right)\sin 2\alpha & -i\frac{\Phi\beta}{\alpha^2}(1-\cos 2\alpha) \\ -i\frac{\Phi\beta}{\alpha^2}(1-\cos 2\alpha) & \left(\frac{\Phi}{\alpha}\right)^2 + \left(\frac{\beta}{\alpha}\right)^2 \cos 2\alpha + i\left(\frac{\beta}{\alpha}\right)\sin 2\alpha \end{pmatrix} \quad (2.6)$$

describes the model used in those papers, where $\beta = \pi\Delta/\lambda$ and $\alpha = \sqrt{\Phi^2 + \beta^2}$. The Holoeye LCD uses a $45^\circ$ twisted nematic liquid crystal cell ($\Phi = \pi/4$) while the Hamamatsu LCD

consists of a parallel nematic liquid crystal cell ($\Phi = 0$). Notice that for a parallel nematic liquid crystal, $\Phi = 0$ and thus $\alpha = \beta$. This simplifies equation 2.6 into:

$$J(0,\beta) = \exp(-i2\beta)\begin{pmatrix}\cos 2\beta - i\sin 2\beta & 0\\ 0 & \cos 2\beta + i\sin 2\beta\end{pmatrix} = \begin{pmatrix}\exp(-i4\beta) & 0\\ 0 & 1\end{pmatrix} \quad (2.7)$$

This equation describes phase retarder, which introduces a $4\beta$ phase shift between the $x$ and $y$ components. This phase shift is dependant on the voltage, then, each pixel acts as a variable phase retarder, which allows Hamamatsu LCD introducing, directly, phase-only holograms when using linearly polarized light in the proper direction. A simple characterization method to determine the $\beta$ parameter response in terms of the input gray level is presented in [FBI+05]. This response corresponds to the phase shift shown in figure 2.4b.

The Holoeye LCD is based on a twisted nematic liquid crystal. As it can be seen in equation 2.6, if $\Phi$ is not zero the modulator model is not a variable phase retarder anymore. In order to determine a configuration that provides a phase-mostly response, a characterization of the LCD is necessary. Some LCD calibration methods as [YL99], measure the characteristic parameters of the model to determine the behavior of the device. In appendix A we present a calibration method using a different approach in which the only assumption is that the modulator behaves as a polarization device and thus can be described by a Jones matrix. This approach avoids the mathematical modeling of the LCD and it can be applied to any kind of LCD which satisfies the previous assumption. The method consists in the analysis of the influence of the LCD on the polarization state of the incoming light. Three input states and the corresponding outputs are measured to determine the LCD influence in terms of a Jones matrix. This analysis is repeated for each addressing gray level describing the modulation response of the LCD in terms of each gray value. The knowledge of these matrices allows us to simulate and predict the modulator response for any configuration. We used this result to find a phase-mostly configuration by minimizing the amplitude variation while keeping the phase modulation range close to $2\pi\, radians$. The result obtained, shown in figure 2.4a, corresponds to a phase modulation range of $1.98\pi\, radians$ and $1 : 1.13$ of intensity contrast. Often the small amplitude variation introduced by a phase-mostly configuration when using phase holograms generates an undiffracted zero diffraction order. In our case this undesired beam nearly vanishes and almost all the energy is concentrated in the holographic pattern.

Optical aberrations due to the non-flatness of LCDs introduce a deformation in light's wavefront. When an aberrated beam is focused by a microscope objective the generated spot is significantly deteriorated which, in the case of optical tweezers, may prevent stable trapping of particles. The curvature of the LCD can be compensated adding suitable phase values to the computed phase hologram sent to the display. The flatness of the surface is usually obtained by interferometry and, in the case of the Hamamatsu LCD, the conjugated values that must be added to the computed hologram are provided by the manufacturer itself. Unfortunately, the Holoeye LCD curvature is not available. To solve this problem we followed two different strategies, first we performed an initial and approximated correction and finally

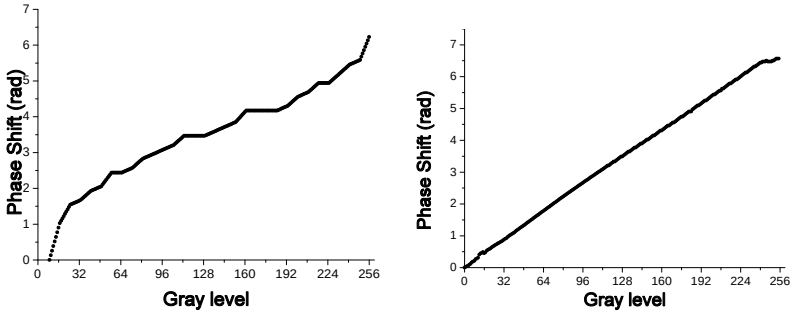


Figure 2.4: Phase shift vs. gray level a) Holoeye LCD b) Hamamatsu LCD

a more comprehensive and accurate one.

When looking at the shape of the distorted spot, we can find two perpendicular lines that appear in two different focal planes, in a behavior similar to the astigmatism. In order to compensate this aberration as well as an additional defocus term, the correction was modeled as a toroidal tilted lens. The characteristic foci and the tilting angle of this model were determined experimentally. The results are presented in appendixes B and G. Those good results were achieved only when the central part of the LCD was illuminated, because the external region introduces higher order aberrations. This limitation prompted us to compensate the whole display using a Shack-Hartmann sensor to measure the distorted wavefront at the modulator plane and calculating the appropriate correction (appendix E). By using this method iteratively, we finally obtained a flatness up to $\lambda/16$. Figure 2.5 shows the generated spot that we would obtain using each modulator without any correction. These pictures have been obtained simulating the effect of the microscope objective by means of a Fourier transform. In order to obtain a reliable simulation we calculated the scale bar according to the parameters of the experimental setup used with each LCD.

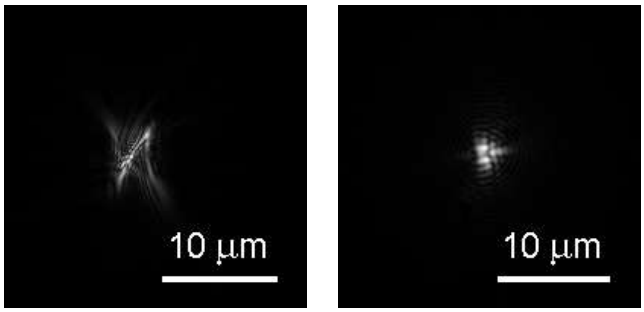


Figure 2.5: Simulated spot obtained without correction a) Holoeye's LCD (Telescope magnification $\Gamma = 1/3$, 100x) b) Hamamatsu's LCD (Telescope magnification $\Gamma = 2/3$, 60x)

To obtain the desired values using computer holograms, the values sent to the LCD need to contain the information given above. Aberration correction which is added to the hologram calculated in section 2.1.2 to counteract the own curvature of the display. Resulting value has to be the modulo $2\pi$ of this addition. Once the phase shift for every pixel is known,

it has to be transcribed into gray levels by using the calibration that connects every phase value with its corresponding gray level.

### Optical design

We can mainly describe a holographic optical tweezers setup as follows: a TEM00 laser beam is expanded and collimated by a pair of lenses forming a telescope, and it is leaded to illuminate the LCD. After reflection on the LCD, the beam is reduced by a second telescope. Finally, it is guided to illuminate the entrance pupil of the microscope objective that will generate the optical trap. In order to obtain good quality holographic optical traps, we studied all the elements described above and analyzed which details are more relevant in terms of quality, efficiency and mechanical stability when designing a holographic tweezers setup.

The LCDs used in this work have been widely discussed in the previous section; and for the current analysis they will be considered, as ideal phase modulators. The definition parameters of the LCDs we take into account to perform this study are the working wavelength, size of the LCD (see table 2.1) and the angle of incidence of the light on the LCD. Layouts of the setups using both LCDs are shown in figure 2.6.

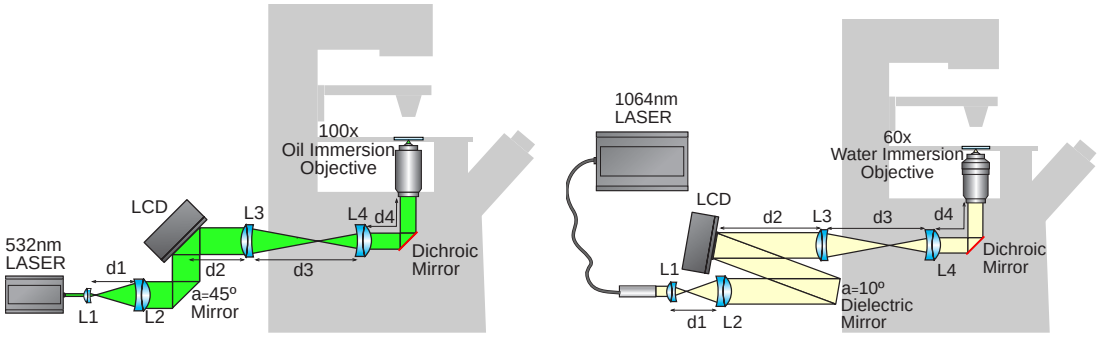


Figure 2.6: a) Scheme using a Holoeye LCD b) Scheme using a Hamamatsu LCD

To obtain a stable and efficient setup we should take the following requirements into consideration:

1. In order to maximize the trapping force, the central part of the gaussian beam must fill the exit pupil of the microscope objective ([Ash92], [FA03]).

2. The LCD must be imaged onto the exit pupil of the microscope objective to prevent vignetting of high-frequency Fourier components, which get diffracted at larger angles ([CKG02], [Gri03]).

3. Compact setups are desired (App. B) and should be assembled with the smallest number of elements.

4. The telescopes must provide parallel illumination both to the LCD and to the infinity-corrected objective.

5. Clipping due to the size of the objects must be avoided.

We built the holographic optical tweezers system using two different models of commercial inverted microscopes, a Nikon Eclipse TE-2000 and a Motic AE-31. Objectives used in each case are: 100x Plan Fluor (Oil 1.30NA DIC or ph3) and 60x Plan Apochromat (Water 1.25NA) on the Nikon and 100x Planachromat (Oil 1.25NA) on the Motic. The use of commercial microscopes allows visualization of the sample using the standard capabilities of the microscope while the microscope objective is also used to generate the optical trap. The laser beam is sent to the objective through the epi-fluorescence port using a dichroic mirror mounted in the filter's cube of the epi-fluorescence toolkit (see fig. 2.6). However the use of commercial microscopes introduces an important physical constraint: a minimal distance between the last lens of the second telescope, $L_4$, and the objective. As shown in appendix B, the optimal arrangement of the second telescope is a 4-f configuration: this defines the focal lengths and positions of the second telescope lenses in terms of the size of the LCD ($l_{LCD}$), the exit pupil diameter ($D_{EP}$), and the distance between $L_4$ and the first surface of the microscope objective ($d_4$). Relationship between these parameters is shown in equation:

$$\begin{aligned} f_{L4} &\geq d_4 \\ \left|\frac{f_{L4}}{f_{L3}}\right| &\geq \left|\frac{D_{EP}}{l_{LCD}}\right| \end{aligned} \tag{2.8}$$

. Optimal conditions are obtained when identity holds, but, usually, exact focal lengths are not available in lens catalogs, then we should choose the available lenses in agreement with equation 2.8 and as small as possible, according to the consideration 3.
The parameters for the first telescope ($f_{L1}$ and $f_{L2}$) are determined, following the first consideration, to obtain a magnification which expands the beam ($D_{laser}$) to overfill the LCD ($l_{LCD}$):

$$\left|\frac{f_{L2}}{f_{L1}}\right| > \left|\frac{l_{LCD}}{D_{laser}}\right| \tag{2.9}$$

In case of partial illumination of the LCD, as used in appendix B and G to correct astigmatism aberrations (see previous section), the value of $l_{LCD}$ of equation 2.8 should be replaced by the real size of the expanded beam that illuminates the LCD.
Optical aberrations introduced by the optical elements are analyzed on appendix B. Their negative effect on trap stiffness is well documented [RWGG06] and must be minimized while designing the optical setup to obtain good quality traps. In this work we used three different laser sources, a 1064 nm Ytterbium fiber laser (IPG Laser GmbH, $P_{max}$=5 W), a 532 nm Nd:$YVO_4$ solid state laser (frequency-doubled Viasho Technology $P_{max}$=120 mW) and a 1064 nm Nd:$YVO_4$ solid state laser (Viasho Technology $P_{max}$=1 W). A pinhole spatially filters the beam of solid state lasers at the back focal plane of the expander lens (L1) to ensure a clean, Gaussian illumination; on the LCD, in the case of the fiber laser, the beam is already filtered and collimated. Aberrations due to short focal lengths of the lenses can be relevant, specially in the case of the first telescope. We performed a ray-tracing simulation with the commercial optical design software ZEMAX$^{TM}$ to study the aberrations produced

by the optical elements of the setup. In appendix B a partial simulation was presented because neither the expander nor the microscope objective were fully modeled and were simulated as paraxial lenses. Using this simulation, we found that the collimating lens of the first telescope had a critical aberration contribution and an achromatic doublet should be used. On the other hand lenses of the second telescope are less critical and plano-convex singlets can be used with the proper orientation; the flat surfaces must face each other. More recently, a full simulation of the system was performed adapting the patent of the 60x water immersion objective [Yam07] to the infrared range (fig. 2.7). Also the expander lens ($L_1$) could be modeled because the fiber laser was used this lens was known. With this simulation we demonstrated that in the infrared range the water immersion objective can be used to generate diffraction-limited traps in depths up to the working distance of the objective ($270\,\mu m$). We also demonstrated that due to the change of refractive index of the objective lenses when using an infrared wavelength, the focus plane when using visible wavelengths or when using infrared wavelengths is slightly in a different position. Then, to obtain the trap in the same plane where the sample is focused we must slightly defocus the second telescope.

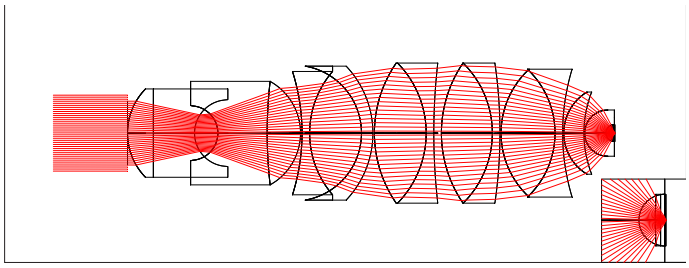

Figure 2.7: Zemax model of the 60x Nikon water immersion objective in the IR range

We measured the transmission efficiency of each element of this last setup and we used the method presented in [SB94a] to determine the transmission of the microscope objective. Absorption obtained for each element are: $2\%$ for singlets and $4\%$ for doublets, $3\%$ for the dielectric mirror and the dichroic mirror, $3\%$ due to the LCD and finally $52\%$ due to the microscope objective. The total efficiency of the system is around $29\%$, then we can determine that energy losses due the clipping and overfilling are of $25\%$.

### Software

One of the main features of holographic optical tweezers is the possibility to control the beam on real-time by means of an LCD. Fast generation of computer generated holograms is required to obtain a smooth interactive control. However, as shown in section 2.1.2, phase holograms are used because of the LCD capabilities and, unfortunately, computing the phase hologram for an arbitrary pattern of traps is not always straightforward. Trap efficiency (defined as the fraction of light directed to the requested traps) of phase holograms needs to be optimized to obtain more energetic optical traps and to avoid undesired ghost traps generated by the remaining light. Some algorithms, such as Gerchberg-Saxton [GS72] and

generalized adaptive additive algorithm [CKG02] have been proposed to obtain holograms with a high trap efficiency. The computational cost due to the iterative nature of these algorithms limits the interactive potential of holographic tweezers. The superposition method of prisms and lenses presented by Liesener *et al.* [LRHT00] extracts a phase hologram from the complex superposition of a set of phase holograms of single traps. This is a direct method without iterations that provides good speed performance. Unfortunately, this method fails for periodic patterns [CSS05], several ghost traps are generated and the uniformity of the pattern intensity is degraded (see fig. 2.8a).

In appendix C, we present an adaptation to optical tweezers of the random mask encoding algorithm proposed by Davis and Cottrell in [DC94]. In a similar way to prisms and lenses strategy, this algorithm consists in a superposition of single trap holograms, but in this case each hologram is assigned into a certain number of randomly distributed pixels of the final hologram. This straightforward algorithm drastically reduces the calculation time and produces no ghost traps obtaining uniform patterns of traps in a short period of time. The main drawback of this algorithm is trap efficiency, which decreases proportionally to the number of traps, as shown in appendix H. In this paper we also discuss different strategies to enhance the efficiency. Figure 2.8 corresponds to the simulation of the resulting trap pattern when using prisms and lenses, Gerchberg-Saxton and random binary masks algorithms, respectively. We can see the low uniformity of the pattern and the ghost traps in figure 2.8a; in figure 2.8c, there is a background light uniformly distributed around the whole area; finally, in figure 2.8b, ghost traps still appear but are hardly visible.

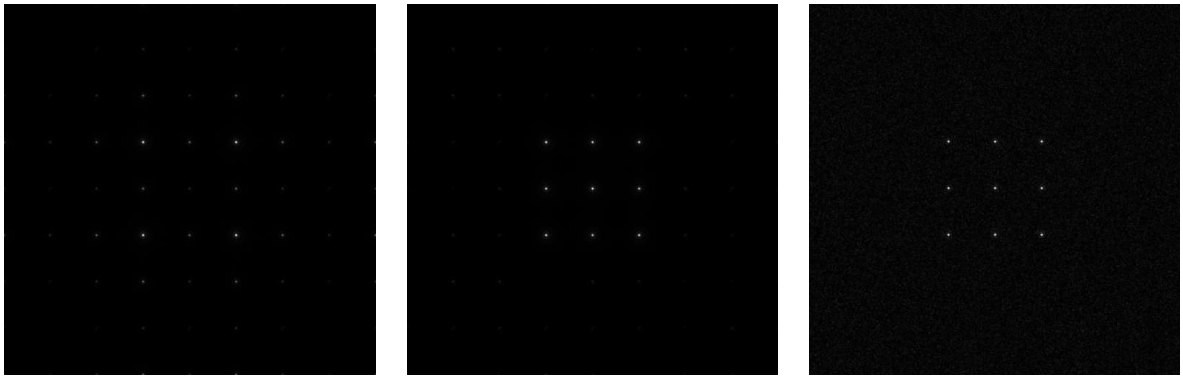

Figure 2.8: Simulation of the reconstruction of a 3x3 pattern of traps hologram using the algorithms: a) Prisms and lenses b) Gerchberg-Saxton c) Random masks

Prisms and lenses and random masks algorithms have been implemented in the computer program presented in appendix D. In order to obtain a user friendly interface to interact with the sample, this program incorporated click-and-drag mouse control of trap positions over a live-video image of the sample. When implementing this software, an important bottleneck appeared: the conversion from phase computed value to the closest phase value available in the LCD required an exhaustive search which slowed down the hologram calculation. To overcome this bottleneck, we used a pre-calculated phase mapping that directly translates the phase value to the corresponding gray level sent to the LCD [BJ95]. We obtained frame

rates of 16 frames per second using the random masks algorithm in a standard Pentium PC (P-IV HT 3.2 GHz) [Ple06]. In the case of the prisms and lenses algorithm, when a single trap is used we obtain the same frame rate as with random masks algorithm, however, if we add one or more traps the frame rate drops significantly.

Finally, we tested the whole holographic optical tweezers setup to trap and manipulate polystyrene beads of different sizes. Using $250\,mW$ on the sample plane, we trapped and manipulated groups of four beads with sizes between $5\,\mu m$ and $200\,nm$ (fig. 2.9). The setup used the water immersion objective on the TE-2000 Nikon microscope, Hamamatsu LCD and the $1064\,nm$ Ytterbium fiber laser.

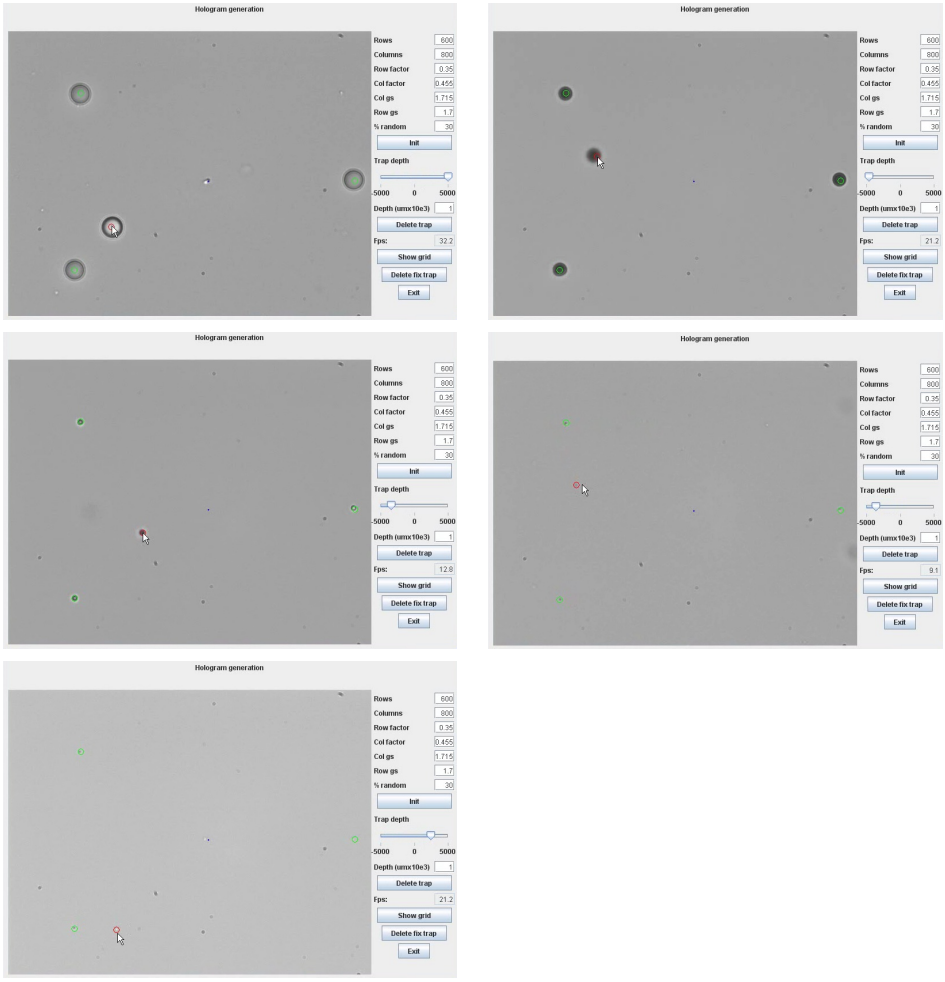


Figure 2.9: Holographic trapping and manipulation of beads a) $5\mu m$ b) $3\mu m$ c) $1\mu m$ d) $500nm$ e) $200nm$

## 2.2.2 Applications

The use of holographic optical tweezers adds interesting features to the standard optical trapping techniques that can be used in many different applications. In this section, we use this technique to catch and manipulate organelles in living cells to study the intracellular

transport, and to test if this technique can be used to study bio-molecules properties in single-molecule experiments.

Study of vesicle transport in living cells

Molecular motors are in charge of intracellular transport. These motor proteins have been studied using optical tweezers to unveil their mechanical properties when driving micro-beads. This kind of studies is usually done *in vitro*. Transport mechanisms in living cells are more complex and the forces involved in this processes remain poorly understood.

In this section I present the application of dynamic holographic traps to study the molecular motors involved in vesicular transport of NG-108 cells(app. F). NG-108-15 is an immortalized mouse neuroblastoma cell line, which was developed in 1971 by Hamprecht et al. [HGR$^+$85]. This cell line has been widely used in the study of neural function. Usually, spread cells are almost invisible by using standard bright-field imaging. However, under conventional phase contrast microscopy, cell and vesicular trafficking is easy visible. NG-108 cell line was provided by Dr. Ehrlicher (University of Leipzig). They are cultured, in the cell-culture laboratory of the Scientific-Technical Services of the Universitat de Barcelona, at $37^\circ$ in a humidified atmosphere containing $95\%$ air and $5\%$ $CO_2$, with a specially formulated medium replaced every two or three days:

- $90\%$ Dulbecco's modified Eagle's medium (DMEM)
- $10\%$ Fetal Calf Serum
- $1\%$ 100U/ml Penicilling/Streptomycin
- $1\%$ 1M HEPES yielding 10 mM concentration

Cells are cultured in plastic Petri dishes, and are resuspended and subcultured prior to confluency every seven days. After several weeks of trials we have determined that around $10^5$ cells must be plated in the new petri dish to obtain about $80\%$ of total confluency after $7$ days. Division procedure can be repeated until passage $35$ when cells are discarded to avoid possible unknown behavior because of genetic mutations. In this case new cells are thawed. In order to have a pool of frozen cells, the cells of every second subculture after the thaw process are frozen. In fact it is possible to freeze the cells of the first passage after thaw, but in order to avoid possible stress it is recommended doing it after the second division.

The freezing protocol consists in resuspending a large quantity of cells ($\sim 1.5 \cdot 10^6$/ml) in a freezing medium:

- $80\%$ Fetal Calf Serum
- $10\%$ Dulbecco's modified Eagle's medium (DMEM)
- $10\%$ Dimethylsulfoxide (DMSO)

Resuspended cells are placed in cryo-tubes of 1ml. Cooling of vials should be slow to minimize cell death by crystallization of the medium. In order to obtain this slow cooling ratio, cryo-tubes are placed in an expanded polystyrene box which is placed in a freezer. After some hours the cryo-tube can be stored in liquid nitrogen. In the thawing procedure the cryo-tube should be gently warmed up. The cell suspension is diluted in $5\,ml$ of culture medium. This dilution is centrifuged and the cells are resuspended with fresh culture medium. It is really important in the thaw/freeze process to minimize the time lapse of contact between cells and Dimethylsulfoxide solution. In fact, Dimethylsulfoxide is toxic for the cells at $25°$. Viability ratios obtained are about $80\%$ after the whole process.

When working with optical traps, special Petri dishes should be used (fig. 2.10a). The reason is that working distances of oil immersion objectives are about hundreds of microns, while the standard thickness of a plastic Petri dish is about $2\,mm$. So, to use culture dishes with high magnification objectives, a round area of the bottom of the dish is removed and substituted by a round coverslip of $0.17\,mm$ of thickness. Usually this kind of cells adhere poorly to glass. A surface coating of matrix proteins is used to improve adhesion. A solution of Laminin (Sigma L2020) in phosphate buffered saline ($40\,mg/ml$) is used to deposit the protein into the glass surface. It is necessary to cover the glass with $300\,\mu l$ of this solution and incubate it for more than one hour at $37°$. Then, the cells are plated and incubated 24 hours in the special Petri dish. When they adhered to the substrate, the dish is moved to the incubator of the optical laboratory, and stays there for an hour. Then, the cells are ready for the experiment.

The maintenance o mammalian cells on the microscope stage requires special equipment. Living conditions are obtained by using a home-built system, based on the work of Ehrlicher et al. [EBS+07] and adapted to our microscope and dishes. In figure 2.10b the dish heater is shown. The aluminium block has been turned to hold the dish on the microscope, to fit the dish guaranteeing a good thermal contact but allowing the light's pass (fig. 2.10b left inset). The two lateral holes contain heater cartridges controlled by a Proportional-Integral-Derivative (PID) controller. This controller registers the temperature of the system by means of a thermocouple and generates current pulses to feed the heating cartridges. In figure 2.11a we show the built-in box with the controller, the contacts and the protection fuse. Controlled atmosphere with 5% of $CO_2$ and nearly 100% of humidity is obtained by using a special Delrin top (fig. 2.10a). The special design creates a perfusion gas chamber but allows transmitted illumination. One of the top connectors is used to insert the gas mixture into the chamber and the second one is opened to the atmosphere. Positive pressure of gas guarantees sterility of the system. The microscope objective also requires a heater (fig. 2.11b) due to the thermal contact with the bottom coverslip. In this case, the voltage that controls the temperature of the heater is set manually.

Using this setup cells can be placed in the microscope stage for, at least, four hours. In figure 2.12 a 2 hours 40 minutes sequence of living NG-108 cells is presented. As men-

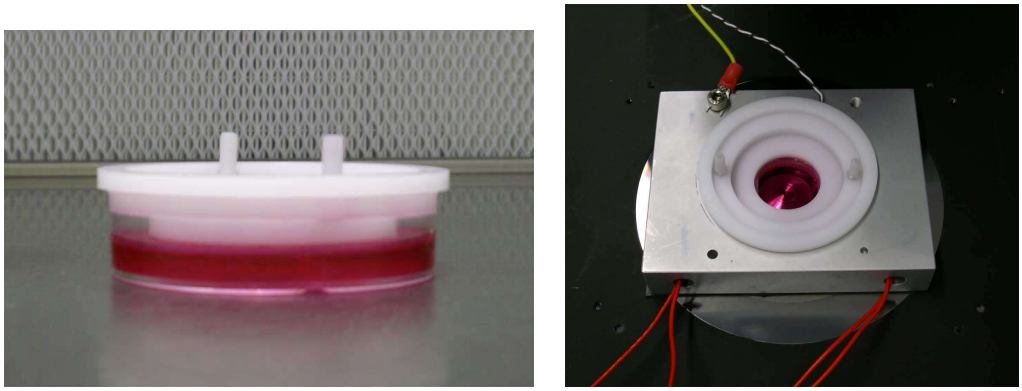

Figure 2.10: a)Experimental dish b)Dish heater

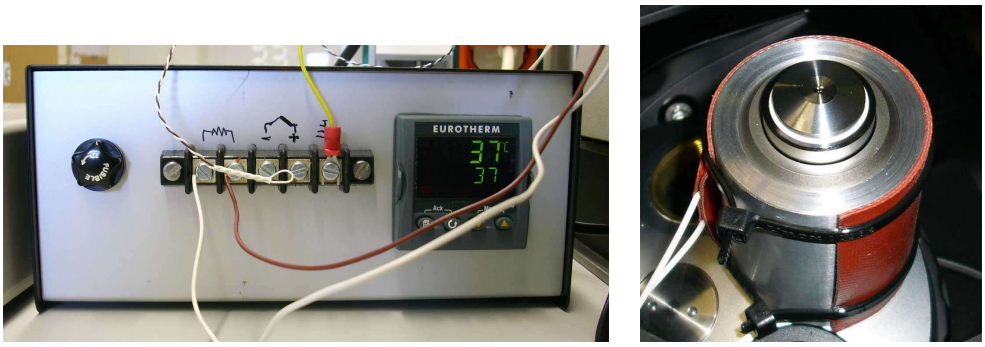


Figure 2.11: a)PID controller box b)Objective heater

tioned above, vesicular traffic is clearly seen under phase contrast conditions. We used a 40x phase contrast air objective to increase the field of view of the sample. As it can be seen, movement and shape of the cells indicate good living conditions. NG-108 grow and proliferate attached to the substrate, a round shape of many of the cells would indicate that experimental conditions were inappropriate.

The transport of organelles inside the cell can be quite fast, around $1\,\mu m/s$. This requires dynamic generation of optical traps which should be moved rapidly to follow the particles. The software presented in the previous section is suitable to steer an optical trap to catch organelles and perform the experiment described in appendix F. This work is based in the experiments performed independently by Ashkin et al. [ASD$^+$90] and Welte et al. [WGP$^+$98] to measure the stall forces of motor proteins in living giant amoeba Reticulomyxa and in Drosophila cells. Ashkin's force calibration data established the relationship between laser power ($1\,mW$) and force exerted by molecular motors ($\sim 0.041\,pN$) on a $320\,nm$ mitochondria. We used this result in our experiment as a reference to determine the force applied to a vesicle. $80\,mW$ of laser power was used to trap an organelle by using the click-and-drag interface described in the previous section. By using the reference data, the force applied by the optical trap was about $2.3\,pN$ which directly implies that the motors which moved the organelle exert weaker forces. We reduced the laser power down to $45\,mW$, when the vesicle was released from the trap. The trapping force in this case was $\sim 1.3\,pN$ which is

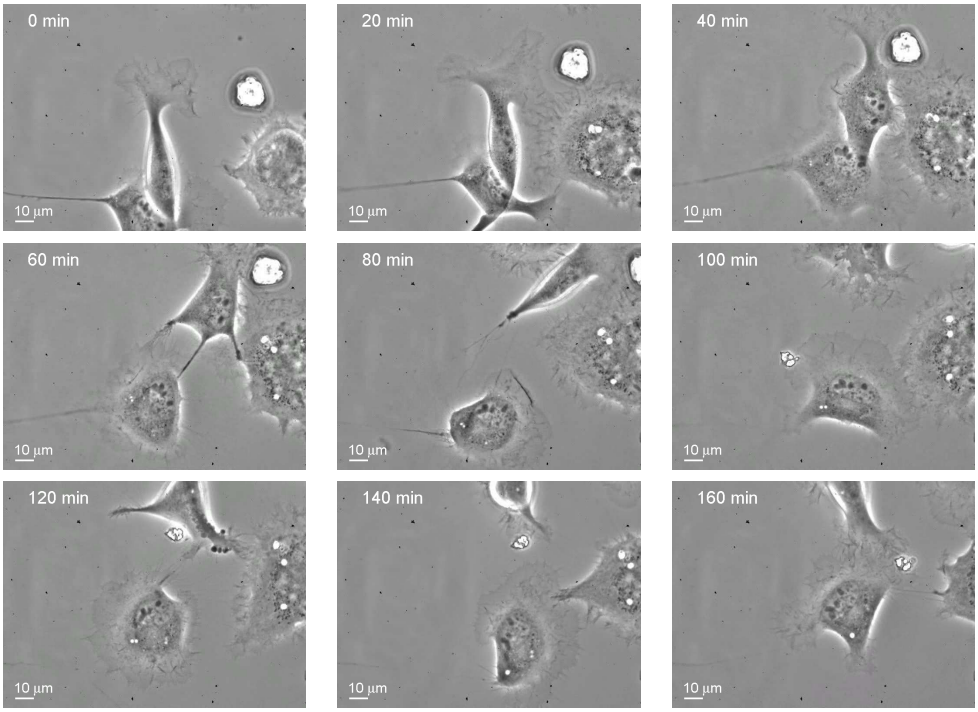


Figure 2.12: NG-108 alive in the microscope stage of the holographic optical tweezers system using a 40x phase contrast objective

similar to the dynein stall force ($1.1\,pN$) [MCL+04].

Study of DNA stretching with holographic optical tweezers

Study of single molecules by using optical forces made possible the determination of mechanical forces present in several relevant biological processes. However, the bio-molecules involved in those processes are really complex. As it has seen, adding holographical capabilities to an optical trapping setup opens the door to new possible experiments. In this section it is presented a preliminary experiment that compares standard a DNA stretching experiment with a holographic based version. The main goal is determining if it is possible to reproduce similar results in terms of force, precision and sensitivity in the holographic experiment compared to the standard one.

Both ends of a DNA strand are attached to different micro-beads. One of the beads is strongly fixed by air suction with a micro-pipette. The other one is trapped by optical forces (see fig.2.13). Increasing the distance between the two beads, the DNA strand will be stretched. To attach the DNA's end and a micro-sphere, the latter is coated with a specific chemical substance† (e.g. streptavidin). One of the ends of the DNA strand is labeled with the complementary molecule (biotin) to obtain a strong non-covalent bond. To avoid double attachments between the two ends of a single molecule and the same bead a different combination of chemicals is used to attach the other end (digoxigenin label/anti-digoxigenin

†Provided by Felix Ritort's Small Biosystems Lab

coated bead).

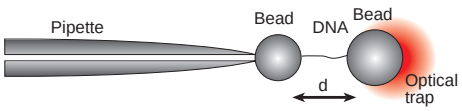


Figure 2.13: DNA stretching experiment scheme

The nature of trap steering will define the two experiments. On the first case, a mechanical displacement of lenses steers the beam and changes the relative position between the micro-pipette and the optical trap [SB05]. In our case, steering is obtained holographically without any mechanical movement.

The principal difficulty of working with DNA is that it is not visible using standard microscopy. To manipulate DNA with guaranties of success a special fluidics chamber is used[†] (fig. 2.14a). This chamber was assembled by using two coverslips separated by means of two nescofilm layers in which a glass micro-pipette and two dispenser tubes are embedded. The thickness of the chamber is about $300\mu m$ and the micropipette is fixed between the two nescofilm layers. Then, the experiment is performed at a depth of $150\mu m$ into the chamber. Usually, oil-immersion objectives are aberration-corrected up to $10\mu m$ of depth [wat00]. When working deeper in the sample, aberration due to the index mismatch between immersion oil and the sample, becomes more important and the optical trap loose trapping capabilities. However, when a water immersion objective is used, there is no index mismatch and this effect disappears, making this kind of objectives suitable to work at deeper distances. In order to use the fluidic chamber in our holographic optical tweezers setup with the water immersion objective, a special holder has been used to place the chamber and the metallic frame with syringe connectors. All the parts of the special setup are shown in figure 2.14b.

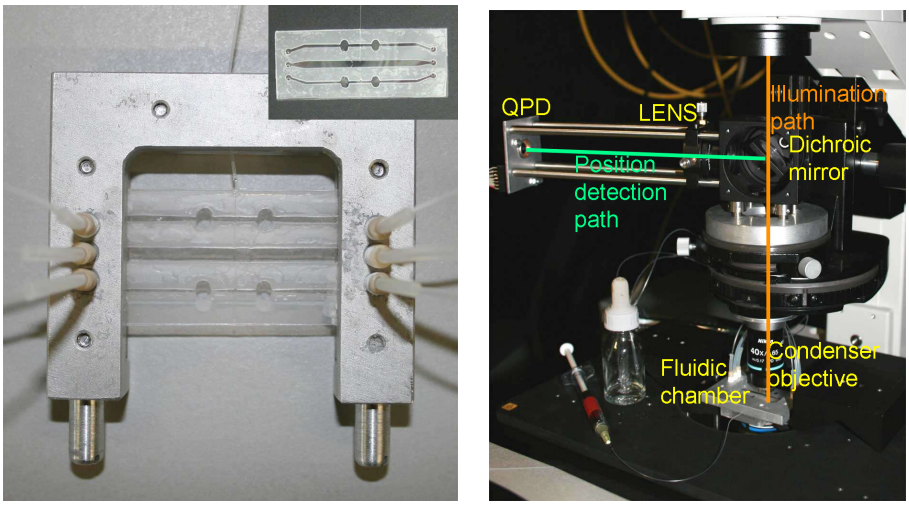


Figure 2.14: a) Fluidic chamber mounted in the metallic frame, tube adaptors in the frame match with the ports of the chamber (inset) b) Calibration setup mounted in the illumination path of the microscope

The experiment is performed in the central channel, which is connected to a syringe with

saline buffer. This solution is used to wash the experimental area. Lateral channels are used to dispense the two different coated beads trough an independent path. In the experiment preparation, the optical tweezers are used to trap each micro-bead coming from the channels and hold it until its displacement to the experimental area. By using the optical trap, we move the streptavidin's coated bead close to the micro-pipette to fix it. The antidigoxigenin's coated bead with an attached DNA-labeled molecule is calibrated and then moved holographically close to the pipette until the free end of the labeled DNA (biotin) is bound to the streptavidin coated bead. When both ends of the DNA molecule are attached to the beads the stretching experiment is ready to start.

The illumination path of the microscope has been modified in order to be able to calibrate optical tweezers. In figure 2.14b, it can be seen that the condenser has been substituted by a $40x$ microscope objective by using a custom adaptor. A second custom adaptor is screwed into the top of the condenser holder. A new optical path is added to the illumination column to collect the refracted laser beam after passing trough the bead. Collected light is focused into a quadrant photodiode sensor to determine the position of the bead as shown in section 2.1.3. Adjustments of this part have been done following the protocol presented in [LRM+07].

Two different LabVIEW programs have been built to store and process the incoming data from the experiment. Quadrant photo diode signals are acquired and digitalized by a National Instruments DAQ PCI card. Images of the sample are acquired by a CCD camera (QImaging). The first program (fig.2.15) is used to calibrate the trap. It records the digitalized signal of the photo diode and determines the calibration parameters using the power spectrum method (see sec. 2.1.3) almost in real-time. The program has the option to save the acquired data into a file for postprocessing. To calibrate the DNA stretching it is necessary to record positions of beads and their displacement from the center of the optical trap. This information is obtained by a second LabVIEW program (fig. 2.16) that records the CCD image and the quadrant sensor signal simultaneously.

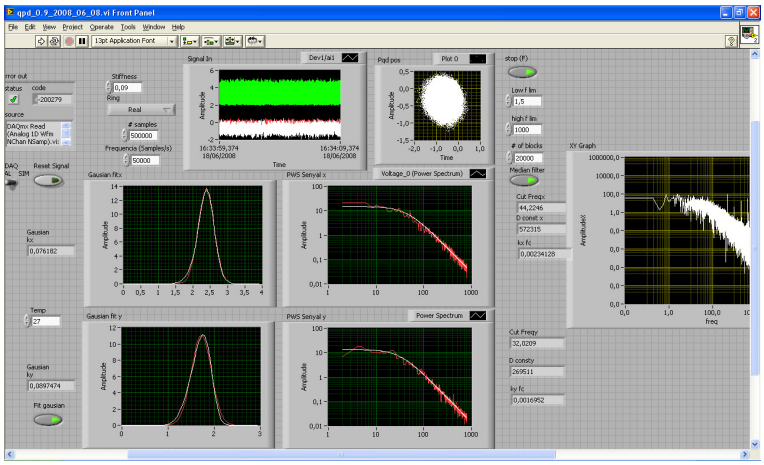


Figure 2.15: Calibration program

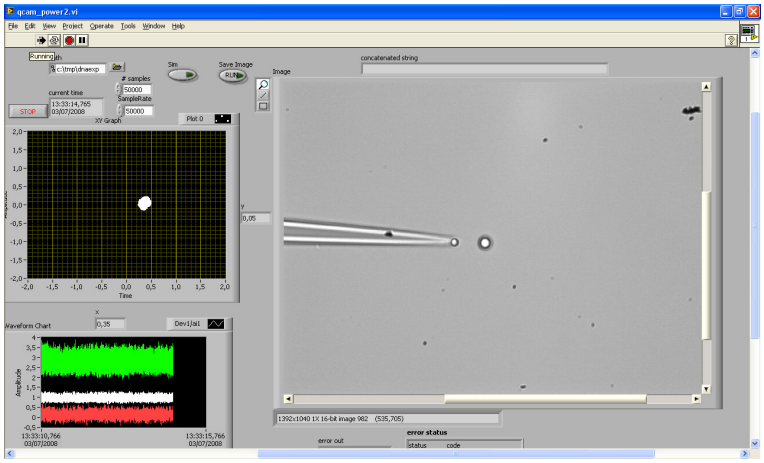

Figure 2.16: DNA stretch program

A simplified software derived from Holotrap (app. D) has been programmed to interact with the sample dynamically. A new feature has been also included into this software. Because neither hardware nor real synchronization system is used, this program is able to generate discrete small displacements of the trap when stretching experiment is performed. This strategy increases time between steps making it possible video and photodiode signal synchronization. The detection of the position of the beads has been performed with a tracking software. Finally to plot the elastic response of the DNA strand it is necessary to calculate from the processed data the distance between beads and the corresponding exerted force in every step.

This preliminary experiment was compared with the data of the experiment using non holographic optical tweezers[†]. The double stranded DNA molecule characteristics were: $24508\,bp$ and $l_0 = 8332.7nm$. Figure 2.17 shows the data obtained with the same molecule characteristics but using the setup presented in [SCB03] (red) versus our experimental data (black). We can see that both curves fit well below $27\,pN$, when the bead escaped from the holographic trap. We set the laser power to have a calibrated trap stiffness of $100\,pN/\mu m$, when using antidigoxigenin coated beads. Their diameter is about $3\mu m$, then, the trap should be able to exert a maximum force on them greater than $100\,pN$ [TMBZ98]. This force should be, in principle, enough to reach the overstretching plateau ($\sim 70pN$). Unfortunately, the trap stiffness drops strongly when the trap is moved holographically [EKL$^+$07]. This happens because every time the hologram is changed, the LCD is updated and, meanwhile, light is diverted away from the trapping region. In the case of this experiment, because of the elastic properties of the DNA strand, and the harmonic behavior of optical tweezers the equilibrium position of the bead is reached when both forces cancel each other. However, when optical force drops due to the hologram change this equilibrium position moves away from center of the optical trap. When elastic forces become larger, there is finally, no equilibrium position between trap and DNA molecule, and the bead escapes.

We demonstrated that DNA stretching experiments using holographic optical tweezers can

reproduce the results obtained using standard optical tweezers systems. For the future, however, some parameters should be adjusted to improve these results. Reducing the step size will reduce the force drop, as shown in [EKL+07]. A similar effect would be obtained using LCDs with faster refresh rates. A deeper comparison with non-holographics technique would also be interesting to analyze both in terms of sensitivity resolution or stiffness changes.

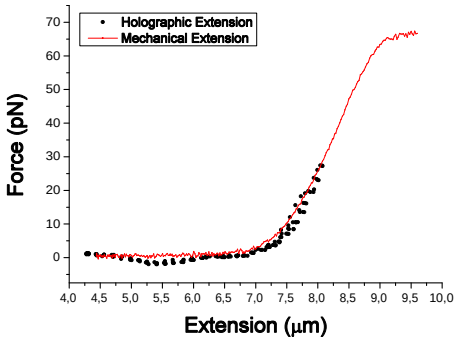


Figure 2.17: DNA stretching force

# Chapter 3

# Conclusions

Optical tweezers experiments evolute toward higher complexities requiring a different *ad hoc* solution for each case. More traps and with more sophisticated control are being increasingly demanded in several application fields. In this thesis we explored the use of holographic optical tweezers in molecular and cell biology as a possible general solution to fully manipulate multiple micro-sized particles. The conclusions of this work follow:

1. We studied the modulation characteristics of LCDs. We developed an automatic method to determine the modulation behavior in terms of Jones matrices for any LCD that behaves as a polarization device. We used this method to find a phase-mostly configuration for the LC-2500R Holoeye LCD when used at an angle of incidence of $45°$.

2. We determined and corrected the aberration produced by the Holoeye LCD. In a first approximation, we found the aberration of the central part of the modulator which consists mainly in as astigmatism and defocus and could be corrected with a toroidal phase. The second more elaborated strategy consists in measuring the wavefront by using a Shack-Hartmann wavefront sensor and then compensate the aberration with the appropriate phase. We achieved an improved flatness of $\lambda/16$

3. We designed and assembled several holographic optical tweezers setups using two LCDs: Holoeye LC-2500R and Hamamatsu X10468-3 working at $532\,nm$ and $1064\,nm$ wavelengths. These were inserted into optical setups based on two different commercial microscopes, the Motic AE31 with an $1.25NA$ oil immersion objective and the Nikon TE2000 equipped both with a $1.3NA$ oil immersion objective and the $1.25NA$ water immersion objective. Furthermore, we used those two systems to trap and manipulate multiple beads simultaneously, with sizes ranging from $200\,nm$ up to $5\,\mu m$ in diameter.

4. We introduced all the characteristics and positions of the optical elements of the system into a numerical simulation to study the effect on trap quality. We determined that, to obtain a diffraction limited spot, the lenses of the second telescope can be singlets

while the lenses of the first telescope, with shorter focal lengths, must be achromatic doublets. The water immersion objective has been also simulated in the infrared range, showing that a diffraction limited spot can obtained in depths up to $270\,\mu m$.

5. We studied the characteristics of prisms and lenses, Gerchberg-Saxton and random masks algorithms for hologram computation of arbitrary patterns of optical trapping. Design trade-offs are clear: the trap efficiency of the Gerchberg-Saxton algorithm is optimized but its computational cost is high. Random masks has a low computational cost but the efficiency is harmed. Prisms and lenses algorithm is halfway between the previous ones and it is sometimes a good compromise. However, the quality of the traps drops significantly when symmetric patterns are required.

6. We implemented a software interface to control holographic traps in-real time using the previous algorithms. We incorporated click-and-drag mouse control of trap positions over a live-video image of the sample. We obtained up to $16fps$ using the random masks algorithm with a standard PC (PIV HT 3.4GHz).

7. We established and maintained a NG-108 cell line during months. Adaptation to the new culture mediums and slight modifications of the thaw and freezing protocols were necessary to obtain a suitable quantity of viable frozen cells.

8. We built special equipment to maintain mammalian cells on the microscope stage with controlled environmental conditions, which consisted of a Petri dish with modified bottom glass and a special top cover. Dish and objective heaters were incorporated into this micro-incubation chamber. We modified the specific protocols to culture the cells on the bottom glass dishes.

9. We used the holographic optical tweezers workstation to interact with micro-vesicles carried by molecular motors inside living cells. We used a previous result from Ashkin to estimate the force produced by the motor that pulled the vesicle. We found that this force was with the dynein stall force ($1.1\,pN$).

10. We demonstrated a DNA stretching experiment using holographic optical tweezers. Some critical problems of the holographic technique have been identified. We proposed some improvements that should be carried out to overcome these problems in the future.

# Appendix A

## Prediction of phase-mostly modulation for holographic optical tweezers

Published in

Optics Communications
Vol.: 281, Issue: 14, Jul. 2008

Available online at www.sciencedirect.com
ScienceDirect
Optics Communications 281 (2008) 3786–3791
OPTICS COMMUNICATIONS
www.elsevier.com/locate/optcom

# Prediction of phase-mostly modulation for holographic optical tweezers

J. Andilla *, E. Martín-Badosa, S. Vallmitjana

*Grup de Recerca en Òptica Física, Departament de Física Aplicada i Òptica, Universitat de Barcelona, Martí i Franquès, 1, Barcelona 08028, Spain*

Received 16 January 2008; received in revised form 21 March 2008; accepted 22 March 2008

**Abstract**

We characterize a reflective Holoeye LC-R 2500 spatial light modulator with a technique in which Jones matrices describing its polarization capabilities are obtained and then used for any arbitrary configuration. We apply this method to predict a phase-mostly modulation response with minimum amplitude contrast and a phase modulation range close to $2\pi$ rad. This allows us to generate multiple traps in a holographic optical tweezers setup with high light efficiency and hardly any unwanted energy on the zero diffraction order.


*Keywords:* Holographic optical tweezers; Spatial light modulators

## 1. Introduction

Optical tweezers are strongly focused laser beams capable of trapping microscopic particles [1]. Optical tweezers have been proved to be a very valuable and useful tool for grabbing, holding, exerting and measuring forces in micron-sized objects in liquids, with huge and promising applications in molecular and cell biology [2]. A major improvement in optical tweezers has been brought about by the introduction of holograms displayed onto spatial light modulators (SLMs) [3–6]. With these devices in the setup, the laser wavefront can be spatially modified prior to the focusing step, resulting in a completely programmable intensity pattern over the sample plane. Large arrays of optical traps, three-dimensional position control or traps with exotic properties are among the new possibilities of holographic optical tweezers [6,7].

Unfortunately, liquid crystal SLMs are unable to modulate the whole unit circle in complex space [8], that is, they are incapable of modifying both phase and amplitude of the incoming wavefront on an independent basis. They are constrained to modulate along one-dimensional manifolds through the complex plane, normally coupling phase and amplitude [9]. On the other hand, the modulation capabilities of SLMs depend both on the polarization state of incident light and on the polarizing elements placed at the exit. These give rise to different operating configurations. Most frequently the SLM is set to a phase-mostly configuration, in order to maximize trapping strength. For this configuration, there is almost uniform amplitude modulation and, ideally, a maximum phase shift of $2\pi$ rad. These conditions are inherently satisfied for parallel nematic liquid crystal SLMs having a cell thickness adjusted to the illuminating wavelength [10–12]. However, in low-cost applications cheaper devices used for image projection are normally preferred. They are based on a twisted nematic liquid crystal cell and are designed to optimize contrast. Nevertheless, by choosing a suitable configuration they can also provide phase-mostly modulation [9,13–15], normally by using elliptically polarized incident light and by placing an analyzer at the exit [16–18]. Improvements of the technology have led to an increase in pixel resolution through a reduction in cell thickness, and thus an unwanted decrease in phase modulation range [19]. Lately, liquid crystal on silicon (LCoS) SLMs, which operate by reflection in a double-pass beam path, have

* Corresponding author. Tel.: +34 934021142; fax: +34 934039219.
*E-mail address:* jordi.andilla@ub.edu (J. Andilla).
*URL:* http://www.ub.edu/optics (J. Andilla).

0030-4018/$ - see front matter © 2008 Elsevier B.V. All rights reserved.
doi:10.1016/j.optcom.2008.03.067

overcome this difficulty and have been proved to be a widespread solution such as, for example, Holoeye reflective twisted nematic liquid crystal devices [20].

Often those using them in holographic optical tweezers are not able to decouple phase modulation from amplitude modulation [21], and thus obtain a bright unwanted zeroth-order diffraction spot [22]. Besides losing light, this central ghost trap needs to be removed. Researchers usually separate the desired pattern of traps and the zero-order beam by adding a linear phase to the computed holograms [23–25], and then block the zero order by a spatial filter [26,27]. The central term and thus energy loss could be minimized if the modulation capabilities of the device were accurately known and a suitable phase-mostly configuration could be selected and measured.

SLM characterization consists in determining the amplitude and phase modulation for the different grey levels addressed on it, for each configuration [15]. This can be quite time-consuming, especially when trying to find a suitable configuration by rotating the polarizing elements placed before and after the device. Some calibration methods assume a model for the modulator and measure the characteristic parameters of the device [9,28–30]; this allows the deduction of operating curves corresponding to different configurations. In [31] a technique for determining the Jones matrix describing SLM polarization capabilities is presented, assuming that a modulator is a non-absorbing polarization device. Again, the modulation response can be predicted and thus optimized for any configuration. Another approach is also introduced in [32] to achieve phase-mostly modulation with a TNLC.

In this paper we present an alternative method to that of reference [31], in which the only assumption is that the modulator behaves as a polarization device and thus can be described by a Jones matrix having no constraints. We use this method to determine Jones matrices of a Holoeye LC-R 2500 reflective liquid crystal SLM [33], for the different gray-level values that can be displayed on it. The SLM makes an angle of 45° degrees with the incident collimated laser beam ($\lambda = 532$ nm), as used in a holographic optical tweezers setup (see [34]). A phase-mostly configuration is then determined by minimizing the computed amplitude modulation, and used for the generation of multiple traps.

## 2. Jones matrix determination procedure

The Jones matrix of a polarization device can be written, in the general case, as

$$\mathbf{M} = A\mathrm{e}^{\mathrm{i}\Phi}\begin{pmatrix} m_{11} & m_{12} \\ m_{21} & m_{22} \end{pmatrix}, \tag{1}$$

where $A$ and $\Phi$ are a global amplitude and a global phase shift, respectively, and the matrix elements $m_{11}$, $m_{12}$, $m_{21}$ and $m_{22}$ are complex values. An input state of polarization represented by a Jones vector $\mathbf{J}_\mathrm{i}$ is transformed onto a polarization state $\mathbf{J}_\mathrm{o}$ when traversing a polarization-state converter, characterized by the Jones matrix $\mathbf{M}$, so that

$$\mathbf{J}_\mathrm{o} = \mathbf{M}\cdot\mathbf{J}_\mathrm{i}. \tag{2}$$

From three input polarization states ($\mathbf{J}_{\mathrm{i}1}$, $\mathbf{J}_{\mathrm{i}2}$ and $\mathbf{J}_{\mathrm{i}3}$) and the corresponding output polarization states of light ($\mathbf{J}_{\mathrm{o}1}$, $\mathbf{J}_{\mathrm{o}2}$ and $\mathbf{J}_{\mathrm{o}3}$) it is possible to obtain $\mathbf{M}$ [35], as we will see below. We will first describe how to determine these polarization states of light (Jones vectors).

### 2.1. Determination of Jones vectors

The Jones vector for a fully polarized wave front propagating in the $z$-direction described by the perpendicular electric fields having amplitudes $A_x$ $A_y$ and phases $\delta_x$ and $\delta_y$ can be written:

$$\mathbf{J} = \begin{pmatrix} A_x\mathrm{e}^{\mathrm{i}\delta_x} \\ A_y\mathrm{e}^{\mathrm{i}\delta_y} \end{pmatrix} = \sqrt{I}\mathrm{e}^{\mathrm{i}\phi}\begin{pmatrix} \chi \\ 1 \end{pmatrix}, \tag{3}$$

where

$$\chi = \tan(\psi)\mathrm{e}^{\mathrm{i}\Delta}\begin{cases} \tan(\psi) = \frac{A_x}{A_y} & (0 \leqslant \psi \leqslant \pi/4), \\ \Delta = \delta_x - \delta_y & (0 \leqslant \Delta \leqslant 2\pi). \end{cases} \tag{4}$$

The complex number $\chi$ or its modulus and argument ($\tan(\psi)$, $\Delta$) describe the polarization state of light (the intensity $I$ and the global phase factor $\phi$ are not relevant). It can be determined by analyzing the periodical signal measured by a light intensity detector placed behind a rotating linear polarizer, which is the principle of operation of a rotating analyzer ellipsometer [35]. If $\theta_k$ is the angle between the transmission axis of the polarizer and the $x$-axis and $I(\theta_k)$ is the intensity of the light transmitted by the polarizer, it can be shown that $\psi$ and $\Delta$ are related to the normalized cosine and sine Fourier coefficients $i_\mathrm{c}$ and $i_\mathrm{s}$ by

$$\begin{aligned} i_\mathrm{c} &= -\cos(2\psi), \\ i_\mathrm{s} &= \sin(2\psi)\cos(\Delta), \end{aligned} \tag{5}$$

where

$$\begin{aligned} i_\mathrm{c} &= \frac{\frac{2}{N}\sum_{k=1}^{N} I(\theta_k)\cos(2\theta_k)}{\frac{1}{N}\sum_{k=1}^{N} I(\theta_k)} \\ i_\mathrm{s} &= \frac{\frac{2}{N}\sum_{k=1}^{N} I(\theta_k)\sin(2\theta_k)}{\frac{1}{N}\sum_{k=1}^{N} I(\theta_k)} \end{aligned}. \tag{6}$$

Here, $N$ is the number of points of the measured digitized signal $I(\theta_k)$.

The coefficients $\psi$ and $\Delta$ can be found from Eq. (5). The sign of $\Delta$ (whether the polarization state of light is left-handed or right-handed), though, is undetermined, as both $\Delta$ and $-\Delta$ give the same values of $i_\mathrm{c}$ and $i_\mathrm{s}$. By taking another measurement of the light transmitted by the system for $\theta_k = 0$ and when a quarter-wave plate is placed before the polarizer with two different orientations, it is possible to find out the sign of $\Delta$: for a given $\mathbf{J}_\mathrm{i}$, the Jones vector after a quarter-wave plate placed at ±45° and a polarizer at angle 0 is

$$\mathbf{J}_{\pm 45} = \mathbf{P}(0)\cdot\mathbf{R}(\mp 45)\cdot\mathbf{L4}(0)\cdot\mathbf{R}(\pm 45)\cdot\mathbf{J}_\mathrm{i}. \tag{7}$$

Table 1
Some examples of Jones matrices

| Linear polarizer parallel to the $x$-direction | Quarter-wave plate, fast axis on the $y$-direction | Rotation (coordinate transformation) |
|---|---|---|
| $P(0)=\begin{pmatrix}1 & 0\\ 0 & 0\end{pmatrix}$ | $L4(0)=\begin{pmatrix}1 & 0\\ 0 & -\mathrm{i}\end{pmatrix}$ | $R(\theta)=\begin{pmatrix}\cos\theta & \sin\theta\\ -\sin\theta & \cos\theta\end{pmatrix}$ |

Jones matrices $\mathbf{P}(0)$, $\mathbf{L4}(0)$ and $\mathbf{R}(\theta)$ are indicated in Table 1.

By comparing the intensities after the polarizer in both cases,

$$|\mathbf{J}_{\pm 45}|^2 \propto 1 \pm \sin\Delta \sin 2\psi, \tag{8}$$

the sign of $\Delta$ can be determined.

### 2.2. Determination of Jones matrices

Going back to Eq. (1), the Jones matrix $\mathbf{M}$ of a given system can be found from three input polarization states described by $\chi_{i1}$, $\chi_{i2}$ and $\chi_{i3}$ and the corresponding output polarization states of light $\chi_{o1}$, $\chi_{o2}$ and $\chi_{o3}$, according to [35]:

$$\begin{aligned} m_{11} &= \chi_{i2} - \chi_{i1}H \\ m_{12} &= H - 1 \\ m_{21} &= \chi_{i2}\chi_{o1} - \chi_{i1}\chi_{o2}H \\ m_{22} &= -\chi_{o1} + \chi_{o2}H \end{aligned} \qquad H = \frac{(\chi_{o3}-\chi_{o1})(\chi_{i3}-\chi_{i2})}{(\chi_{o3}-\chi_{o2})(\chi_{i3}-\chi_{i1})} \tag{9}$$

Absolute amplitude and phase factors $A$ and $\Phi$ cannot be determined with this method as in the definition of $\chi$ itself only relative quantities are involved. We have retrieved $A$ by comparing the ratio of the measured intensities $I(\theta_k)$ for the input and the corresponding output polarization states of light; however, the overall phase factor $\Phi$ should be measured separately by interferometric techniques (see the details in Section 2.3).

### 2.3. Modulator response: amplitude and phase

Assuming that a modulator behaves as a polarization device, a Jones matrix $\mathbf{M}(g)$ for each gray level $g$ displayed on it can be determined with the method described above. Then, amplitude and phase modulation can be predicted for any configuration: if $\mathbf{J}_i$ describes the polarization state of light incident on the SLM, which can be generated with a polarizer and a quarter-wave plate (oriented at $\theta_P$ and $\theta_{L4}$, respectively):

$$\mathbf{J}_i = \mathbf{R}(-\theta_{L4})\cdot L4(0)\cdot \mathbf{R}(\theta_{L4})\cdot \mathbf{R}(-\theta_P)\cdot \mathbf{P}(0)\cdot \mathbf{R}(\theta_P), \tag{10}$$

and a linear polarizer (analyzer) is placed at the exit (oriented at $\theta_A$), the output Jones vector expressed in the analyzer frame of reference is

$$\mathbf{J}_{out}(g) = \mathbf{P}(0)\cdot \mathbf{R}(\theta_A)\cdot \mathbf{M}(g)\cdot \mathbf{J}_i \equiv e^{i\Phi(g)}\begin{pmatrix}\rho(g)e^{i\alpha(g)}\\ 0\end{pmatrix}. \tag{11}$$

Here, $\rho(g)$ and $\alpha(g)+\Phi(g)$ are the amplitude and phase modulation for the considered gray level $g$ having Jones matrix equal to $\mathbf{M}(g)$. We have split the phase into two terms: phase $\alpha(g)$ derived from Jones matrix elements $m_{11}$, $m_{12}$, $m_{21}$ and $m_{22}$ and external phase $\sigma(g)$ (see Eq. (1)). The latter can be determined by measuring experimentally the global phase modulation $\alpha(g)+\Phi(g)$ for a single configuration (values of $\theta_P$, $\theta_{L4}$ and $\theta_A$) and then subtracting the computed value $\alpha(g)$ from it.

## 3. Experimental realization and results

### 3.1. Experimental setup

We used the procedure explained above to determine the Jones matrix of a Holoeye LC-R 2500 reflective liquid crystal SLM [33], for each of the 256 grey-level values displayed on it. The SLM has 1024 × 768 pixels with a pixel pitch of 19 μm. Fig. 1a shows a sketch of the experimental setup: a Nd:$YVO_4$ laser beam ($\lambda = 532$ nm, 120 mW) is expanded and filtered and then collimated by lens L1. Different input polarization states of light ($\mathbf{J}_i$) are achieved with the polarizer and half-wave plate placed before the SLM. The sketch shows the ellipsometer (rotating analyzer and detector) placed behind the SLM to determine the output polarization states $\mathbf{J}_o$. To determine the input polarization states the ellipsometer should be located just before the SLM. We also indicate the reference frame: all angles are measured

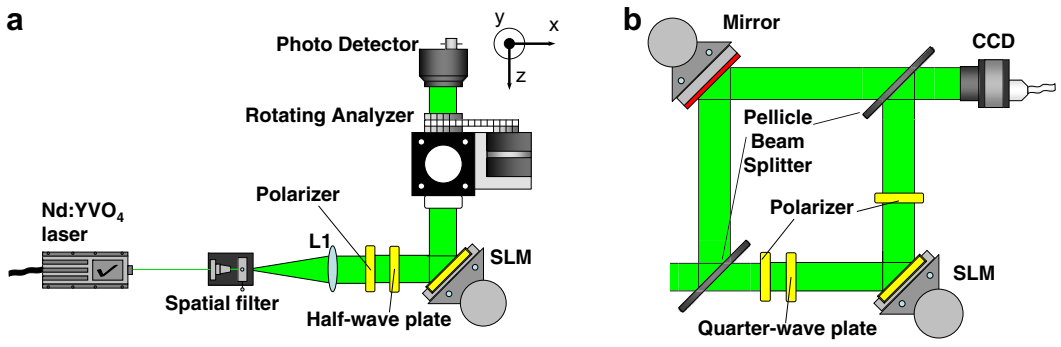


Fig. 1. Sketch of the experimental setup: (a) rotating analyzer ellipsometer, (b) Mach–Zehnder interferometer used for phase determination.

counter-clockwise from the horizontal ($x$) direction, when looking at the side first touched by the laser. SLM' shortest side (768 pixels) is parallel to the $y$-direction.

Note that the modulator is placed at 45° with respect to the incident beam, as it is going to be used in a holographic optical tweezers setup. The usual configuration for a reflective modulator is to place it perpendicular to the beam and then redirect the beam with a non-polarizing beam-splitter. This allows, by controlling the input and output polarization, free access to the different operating modes of the device. The round trip path through a non-polarizing beam-splitter would result in a loss of 75% of the incident light. This is unacceptable in a holographic optical tweezers setup, considering the large power required for trapping even a small number of samples, so we discarded that possibility in favor of that depicted in Fig. 1a.

Fig. 1b shows a sketch of the Mach-Zehnder interferometer used to determine Jones matrix external phase $\Phi(g)$ for each gray level of the SLM. The collimated laser beam is split by the first beam-splitter. A CCD camera registers the interference fringes between two plane waves when the two beams recombine again. The phase variation produced when the SLM is placed in one arm of the interferometer is transferred onto a fringe displacement on the interference plane, and can be computed with the method described in [15]. The orientation of the quarter-wave plate and polarizers are used to select one configuration of the device.

### 3.2. Jones matrices

Jones matrices of 32 evenly spaced gray-level values written on the modulator are automatically obtained with the method described above. Figs. 2a and b show Jones matrices complex elements

$$M_{kl}(g) = A(g)e^{i\Phi(g)}m_{kl}(g) \quad (k,l = 1,2) \tag{12}$$

(The values of the other gray levels ranging from 0 to 255 have been computed by linear interpolation).

In the procedure, we first determine $m_{11}(g)$, $m_{12}(g)$, $m_{21}(g)$ and $m_{22}(g)$ from ellipsometric measurements. Then, global phase modulation $\alpha(g) + \sigma(g)$ is measured by interferometric techniques once, for a given configuration. In order to check the characterization technique, we have verified that different configurations yield the same results for the external phase, $\sigma(g)$. However, when determining the global amplitude factor $A(g)$ by computing the ratio between the measured intensities $I(\theta_k)$ for the input and output polarization states of light, we find that the result slightly depends on the chosen configuration. We think this might be due to the following reasons: (i) the SLM not being uniform, its response changes from pixel to pixel; as the area of the light beam in the intensity detector (about 3 mm in diameter) covers quite a lot of pixels, the results obtained here are an average of their different responses; (ii) the SLM might slightly depolarize the incident light beam [36]; in this case, Mueller matrices taking into account depolarization effects should be considered, instead of Jones matrices [37].

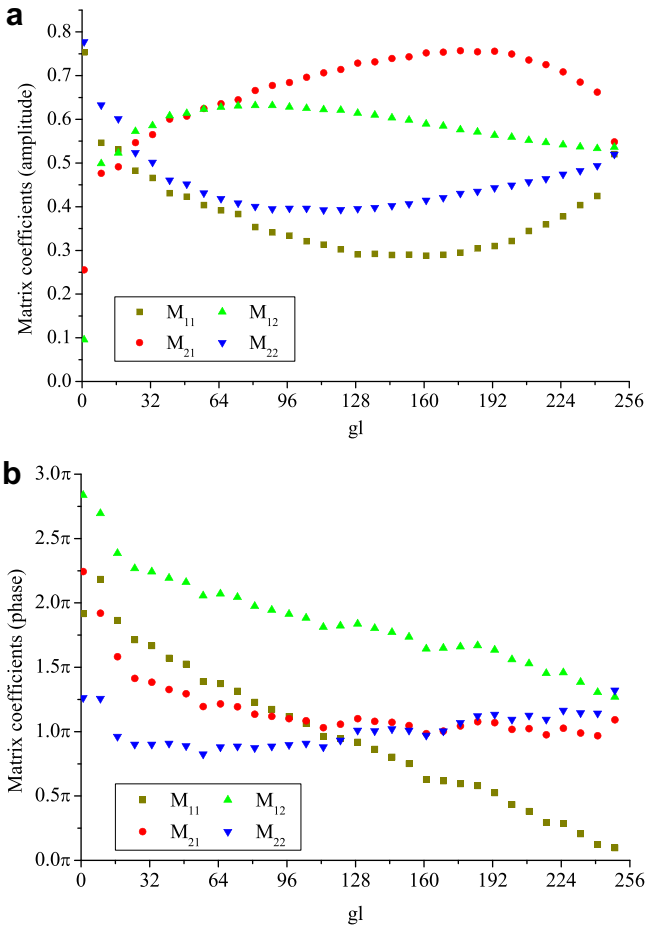


Fig. 2. Jones matrices elements for each gray level $g$ (0–255) displayed on the SLM: (a) amplitude, (b) phase.

In any case, we will presume that Jones formulism still applies and will consider an average $A(g)$ factor. We will next validate the characterization method by comparing the modulation response simulated from the computed Jones matrices with direct amplitude and phase modulation measurements.

### 3.3. Phase-mostly configuration prediction and application to holographic optical tweezers

The knowledge of Jones matrices describing SLM behavior allows us to simulate and predict the modulator response for any configuration. We have computed amplitude and phase modulation for arbitrary configurations, as described in Section 2.3. Phase-mostly configuration is found by minimizing the amplitude contrast while keeping a phase modulation range close to $2\pi$ rad. We have found different configurations yielding similar results, both with elliptically or linearly polarized incoming light. For the sake of simplicity, we have chosen a solution in which the modulator is sandwiched between two linear polarizers,

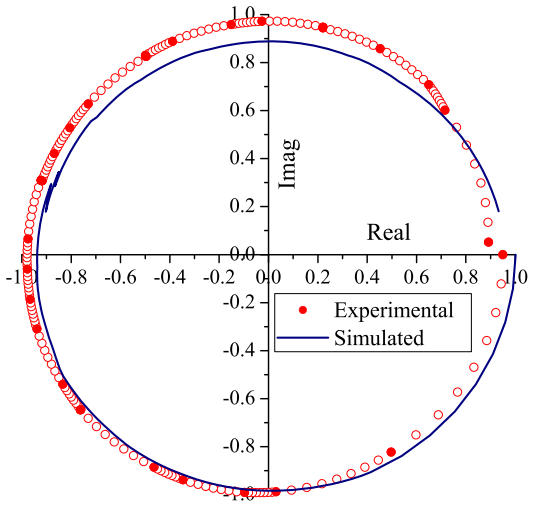


Fig. 3. Phase-mostly configuration: prediction (simulated) and experimental data.

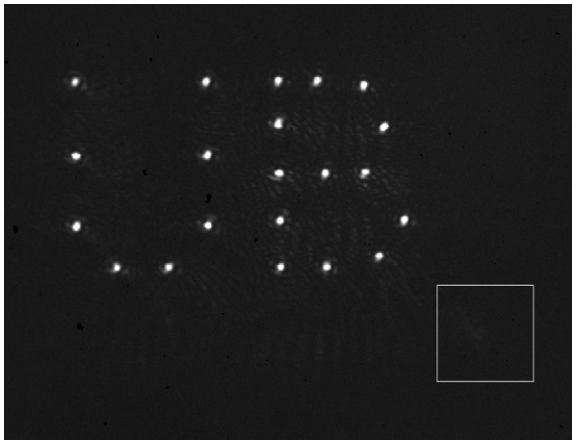

Fig. 4. Holographic traps when the phase-mostly configuration is used. The box shows the zero diffraction term.

oriented at $\theta_P = -45°$ and $\theta_A = 26°$, according to sign convention of Section 3.1. Fig. 3 shows a comparison between the predicted modulation response and the operating curve measured with standard techniques [15] (32 gray-level values were measured, the others were obtained by interpolation). Amplitude is normalized to one in both cases (the absolute value is around 0.8). Experimental and simulated curves give similar results, better on phase modulation than on amplitude modulation, due to the compromise averaged $A(g)$ factor: maximum phase shift 1.98π rad (experimental) or 1.94π rad (simulated), intensity contrast 1:1.13 (experimental) or 1:1.27 (simulated). Other authors [38,39] have reported phase-mostly configurations for the same modulator making a different angle with the incident light: although they reach a maximum phase shift of 1.98π rad, the intensity contrast is only around 1:3. Others mention trying to optimize phase efficiency whether with input and exit linear polarizers (for Holoeye LC2002) [40] or by placing a polarizer at the entrance but no analyzer at the exit [27]. We think this is a widespread non-optimal solution that might explain the unwanted brightness of the zero diffraction order.

We have used our phase-mostly configuration in a holographic optical tweezers setup [34]: Fig. 4 shows the experimental trap pattern when a multiple-trap hologram is computed by the Gerchberg–Saxton algorithm [41]. As we can see, energy concentrates on the desired traps and not on the central undiffracted beam, which nearly vanishes. This is due to the modulator response only introducing phase shifts with very low amplitude contrast, and avoids unwanted traps in the central field of view.

By using Jones matrices of the SLM we can predict other configurations that might be interesting for our applications. Our modulator was initially purchased to work at 532 nm, while near infrared lasers (typically, 1064 nm) should be used to trap biological specimens without optical damage. Bearing in mind that birefringence is inversely proportional to wavelength, one would expect that an SLM illuminated by infrared light instead of visible light would have a lesser range in phase modulation. We have analyzed which is the maximum phase shift of our Holoeye device (even at the expense of having amplitude modulation), to estimate whether we can still use it at longer wavelengths than 532 nm. Even when using elliptical polarized light, we have only reached phase shifts around 2.5π rad (at 532 nm), which seem rather insufficient. The graphs given by the manufacturer for perpendicular incidence yield to similar conclusions: while the phase modulation range is about 2.7π rad for 543 nm, it is reduced to 1.4π rad for 1064 nm. This means that using the same modulator at infrared wavelengths would not be straightforward, as this restriction in phase modulation range should be taken into account in hologram computation.

## 4. Conclusion

In this paper, we predict and find a phase-mostly modulation curve for a Holoeye LC-R 2500 SLM making an angle of 45° with the incident light ($\lambda = 532$ nm). We have seen that this can be achieved by sandwiching the modulator between two linear polarizers, with no need of using a quarter-wave plate to generate elliptically polarized input light. The prediction is made from the determination of Jones matrices of the modulator, for each gray level displayed on it. We have validated the characterization method by comparing the predicted curve with results obtained with standard techniques. The correspondence between theoretical and experimental results is better on phase than on amplitude modulation, and could be improved if non-uniformity and depolarization effects of the SLM were taken into account. This would require pixel by pixel Mueller matrix determination and is beyond the scope of this work. Here, we have proved that an easier approach can still help us to predict the modulation properties of our SLM. For example, we have learned that the maximum phase modulation range of our device (2.5π

rad) is too short for the modulator to operate at longer wavelengths.

Finally, the predicted phase-mostly modulation is used in a holographic optical tweezers setup with high light efficiency and almost no undesired energy concentrated on the zero diffraction order. Thus, there is no need to separate the desired pattern of traps from the centre and then block the unwanted term. This shows that rather low-cost spatial light modulators are a suitable solution for holographic optical tweezers, especially if used in optimized conditions.

## Acknowledgements

We acknowledge Dr. M. Montes-Usategui and Dr. S. Bosch for many fruitful discussions and E. Pleguezuelos for the generation of the hologram to obtain the traps of Fig. 4. This work was funded by the Spanish Ministry of Education and Science, under Grants FIS2004-03450 and NAN2004-09348-C04-03.

## References

[1] A. Ashkin, J.M. Dziedzic, J.E. Bjorkholm, S. Chu, Opt. Lett. 11 (1986) 288.
[2] M.J. Lang, S.M. Block, Am. J. Phys. 71 (2003) 201.
[3] M. Reicherter, T. Haist, E.U. Wagemann, H.J. Tiziani, Opt. Lett. 24 (1999) 608.
[4] J. Liesener, M. Reicherter, T. Haist, H.J. Tiziani, Opt. Commun. 185 (2000) 77.
[5] E.R. Dufresne, G.C. Spalding, M.T. Dearing, S.A. Sheets, D.G. Grier, Rev. Sci. Instr. 72 (2001) 1810.
[6] J.E. Curtis, B.A. Koss, D.G. Grier, Opt. Commun. 207 (2002) 169.
[7] D.G. Grier, Nature 424 (2003) 810.
[8] R. Tudela, E. Martín-Badosa, I. Labastida, S. Vallmitjana, I. Juvells, A. Carnicer, J. Opt. A: Pure Appl. Opt. 5 (2003) S189.
[9] K. Lu, B.E.A. Saleh, Opt. Eng. 29 (1990) 240.
[10] <http://sales.hamamatsu.com/en/products/electron-tube-division/detectors/spatial-light-modulator.php>.
[11] <http://www.bnonlinear.com/products/XYphase/XYphase.htm>.
[12] <http://www.holoeye.com/phase_only_modulator_heo1080p.html>.
[13] N. Konforti, E. Marom, S.-T. Wu, Opt. Lett. 13 (1988) 251.
[14] L.G. Neto, D. Roberge, Y. Sheng, Appl. Opt. 34 (1995) 1944.
[15] E. Martín-Badosa, A. Carnicer, I. Juvells, S. Vallmitjana, Meas. Sci. Technol. 8 (1997) 764.
[16] J.A. Davis, I. Moreno, P. Tsai, Appl. Opt. 37 (1998) 937.
[17] J. Nicolás, J. Campos, M.J. Yzuel, J. Opt. Soc. Am. A 19 (2002) 1013.
[18] V. Arrizón, L.A. González, R. Ponce, A. Serrano-Heredia, Appl. Opt. 44 (2005) 1625.
[19] I. Labastida, A. Carnicer, E. Martín-Badosa, S. Vallmitjana, I. Juvells, Appl. Opt. 39 (2000) 766.
[20] <http://www.holoeye.com/spatial_light_modulators-technology.html>.
[21] D. Cojoc, S. Cabrini, E. Ferrari, R. Malureanu, M.B. Danailov, E. Di Fabrizio, Microelectron. Eng. 73-74 (2004) 927.
[22] S.C. Chapin, V. Germain, E.R. Dufresne, Opt. Express 14 (2006) 13095.
[23] G. Sinclair, P. Jordan, J. Courtial, M. Padgett, J. Cooper, Z.J. Laczik, Opt. Express 12 (2004) 5475.
[24] C.M. Creely, G. Volpe, G.P. Singh, M. Soler, D.V. Petrov, Opt. Express 13 (2005) 6105.
[25] A. Jesacher, S. Fürhapter, C. Maurer, S. Bernet, M. Ritsch-Marte, Opt. Lett. 31 (2006) 2824.
[26] A. Jesacher, S. Fürhapter, S. Bernet, M. Ritsch-Marte, Opt. Express 12 (2004) 4129.
[27] D.R. Burnham, D. McGloin, Opt. Express 14 (2006) 4175.
[28] J.A. Coy, M. Zaldarriaga, D.F. Grosz, O.E. Martínez, Opt. Eng. 35 (1996) 15.
[29] A. Márquez, C. Iemmi, I. Moreno, J. Davis, J. Campos, M. Yzuel, Opt. Eng. 40 (2001) 2558.
[30] M. Yamauchi, Appl. Opt. 44 (2005) 4484.
[31] I. Moreno, P. Velásques, C.R. Fernández-Pousa, M.M. Sánchez-López, F. Mateos, J. Appl. Phys. 94 (2003) 3697.
[32] V. Durán, J. Lancis, E. Tajahuerce, M. Fernández-Alonso, Opt. Express 14 (2006) 5607.
[33] <http://www.holoeye.com/spatial_light_modulator_lc_r_2500.html>.
[34] E. Martín-Badosa, M. Montes-Usategui, A. Carnicer, J. Andilla, E. Pleguezuelos, I. Juvells, J. Opt. A: Pure Appl. Opt. 9 (2007) S267.
[35] R.M.A. Azzam, N.M. Bashara, Ellipsometry and Polarized Light, Elsevier Science B.V., Amsterdam, 1999.
[36] J.L. Pezzaniti, S.C. McClain, R.A. Chipman, S.-Y. Lu, Opt. Lett. 18 (1993) 2071.
[37] J.E. Wolfe, R.A. Chipman, Appl. Opt. 45 (2006) 1688.
[38] C. Kohler, X. Schwab, W. Osten, Appl. Opt. 45 (2006) 960.
[39] M. Reicherter, S. Zwick, T. Haist, C. Kohler, H. Tiziani, W. Osten, Appl. Opt. 45 (2006) 888.
[40] S. Sundbeck, I. Gruzberg, D.G. Grier, Opt. Lett. 30 (2005) 477.
[41] R.W. Gerchberg, W.O. Saxton, Optik 35 (1972) 237.

# Appendix B

## Design strategies for optimizing holographic optical tweezers set-ups

Published in

Journal of Optics A: Pure and Applied Optics
Issue:9 S267, Jul. 2007

IOP Publishing Journal of Optics A: Pure and Applied Optics
J. Opt. A: Pure Appl. Opt. **9** (2007) S267–S277 doi:10.1088/1464-4258/9/8/S22

# Design strategies for optimizing holographic optical tweezers set-ups

**E Martín-Badosa, M Montes-Usategui, A Carnicer, J Andilla, E Pleguezuelos and I Juvells**

Grup de Recerca en Òptica Física-GROF, Departament de Física Aplicada i Òptica, Universitat de Barcelona, Martí i Franquès 1, Barcelona E-08028, Spain

E-mail: estela.martinb@ub.edu

Received 2 January 2007, accepted for publication 29 June 2007
Published 25 July 2007
Online at stacks.iop.org/JOptA/9/S267

**Abstract**
We provide a detailed account of the construction of a system of holographic optical tweezers. While a lot of information is available on the design, alignment and calibration of other optical trapping configurations, those based on holography are relatively poorly described. Inclusion of a spatial light modulator in the set-up gives rise to particular design trade-offs and constraints, and the system benefits from specific optimization strategies, which we discuss.

**Keywords:** holographic optical tweezers, spatial light modulators, optical design

(Some figures in this article are in colour only in the electronic version)

## 1. Introduction

The introduction of holographic optical elements into optical tweezer set-ups has multiplied the possibilities of this technology for precisely trapping, moving and manipulating microparticles. First, static diffractive optical elements generated by computer and manufactured by photolithography enabled the simultaneous creation of several optical traps [1, 2]. Conversion of the static trap arrays into dynamic light patterns by displaying the diffractive optical elements on spatial light modulators was the logical next step [3–6].

These special displays can be updated at video rates, so that with every new diffractive element a completely different optical potential is formed at the sample plane. Furthermore, holographic optical tweezers have an advantage over other methods of dynamic light array generation, such as time sharing [7], in that the modulator spatially modifies the phase of the incoming wavefronts. Wavefront control easily permits three-dimensional positioning of the traps as well as the creation of beams with special characteristics, such as Bessel or Laguerre–Gaussian beams [8] that carry angular momentum.

In just a few years holographic optical tweezers have become a research topic with many potential applications [9] and thus have turned into a subfield of optical trapping of particular importance and projection. New applications are being proposed in many fields ranging from microfluidics [10, 11] to nanotechnology [12] and biophysics [13]. However, contrary to single-beam technology, which has been thoroughly documented in its many facets [14–18], holographic optical tweezers systems remain comparatively poorly described. The inclusion of the spatial light modulator in the optical set-up has important design implications that are specific to this technology. Also, the system may benefit from particular optimization strategies that are worth showing and discussing.

The goal of this paper is to help fill this gap by carefully describing and analysing the design and construction of a system of holographic optical tweezers, a subject that we have divided into three main parts. Section 2 analyses the optical system constraints and reveals the trade-offs between optical efficiency and resulting layout size. Several practical tips and design proposals for two different systems are also included here. We believe that the results contained in this section are of wide applicability. Section 3 is devoted exclusively to the spatial light modulator and includes information that is more dependent on the particular device that we use. The three subsections deal with phase-only modulation adjustment, angular dependence of the reconstructed holograms and correction of the built-in optical aberrations of the device. Finally, section 4 contains a complete analysis of the optical

  

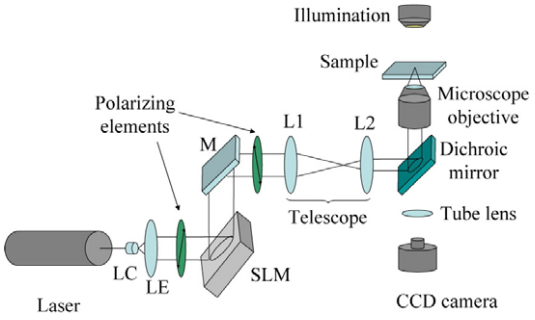


**Figure 1.** Diagram of the holographic optical tweezers set-up.

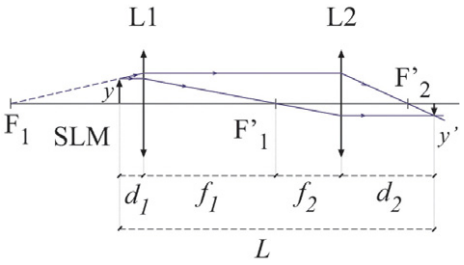


**Figure 2.** Ray tracing diagram showing the image formation through the telescope L1–L2.

aberrations of the resulting optical systems and suggestions on how to achieve diffraction-limited performance with very simple lenses.

## 2. Design of the optical set-up

### *2.1. Optical system constraints*

Figure 1 shows a diagram of a system of holographic optical tweezers. A continuous-wave, $TEM_{00}$ laser beam is first expanded and then collimated by lenses LE and LC. A pinhole spatially filters the light at the back focal plane of the expander lens to ensure clean, Gaussian illumination on the spatial light modulator (SLM). The modulator, which may operate either by reflectance or transmittance, is sandwiched between polarizing elements with specific orientations that depend on the configuration desired (see section 3). After passing through a telescope, the beam is reflected upwards by a dichroic mirror and is focused by the high numerical aperture microscope objective on the sample plane. Usually, this latter step takes place inside a commercial inverted microscope, so that the illumination system, objective lens and other optical elements can still be used for imaging purposes. For example, light from the illumination column is transmitted through the dichroic mirror and can reach the sample or the sample plane is still projected on the CCD by the objective and tube lens, allowing observation and recording of the experiments.

The telescope formed by lenses L1 and L2 should be designed to meet the following requirements:

(1) The SLM is imaged onto the exit pupil of the microscope objective [6, 8] to prevent vignetting of high-frequency Fourier components, which get diffracted at larger angles.
(2) To make use of its whole active area, the image of the modulator should be scaled down to match the size of the objective's back aperture. Furthermore, an overfilling of the SLM by the laser will result in an overfilling of the aperture. This, which is necessary, can be accomplished with the first telescope (inverted) formed by lenses LE and LC. The ratio should be adjusted to optimize trapping efficiency as in non-holographic set-ups [19, 20]. Gaussian laser beams are typically expanded so that the beam waist roughly matches the aperture (here, the size of the SLM).
(3) Finally, it must provide parallel illumination to the infinity-corrected objective (figure 1), hence the telescopic arrangement. Most modern microscope objectives are corrected to work with the sample at the front focal plane. Light rays are therefore parallel after the objective, which is advantageous, since additional optics, such as fluorescence filters or polarizers, can be placed in the path of those parallel rays with negligible effects on focus or aberration correction [21]. An important consequence is that infinity-corrected microscopes need no lenses in the epifluorescence path to collimate light, and thus the two lenses of the telescope can be chosen and placed with total freedom, unlike older microscopes with fixed tube length [18].

Also, regarding the optical system, since the spatial light modulator is illuminated by collimated light and the diffracted beams are observed at the focal plane of the objective lens (focal length, $f$), the relation between the complex reflectance, $R(u, v)$, of the modulator and the electric field at the sample plane, $E(x, y)$, is, except for some often irrelevant phase terms [22], that of a Fourier transform:

$$E(x, y) = e^{i\psi(x,y)} \int\int R(u, v) \times \exp\left[-i\frac{2\pi}{\lambda f}(ux + vy)\right] du\, dv. \quad (1)$$

In light of these requirements for the telescope, distance $d_1$ from the SLM to the first lens L1 and distance $d_2$ from the second lens L2 to the objective exit pupil (figure 2) are subject to several constraints. The distance between these two lenses must be the addition of their focal lengths, $d = f_1 + f_2$, for them to form a telescope. Furthermore, the SLM is imaged by this system with an absolute lateral magnification given by:

$$M = \left|\frac{y'}{y}\right| = \frac{f_2}{f_1}. \quad (2)$$

Incidentally, this magnification is independent of distances $d_1$ and $d_2$, since a ray that leaves the edge of the SLM and travels parallel to the optical axis will always exit the system at the same height (see figure 2). Total distance, $L$, from the SLM to the objective back aperture is therefore

$$L = d_1 + d_2 + f_1 + f_2 = d_1(1 - M^2) + f_1(1 + M)^2, \quad (3)$$

where equation (2) was considered and distance $d_2$ was calculated by use of the Gaussian lens formula:

$$d_2 = -d_1 M^2 + f_1 M(1 + M). \quad (4)$$

The 4-$f$ configuration is a common arrangement for the imaging telescope. The SLM is placed at the front focal plane

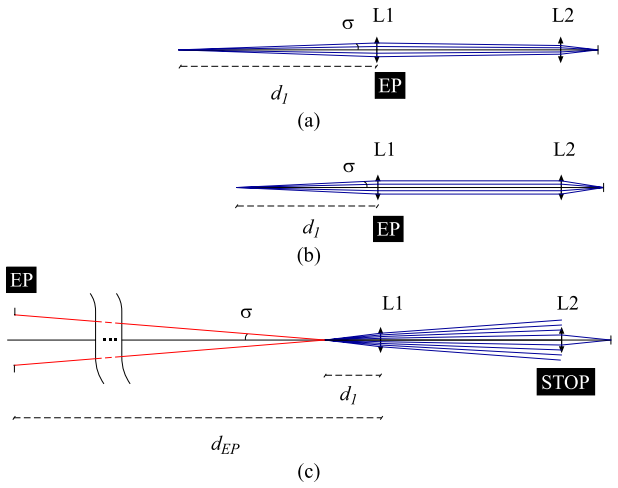


**Figure 3.** Ray tracing showing the different positions of the SLM with respect to lens L1: (a) $d_1 > f_1$, (b) $d_1 = f_1$ and (c) $d_1 < f_1$. EP, entrance pupil.

of the first lens ($d_1 = f_1$) so that the image is formed at the back focal plane of the second lens ($d_2 = f_2$), as shown in figure 3(b). Light rays are parallel between the two lenses and the total length becomes $L = 2f_1(1 + M)$. However, this is not the only possibility; figures 3(a) and (c) show ray tracings for two alternative arrangements in which the SLM is placed further away from and closer to lens L1, respectively.

Interestingly, more compact set-ups can be built in this latter case. For a given focal length $f_1$, as magnification $M$ does not depend on SLM position, the shortest overall length $L$ is achieved when the SLM is placed as close to the first lens as possible (minimum $d_1$, equation (3)). The variation of $L$ with $d_1$ for a practical example corresponding to the analysis in section 2.2 ($M = 0.3$, $f_1 = 250$ mm), is depicted in figure 4(a). It can be seen that $L$ approaches its minimum value of $L = f_1(1 + M)^2 \approx 420$ mm as the modulator gets closer to lens L1 ($d_1$ tends to zero).

The price for this smaller footprint is lower light efficiency. Indeed, let us assume that the entrance pupil diameter, $\phi_2$, of lens L2 is smaller than or equal to that of lens L1, $\phi_1$, (that is, $\phi_2 \leqslant \phi_1$). This is normally the case in telescopes, as the diameter of a beam will get smaller at the output. We see that, whenever the SLM is placed at a distance $d_1 \geqslant f_1$ (cases (a) and (b)), lens L1 is both the aperture stop and the entrance pupil of the imaging system. Thus the distance from L1 to the entrance pupil is $d_{EP(a,b)} = 0$ and pupil diameter is $\phi_{EP(a,b)} = \phi_1$. However, when $d_1 < f_1$ (case (c)), L2 acts as the aperture stop of the system and the entrance pupil appears to the left of L1, at a distance

$$d_{EP(c)} = f_1 \frac{1 + M}{M}. \tag{5}$$

In this case the entrance pupil diameter is $\phi_{EP(c)} = \phi_2/M$. The system aperture $\sin\sigma$ is therefore:

$$\sin\sigma = \frac{\phi_{EP}/2}{\sqrt{(\phi_{EP}/2)^2 + (d_{EP} - d_1)^2}} \times \begin{cases} \sin\sigma_{(a,b)} = \dfrac{\phi_1/2}{\sqrt{(\phi_1/2)^2 + d_1^2}} \\ (d_1 \geqslant f_1) \\ \sin\sigma_{(c)} = \dfrac{\phi_2/M}{\sqrt{(\phi_2/2M)^2 + \left(f_1\frac{1+M}{M} - d_1\right)^2}} \\ (d_1 < f_1). \end{cases} \tag{6}$$

From equation (6) we can see that, for case (c), $\sin\sigma$ increases with $d_1$, whereas in cases (a) and (b) it decreases. Thus, in both situations the maximum value is attained for $d_1 = f_1$. When $\phi_1 = \phi_2$, we have:

$$\sin\sigma_{max}(d_1 = f_1) = \frac{\phi_1/2}{\sqrt{(\phi_1/2)^2 + f_1^2}}. \tag{7}$$

Figure 4(b) is a graphical representation of equation (6) for $M = 0.3$, $f_1 = 250$ mm and $\phi_1 = \phi_2 = 22.9$ mm. It shows that placement of the SLM at the front focal plane of lens L1 (the 4-$f$ configuration) maximizes light efficiency, although it is intermediate in terms of overall length. The modulator can be placed closer to lens L1 if a smaller optical system is desired. However, as we prefer to retain the light-gathering capacity and shorten the optical system by some other means, as discussed below, a 4-$f$ configuration is assumed for the telescope in what follows.

Let us now focus on the practical constraints for distances $d_1$ and $d_2$. When using an inverted commercial microscope,

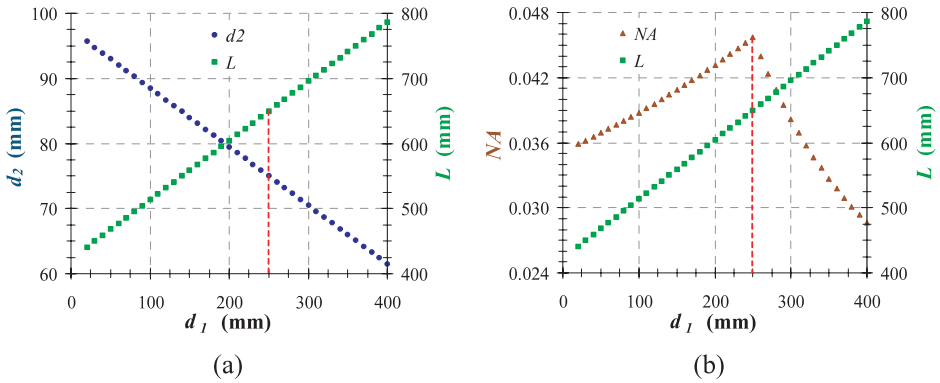


**Figure 4.** Numerical example ($M = 0.3$, $f_1 = 250$ mm, $\phi_1 = \phi_2 = 22.9$ mm) of the dependence of $d_2$, $L$ and numerical aperture, $\sin\sigma$, of the telescope with distance $d_1$. The dashed red line indicates the case $d_1 = f_1$.

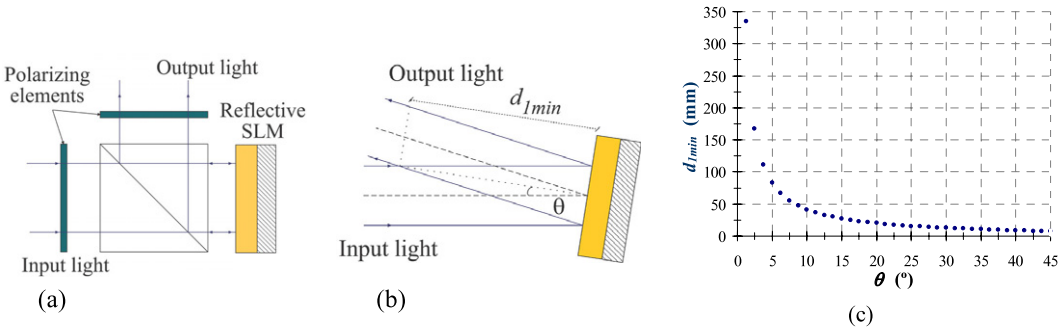


**Figure 5.** Geometry in a reflective SLM: (a) with a beamsplitter and (b) by tilting the SLM. (c) Dependence of the minimal distance $d_{1\,\mathrm{min}}$ on the incident angle $\theta$.

the minimum distance from lens L2 to the exit pupil of the objective, $d_2$, is some 300 mm, if the lens is placed outside the microscope (roughly the length of the fluorescence path). This limitation determines to a large extent the overall size and often leads to large optical systems: in effect, for $d_1 = f_1, d_2 = f_2$ (4-$f$ arrangement), equation (3) becomes:

$$L = 2(f_1 + f_2) = 2d_2\frac{1+M}{M}. \tag{8}$$

The active area of the spatial light modulators used in optical tweezers range from about 8 mm (BNS P512 [23]) to about 20 mm (Hamamatsu X8267 [24]) on a side. However, the exit pupil diameter of high-aperture, immersion objectives is between 3 and 5 mm. Thus, lateral magnification $M$ takes values between 0.1 and 0.6. For a typical value of $M = 0.4$ and with $d_2 = 300$ mm, $d_1$ becomes 750 mm and finally $L = 2.1$ m.

Such long working lengths help to minimize optical aberrations [2] and are thus frequently viewed as a desirable feature. However, our results indicate (section 4) that aberrations in the optical train are not really an issue and can be controlled quite easily by use of a few simple tricks. Thus, the distance $L$ could be much shortened if $d_2$ were reduced by placing lens L2 inside the microscope. Practical details on how to do this are left to the proposed solution in section 2.2.

Reduction in distance $d_2$ leads to reduction in distance $d_1$, as both are linked by equation (2). This latter distance is subject to design constraints of its own and frequently cannot be made smaller than a certain limit, which should be taken into account when reducing the design.

For example, minimal distance between SLM and lens L1, $d_1$, can be just a few centimetres for transmittance SLMs [3, 4], the space required to allow polarizing elements to fit between. However, reflective SLMs are more commonly used as they provide higher resolutions and a larger fill factor. They do pose different geometrical requirements. One possible arrangement would be to place the reflective modulator perpendicular to the optical axis [25] and then redirect the modulated beam out with a beamsplitter, as shown in figure 5(a). However, control of the input and output polarization is a much desired feature of the set-up, as it may allow free access to the different operating modes of the device (such as the phase-only modulation operating curve). Both constraints, polarization control and on-axis operation, can be met by the use of a non-polarizing beamsplitter, but the round-trip path through that element would result in a loss of 75% of incident light. This is unacceptable given the large power required for trapping even a small number of samples, so the device is usually operated at small incident angles $\theta$ (figure 5(b)) [26]. This sets the minimal distance at

$$d_{1\,\mathrm{min}} = \frac{\phi_{\mathrm{SLM}}}{2\tan\theta}, \tag{9}$$

the distance required for separating input and output beams.

Figure 5(c) shows distance $d_{1\,\mathrm{min}}$ as a function of $\theta$ for a medium size SLM, $\phi_{\mathrm{SLM}} \approx 14.6$ mm (Holoeye Photonics, LC-R 2500, see section 3). For small angles, $\theta \approx 2.5°$, minimum distance is $d_{1\,\mathrm{min}} \approx 170$ mm. Allowance for polarizing elements would add some centimetres to the total count. At any rate, in practice, this result appears to be less restrictive than limitations arising from the position of lens L2.

### 2.2. *Optical set-up: proposals and practical considerations*

According to the analysis of the optical system constraints carried out in the preceding section, we built a system of holographic optical tweezers as follows: a Nd:$YVO_4$ laser beam (Viasho Technology, $\lambda = 532$ nm, 120 mW) illuminates a twisted-nematic liquid-crystal reflective SLM (Holoeye Photonics, LC-R 2500), sandwiched between a polarizer and an analyser with the proper orientations to achieve phase-mostly modulation (see section 3). Light after the telescope enters a commercial inverted microscope. We show results for two different models, a Nikon Eclipse TE-2000E and a Motic AE-31, equipped with oil-immersion, high-numerical aperture objectives (Nikon Plan Fluor 100×, 1.30 NA and Motic Plan achromatic 100×, 1.25 NA, respectively).

Distance $d_2$ from lens L2 to the objective exit pupil is greatly reduced by placing the lens inside the microscope body. This is straightforward for the TE-2000 microscope, as a lens can be easily retrofitted into standard Nikon fluorescence cubes. Each cube has a 1″ threaded circular aperture on one of its six surfaces, for the excitation filter to be mounted. However, lenses or any other optical or mechanical component can be attached there instead. Figure 6(a) shows a photograph of a cube with the dichroic mirror inside and lens L2 on the input face, directly screwed into place. Although not visible, an absorbance filter is also present on the bottom side (exit) to filter the laser out, thus preventing camera saturation.

However, custom-made modification was necessary for the Motic AE-31 cube, an inexpensive inverted microscope

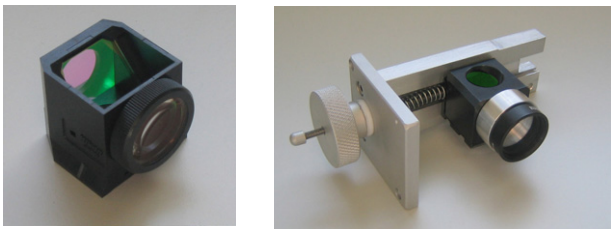

(a) (b)

**Figure 6.** Detailed photographs of (a) a standard commercial cube for a Nikon Eclipse TE-2000E microscope and (b) a custom-made cube for a Motic AE-31 microscope.

with fluorescence capacity. A centring mechanical component containing the cube is shown in figure 6(b).

By adopting this solution, distance $d_2$ goes down to about 75 mm for the Nikon microscope and to 100 mm for the Motic instrument. If the vertical size of the Holoeye modulator (see specifications in section 3) is imaged by the telescope to match the objective exit pupil (diameter of about 4 mm, Nikon Plan Fluor 100×), the magnification would then be $M = 4/14.5$. If we place the SLM on the front focal plane of lens L1 then $d_1 \approx 275$ mm (corresponding to $d_2 = 75$ mm), the total length between the SLM and the microscope objective becomes $L \approx 0.7$ m. This is much shorter than the 2.1 m we obtained in section 2.1, especially as part of the path is inside the microscope. Conveniently, the distance between lenses L1 and L2, which is about $75 + 275$ mm $= 350$ mm, is large enough to enable lens L1 to be placed outside the microscope. Similar conclusions can be drawn for $d_2 = 100$ mm (Motic microscope).

Finally, the required tilt $\theta$ of the SLM ($\phi_{\mathrm{SLM}} \approx 15$ mm) with respect to the incident beam (figure 3(b)), such that it can be put as close to lens L1 as $d_1 \approx 275$ mm, is only about a few degrees, according to equation (9). Nevertheless, we place the SLM tilted 45°, because it simplifies the arrangement of the whole optical set-up. We found that, although not lying on a plane perpendicular to the optical axis, the SLM is capable of producing fairly good traps when functioning in a suitable phase-only configuration. These issues are analysed in detail in section 3.

Figure 7 shows pictures of the optical set-ups built for the Nikon Eclipse TE-2000E (figure 7(a)) and for the Motic AE-31 (figure 7(b)) microscopes. We see the expander lens LE, collimating lens LC and some polarizing elements before and after the SLM, which is arranged to reflect light at right angles. Placing the SLM at 45° considerably simplifies the optical set-up, as it works geometrically as a mirror. Both lenses L1 are outside the microscope bodies and lenses L2, mounted on their respective cubes, cannot be seen.

## 3. Holoeye LC-R 2500 spatial light modulator

The Holoeye LC-R 2500 used in our set-ups is a reflective, twisted nematic, liquid crystal on silicon (LCOS) spatial light modulator (SLM), and was selected for its high resolution, good optical quality and low cost. It has an active area of $19.5 \times 14.6$ mm$^2$, divided into $1024 \times 768$ square pixels (pixel pitch $=$ 19 $\mu$m, fill factor 93%) that are electrically addressed by an 8-bit signal coming from a computer graphics card through the DVI interface [27]. The SLM can provide from 0 to $2\pi$ phase modulation in the visible region (400–700 nm), although usually with a certain amount of amplitude modulation, which is inherent to twisted nematic liquid crystal modulators [28]. The response depends on the polarization state of the light both before and after the SLM and can be changed by adjusting the polarization elements shown in figure 7. Since we are not using the device at the near-normal incidence assumed by the manufacturer [26], modulation response was measured and adjusted.

In section 3.1 we give details on these measurements and report a configuration for which there is nearly uniform amplitude modulation and a maximum phase shift of $2\pi$ (phase-mostly configuration), when the device makes an angle of 45° with the incident light. Also, in section 3.2 we analyse the effect of oblique incidence on the reconstruction

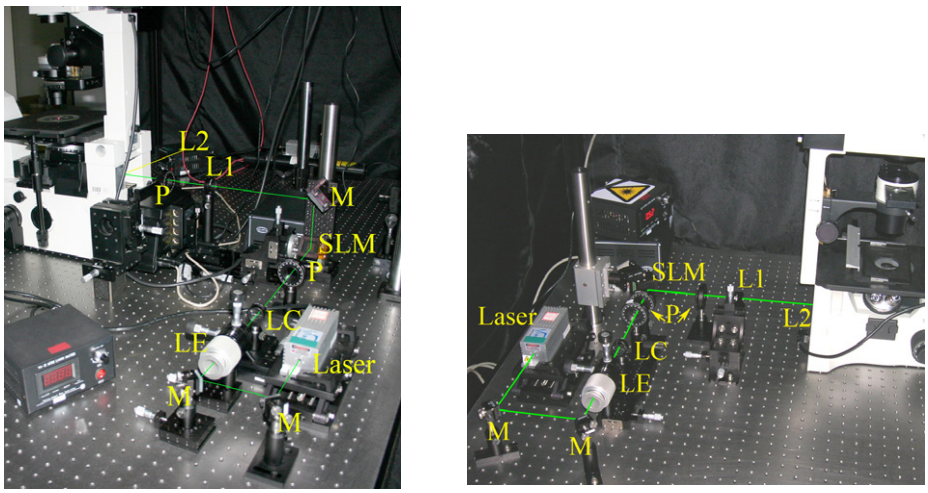


(a) (b)

**Figure 7.** Photographs of two holographic optical set-ups with microscopes (a) Nikon Eclipse TE-2000E, (b) Motic AE-31. (M: mirror, P: polarizing element.)

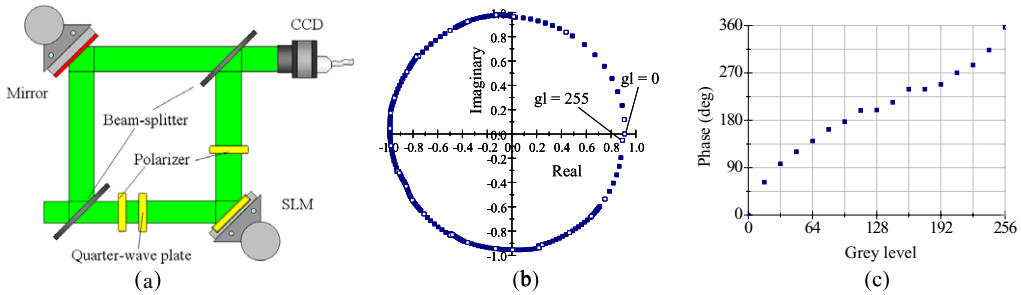


**Figure 8.** (a) Mach–Zehnder interferometer for SLM phase determination. Holoeye LC-R 2500 phase-mostly configuration at 45° (b) representation in the complex plane and (c) phase as a function of the grey level (gl).

of holograms. Finally, section 3.3 is devoted to the correction of certain aberrations of the display caused by the curvature of the silicon backplane.

### *3.1. Characterization: phase-only configuration*

Spatial light modulators are electro-optic devices that can modify (modulate) the amplitude and phase of an optical wavefront on a controlled basis. Spatial light modulators come in many flavours [29], the most frequently employed for holography being those based on liquid crystal mixtures. Modulation is achieved by making light propagate inside an optically active medium (the liquid crystal), whose optical properties, notably extraordinary index of refraction or optical axis, are voltage-dependent. Thus, the retardance induced by such a device is, in turn, dependent on the voltage applied to the liquid crystal cell, as well as on the polarization of the traversing light beam.

Spatial light modulator characterization consists of determining the amplitude and phase modulation values for the different addressing voltages, for a fixed orientation of both input and output polarization elements. For an 8-bit modulator, up to 256 different voltage values can be applied to any given pixel. Usually, SLM electronics is connected to the graphics board of a computer and the user feeds the SLM by displaying images on the PC screen. The different grey levels ($gl$) of the image (ranging between $gl = 0$ and 255) are eventually translated into driving voltages inside the modulator.

For each grey level, amplitude modulation is simply measured as the square root of the transmittance of the device. Phase modulation is the phase change imparted by the modulator onto the incoming wavefront. Since only phase differences are of any physical significance, it is obtained by measuring the relative phase shift between a reference grey level (phase modulation arbitrarily set to zero) and the other grey-level values.

Figure 8(a) shows a sketch of the Mach–Zehnder interferometer that we used to measure the phase shifts: a collimated laser beam ($\lambda = 532$ nm) is divided by the first beamsplitter and a CCD camera records the interference fringes between the two plane waves. The orientations of the quarter-wave plate and the two polarizers determine the modulation properties of the SLM, which is placed in one arm of the interferometer. The phase it introduces is observed as a fringe displacement on the interference plane. When a constant reference grey level is displayed on one half of the modulator and the remaining values are sequentially displayed on the other half, shifted interference fringes can be seen on the CCD image. The relative phase shift $\varphi$ can be accurately measured with the fringe analysis method described in [30] as

$$\varphi = 2\pi\,\Delta/P, \tag{10}$$

where $P$ is the period of the fringes and $\Delta$ is the relative fringe displacement. The former is determined by Fourier transforming the fringe images, while the latter is obtained by performing the one-dimensional correlation product between the shifted fringe patterns. This gives a measurement of the similarity between the two functions as one of them is displaced over the other. The position of the correlation maximum corresponds to the maximum overlapping conditions and, in the case of fringe correlation, it directly provides the fringe displacement.

Finally, the set-up in figure 8(a) also allows transmittance measurements, by placing an intensity detector before and after the SLM for each displayed grey-level value; amplitude modulation is simply the square root of the transmittance, and is usually normalized to 1.

The best phase-mostly operating curve we found is shown in figure 8(b). The graph is a polar plot where the amplitude and phase modulation are jointly displayed as a complex-plane curve, each point standing for a single grey level (from $gl = 0$ to 255). The magnitude of a vector from the origin of coordinates to the point considered (i.e. the radial coordinate) gives the amplitude modulation and the angle with respect to the real-positive axis (the polar angle) is the phase shift. The measurement was done for 16 evenly spaced grey-level values, represented by empty squares in the curves. The remaining points (solid squares) are obtained by linear interpolation. This configuration is achieved when the modulator is sandwiched between two linear polarizers, oriented at $-45°$ and 26° with respect to the longest side of the display. Positive angles are measured counterclockwise, when looking at the polarizer by the side first touched by the laser. Maximum phase shift reaches $1.98\pi$, amplitude is almost constant with an intensity contrast of only 1:1.25 and optical efficiency is around 50%. Finally, figure 8(c) shows the phase modulation as a function of the grey level (addressing voltage), which is not uniform and should be linearized when the holograms are computed.

### *3.2. Reconstruction of holograms by a tilted modulator*

As explained above, we place the modulator at 45° with respect to the beam direction. Here, we analyse how this may change

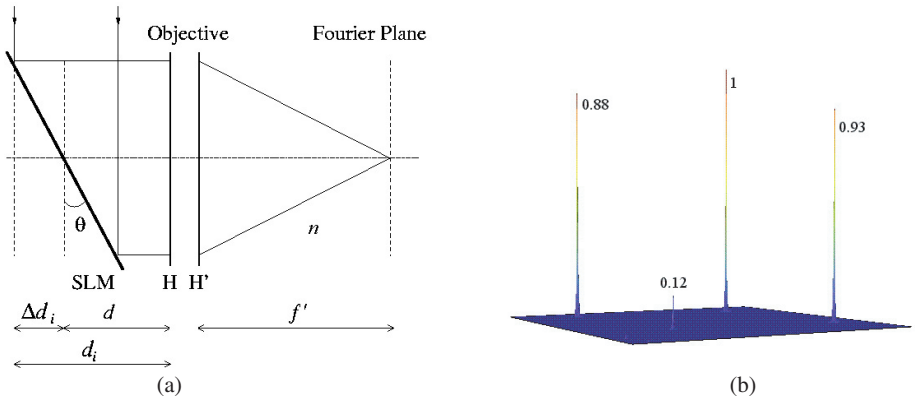


**Figure 9.** (a) SLM titled by an angle $\theta$ with respect to the beam direction ($n$: index of refraction). (b) Simulation of the diffraction effects arising from equation (14) ($\theta = 45°$) on three equal intensity traps.

the reconstruction of the displayed hologram $R(u, v)$, and affect the performance of the optical traps.

The hologram $R(u, v)$ is calculated by means of equation (1). Usually, the spatially variant phase term $e^{i\psi(x,y)}$ is not taken into account as it disappears when the intensity of the diffracted light is recorded. Our goal in this section is to study how the hologram is reconstructed when the modulator is tilted, which means that the distance between each SLM row and the objective changes (figure 9(a)). As $e^{i\psi(x,y)}$ explicitly depends on the distance between the hologram and the front principal plane of the objective, we need to include this phase in the analysis. The complete formula that links a hologram $R(u, v)$ with the reconstructed field $E(x, y)$ [22] is:

$$E(x, y) = \exp\left(\frac{ik}{2f'}\left(1 - \frac{d}{f'}\right)(x^2 + y^2)\right) \times FT_{\lambda f'}[R(u, v)], \tag{11}$$

where $d$ is the distance between the SLM and the front principal plane of the objective, $f'$ is the effective focal length ($f' = f/n$, where $n$ is the index of refraction) and $FT_{\lambda f'}[R(u, v)]$ stands for the Fourier transform of $R(u, v)$ evaluated at frequencies $x/\lambda f'$ and $y/\lambda f'$. Notice that $|E(x, y)|^2 = |FT_{\lambda f'}[R(u, v)]|^2$.

The modulator is tilted in such a way that the distance $d_i$ between the $i$th modulator row and the front principal plane $H$ is constant, but varies from row to row. Thus, $d_i = d + \Delta d_i$. Then, the contribution of the $i$th row $R(u, v_i)$ to the total electric field is:

$$E_i(x, y) = \exp\left(\frac{ik}{2f'}\left(1 - \frac{d_i}{f'}\right)(x^2 + y^2)\right) \times FT_{\lambda f'}[R(u, v_i)], \tag{12}$$

where $FT_{\lambda f'}[R(u, v_i)]$ is the two-dimensional Fourier transform of row $R(u, v_i)$. Therefore, the proper expression for the reconstructed field can be written by addition of terms similar to that in equation (12), for different distances $d_i$:

$$E = \exp\left(\frac{ik}{2f'}\left(1 - \frac{d}{f'}\right)(x^2 + y^2)\right) \times \sum_i \exp\left(-\frac{ik}{2f'}\frac{\Delta d_i}{f'}(x^2 + y^2)\right) FT_{\lambda f'}[R(u, v_i)]. \tag{13}$$

Finally, the intensity is

$$I \propto EE^* = \left|\sum_i \exp\left(-\frac{ik}{2f'}\frac{\Delta d_i}{f'}(x^2 + y^2)\right) \times FT_{\lambda f'}[R(u, v_i)]\right|^2. \tag{14}$$

Notice that this result is independent of distance $d$. An example simulated using this equation is shown in figure 9(b). A hologram was computed by using the Gerchberg–Saxton algorithm [31, 32] to obtain three equal intensity traps. The simulation realistically takes into account both the actual phase-mostly modulation curve and the geometrical parameters of the SLM. The figure shows a typical result: as a consequence of the SLM tilt, the intensity of the three traps is no longer uniform (a small replica is also visible). These differences are hardly noticeable experimentally and can be corrected during hologram computation if desired. Our conclusion is that use of the SLM at large angles to the optical axis does not seem to pose any major difficulty and may simplify the optical layout. A different but related study that supports similar conclusions can be found in [33].

### *3.3. Modulator aberrations and correction*

A liquid crystal on silicon (LCOS) micro-display essentially consists of a liquid crystal layer between a cover glass and a silicon backplane that contains the driving circuitry and is coated with aluminium to form a highly reflective surface. The backplane is manufactured at commercial VLSI foundries using standard CMOS methods and processes, which unfortunately are not optimized with optical performance in mind. As a consequence, although the resulting devices can be made flat at the pixel level to prevent scattering and improve diffraction efficiency, they have bows and warps at the die level [34], which frequently gives rise to major optical aberrations.

In particular, the beam reflected by our Holoeye modulator, when focused by the microscope objective, forms two light lines instead of a diffraction-limited spot. The two lines are perpendicular to each other and appear at two different focal planes in a behaviour similar to the presence of astigmatism (refer to figure 10). Figure 10(b) (left and right)

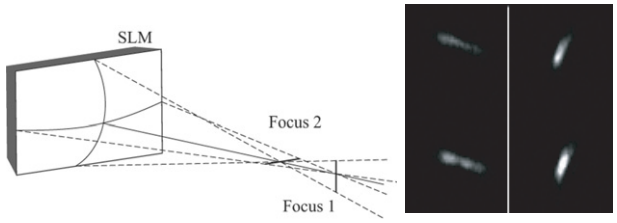


(a) (b)

**Figure 10.** (a) Light reflected by the SLM converging at two different foci. (b) Intensity of a pair of optical traps at the two foci.

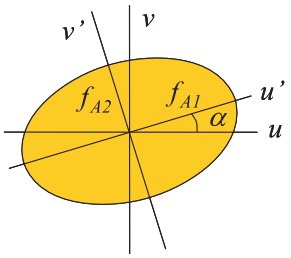


**Figure 11.** Definition of the parameters used to correct SLM aberration.

corresponds to the images captured at the two foci when a pair of optical traps is generated. The effect, which also takes place at normal incidence, reveals the lack of flatness of the device surface and seems to be a widespread problem [35].

Fortunately, in our case it was relatively easy to find an anamorphic phase function that reverses the effect and which can then be added to any trapping hologram, eventually correcting the aberration. The correction is modelled after the following phase function, $\phi_{ab}$:

$$\phi_{ab} = -\frac{\pi}{\lambda}\left[\left(\frac{u'}{f_{A1}}\right)^2 + \left(\frac{v'}{f_{A2}}\right)^2\right], \tag{15}$$

which is the quadratic approximation of an elliptical wave having focal lengths $f_{A1}$ and $f_{A2}$ in the $u'$ and $v'$ directions, respectively [22]. Here, $u'$ and $v'$ are the $\alpha$-rotated axes of $u$ and $v$ (the modulator horizontal and vertical coordinates, figure 11):

$$\begin{aligned} u' &= u\cos\alpha + v\sin\alpha \\ v' &= v\cos\alpha - u\sin\alpha. \end{aligned} \tag{16}$$

We found experimentally by trial and error parameters $f_{A1}$, $f_{A2}$ and $\alpha$ which satisfactorily correct the aberration. We display the corresponding phase function $\phi_{ab}$ on the SLM and observe the quality of the optical trap: initial values for $f_{A1}$ and $f_{A2}$ are determined by finding the two foci in figure 10(a), then different phases are computed with various $\alpha$ orientations (while allowing slight changes in $f_{A1}$ and $f_{A2}$) until a trap with circular symmetry is obtained. We finally found $f_{A1} = 30$ m, $f_{A2} = 8$ m and $\alpha = 17°$, for our modulator. The resulting phase correction, adapted to the SLM operating curve (figures 8(b) and (c)), is shown in figure 12(a). Figure 12(b) shows the captured images of the two traps at the mid-point of the two foci (left) and the spots after correction (right). A more quantitative approach to characterizing and

(a) (b)

**Figure 12.** (a) Elliptical phase that corrects the aberration of Holoeye modulator. (b) Image of two optical traps without correction (left) and after correction (right).

correcting SLM aberrations can be found in [35]. A final possibility for determining phase correction would be to use a Shack–Hartmann wavefront sensor, as this allows accurate and automated measurements of the wave aberration.

## 4. Aberrations in the optical train

Single-beam optical tweezers rely on the gradient component of the light force to trap and move material particles. As light has to be brought to a sharp focus, exquisitely corrected microscope objectives are required to form the optical traps. Optical aberrations are always a major cause of concern, since their detrimental effect on trap stiffness is well documented [36]. Because of this, an accurate analysis of aberrations of the complete optical system should be included in the design process as a final stage.

In this section, we perform ray-tracing simulations with commercial optical design software (Zemax) to study the spherical aberration in the focal plane of the microscope objective, for different qualities and combinations of outside lenses. The microscope objective is considered a paraxial lens to isolate the influence of the other lenses on the quality of the focal spot. This approach may provide useful rules of thumb for the design of the external set-up but it should be noted that important aberrations may be left out of the analysis. For example, when using oil-immersion lenses, the index mismatch at the glass/water interface is known to be a major source of spherical aberration [37].

As our objectives are infinity-corrected, spherical aberration is minimized at the front focal plane. The focal length in air, $f$, can be obtained from the magnification, $m$, and the focal length of the microscope tube lens, $f_{\text{tube}}$, $f = f_{\text{tube}}/m$ [21]. Nikon and Motic objective focal lengths are 2 mm and 1.2 mm, respectively.

This section is organized as follows: first, in section 4.1 a perfectly parallel beam is supposed to illuminate lens L1 to isolate the effect of the imaging telescope formed by lenses L1 and L2. In section 4.2, the best solution found in section 4.1 is analysed jointly with the beam expander and collimator. Whenever possible, we use commercial standard single lenses. Unless otherwise specified, these are made of BK7, which has good transmission throughout the visible and the near-infrared spectra (over 90%). Also, in practice, antireflection coatings should be used to help reduce transmission losses and stray reflections.

Aberrations introduced by the SLM are not taken into account, as they have presumably been corrected with the

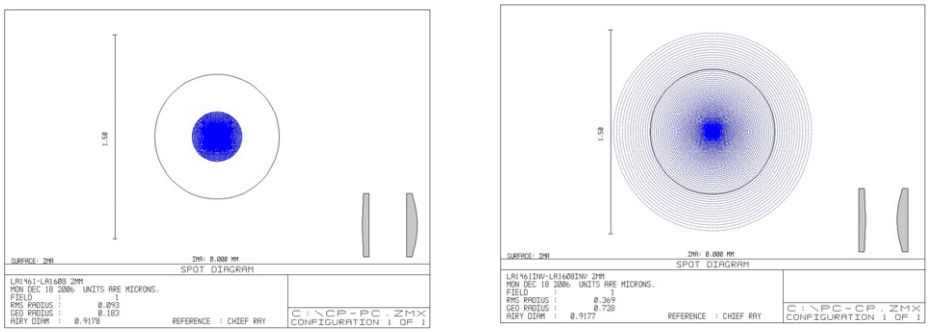


(a) (b)

**Figure 13.** Spot diagrams for the following shapes and orientation of lenses L1 and L2: (a) plano-convex, curved surfaces facing collimated beams; (b) plano-convex, flat surfaces facing collimated beams.

method developed in section 3.3. However, we do consider that the modulator is tilted by 45° in the horizontal (long) direction and that the illuminated area of the device, as well as the active area imaged onto the exit pupil of the objective, has an elliptical shape.

### *4.1. Imaging telescope (L1 and L2)*

Again, we assume a 4-$f$ configuration for the telescope (section 2) and we analyse the set-up for the Nikon microscope, which needs shorter focal lengths than the Motic and is therefore more prone to aberrations. Required lens L2 focal length is $f_2 = d_2 = 75$ mm and lens L1 focal length is chosen as $f_1 = 250$ mm ($M = 0.3$). This is a standard value in many vendor's catalogues, making it an easy lens to find commercially and one which fully meets magnification requirements: for an exit pupil diameter of 4 mm (Nikon Plan Fluor 100× objective), the SLM active area imaged onto the objective exit pupil is elliptical, with its vertical and horizontal axis of about 700 and 1000 pixels, respectively. The total length given by equation (8) is, in this case, $L = 650$ mm.

We chose plano-convex lenses, since these are the best singlet form for either focusing collimated light or for collimating a point source. Thus, placing two plano-convex lenses with their flat surfaces facing one another is the best simple solution of spherical aberration for a telescope [38]. Figure 13(a) shows the spot diagram obtained in the focal plane of the microscope objective with this configuration. The results are worse if the same plano-convex lenses are used but with a wrong orientation (curved surfaces facing one another, figure 13(b)) or for two bi-convex lenses (results not shown). Inexpensive standard Thorlabs 1″ BK7 singlet lenses are used in our simulations: LA1461 (250 mm plano-convex), LA1608 (75 mm plano-convex), LB1056 (250 mm bi-convex) and LB1901 (75 mm bi-convex).

The RMS radius (root-mean-square radial size) indicated on the plots gives an approximate idea of the spread of the ray bundle. Roughly speaking, if all rays are well within the Airy disc (represented in the figures by a circle), the system is often considered to be diffraction-limited.

The results show that two plano-convex lenses with their curved surfaces facing the collimated beams (figure 13(a)) produce a diffraction-limited spot (RMS radius = 0.093 $\mu$m, Airy radius = 0.46 $\mu$m), whereas in the opposite case, shown in figure 13(b), they do not (RMS radius = 0.369 $\mu$m). Also, if the telescope is made with two bi-convex lenses, the result is intermediate (RMS radius = 0.137 $\mu$m).

In conclusion, simple plano-convex lenses are a good enough choice for the imaging telescope. There is no need for more sophisticated optics, even in systems like the one we are analysing that reduce dimensions by use of lenses with short focal lengths (such as $f_1 = 250$ mm, $f_2 = 75$ mm).

### *4.2. Beam expander and collimator (LE and LC)*

As mentioned in section 2.1, the laser beam expander and collimator also form a telescope, although used in reverse. It will increase the beam diameter of an incident Gaussian beam by

$$\tilde{M} = \frac{f_C}{f_E} \tag{17}$$

while simultaneously reducing the beam angular divergence by the inverse factor $1/\tilde{M}$. We chose for our simulations $f_E = 8$ mm, $f_C = 100$ mm so that a laser beam diameter of about 1.1 mm (like ours) is magnified 12.5 times. The beam then illuminates some 720 vertical pixels of the Holoeye modulator, fully consistent with the imaged active area we set in section 4.1 and overfilling requirements.

We assume that lens LE is a paraxial lens and we focus our analysis on collimating lens LC alone. This is because LE is either not necessary, when a fibre laser is used, or is a well-corrected microscope objective, when light is expanded by a spatial filter. In any case, the collimator receives a high-quality Gaussian beam that we assume is free from aberrations.

Figure 14(a) shows the results for an inexpensive plano-convex singlet (Thorlabs LA1509, 1″, BK7, 100 mm) with the right orientation. Under these conditions, the spot is not diffraction-limited (RMS radius = 1.208 $\mu$m, Airy radius = 0.46 $\mu$m), which is not surprising. For example, when compared to lens L2, even though its focal length is somewhat larger ($f_C = 100$ mm, $f_2 = 75$ mm), it works at a higher aperture (related by magnification $M$). Lens LC is the most critical element in the system with regard to aberrations and needs higher-quality optics.

We tried an achromatic doublet corrected in the visible region: 1″ Thorlabs' lens made of BK7 and SF5 (item number AC-254-100-A1). The result, plotted in figure 14(b) (RMS radius = 0.244 $\mu$m), shows that spherical aberration is

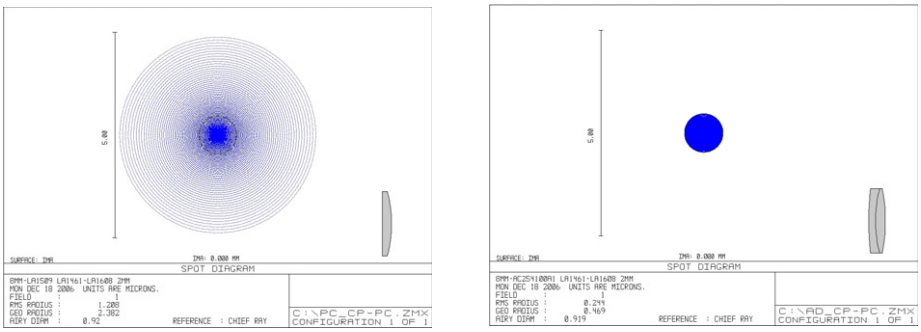


(a) (b)

**Figure 14.** Spot diagrams when the following shape of lens LC is used: (a) plano-convex, (b) achromatic doublet.

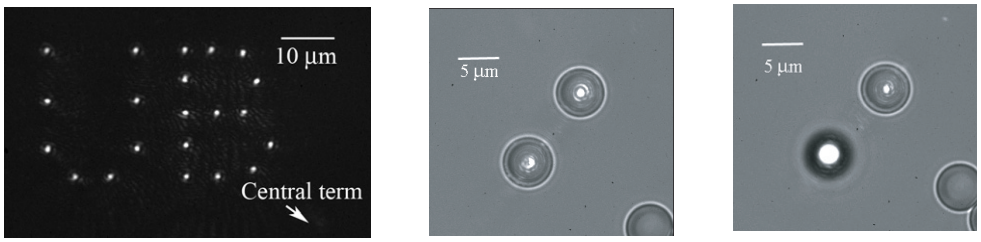


(a) (b) (c)

**Figure 15.** Experimental results with the Nikon microscope. (a) Several holographic optical traps, (b) polystyrene microspheres ($d = 5\ \mu$m) trapped at the same plane or (c) at different depths.

substantially reduced and that the spot can now be considered diffraction-limited.

In conclusion, special care should be taken when selecting lens LC. Because of its working conditions, it is especially prone to spherical aberration, and so a corrected lens, such as a doublet or an aspheric one, needs to be used.

## 5. Results and final remarks

Figure 15 is illustrative of the characteristic results that may be obtained with the system. Many quality traps showing diffraction rings can be simultaneously produced. Importantly, the central spot is very small (see figure 15(a)), which we believe is indicative of a well-controlled spatial light modulator. A large DC term creates an unwanted trap at the centre of the sample and may need to be filtered out. A deficient phase-only curve or failure to correct the nonlinearities between driving voltages and phase values (figure 8(c)) in computing the holograms contributes to this central spot. Light reflected at the front face of the SLM or unmodulated because of fill factor issues are also small contributions that cannot be eliminated.

Finally, figures 15(b) and (c) show polystyrene microspheres trapped and moved independently in three dimensions.

## Acknowledgments

This research was funded by the Spanish Ministry of Education and Science through grants FIS2004-03450 and NAN2004-09348-C04-03. We are indebted to S Vallmitjana for his general help and advice on several experimental issues.

## References

[1] Dufresne E R and Grier D G 1998 Optical tweezer arrays and optical substrates created with diffractive optical elements *Rev. Sci. Instrum.* **69** 1974–7

[2] Dufresne E R, Spalding G C, Dearing M T, Sheets S A and Grier D G 2001 Computer generated holographic optical tweezer arrays *Rev. Sci. Instrum.* **72** 1810–6

[3] Hayasaki Y, Itoh M, Yatagai T and Nishida N 1999 Nonmechanical optical manipulation of microparticle using spatial light modulator *Opt. Rev.* **6** 24–7

[4] Reicherter M, Haist T, Wagemann E and Tiziani H 1999 Optical particle trapping with computer-generated holograms written on a liquid-crystal display *Opt. Lett.* **24** 608–10

[5] Liesener J, Reicherter M, Haist T and Tiziani H J 2000 Multi-functional optical tweezers using computer-generated holograms *Opt. Commun.* **185** 77–82

[6] Curtis J E, Koss B A and Grier D G 2002 Dynamic holographic optical tweezers *Opt. Commun.* **207** 69–175

[7] Visscher K, Gross S P and Block S M 1996 Construction of multiple-beam optical traps with nanometer-resolution position sensing *IEEE J. Sel. Top. Quantum Electron.* **2** 1066–76

[8] Grier D G 2003 A revolution in optical manipulation *Nature* **424** 810–6

[9] Dholakia K and Reece P 2006 Optical micromanipulation takes hold *Nanotoday* **1** 18–27

[10] Di Leonardo R, Leach J, Mushfique H, Cooper J M, Ruocco G and Padgett M J 2006 Multipoint holographic optical velocimetry in microfluidic systems *Phys. Rev. Lett.* **96** 134502

[11] Burnham D R and McGloin D 2006 Holographic optical trapping of aerosol droplets *Opt. Express* **14** 4175–81

[12] Plewa J, Tanner E, Mueth D M and Grier D G 2004 Processing carbon nanotubes with holographic optical tweezers *Opt. Express* **12** 1978–81

[13] Creely C M, Volpe G, Singh G P, Soler M and Petrov D V 2005 Raman imaging of floating cells *Opt. Express* **13** 6105–10
[14] Neuman K C and Block S M 2004 Optical trapping *Rev. Sci. Instrum.* **75** 2787–809
[15] Grange W, Husale S, Güntherodt H and Hegner M 2002 Optical tweezers system measuring the change in light momentum flux *Rev. Sci. Instrum.* **73** 2308–16
[16] Block S M 1998 Constructing optical tweezers *Cell Biology: A Laboratory Manual* ed D Spector, R Goldman and L Leinward (Cold Spring Harbor, NY: Cold Spring Harbor Press)
[17] Berg-Sorensen K and Flyvbjerg H 2004 Power spectrum analysis for optical tweezers *Rev. Sci. Instrum.* **75** 594–612
[18] Fallman E and Axner O 1997 Design for fully steerable dual-trap optical tweezers *Appl. Opt.* **36** 2107–13
[19] Ashkin A 1992 Forces of a single-beam gradient laser trap on a dielectric sphere in the ray optics regime *Biophys. J.* **61** 569–82
[20] Fallman E and Axner O 2003 Influence of a glass-water interface on the on-axis trapping of micrometer-sized spherical objects by optical tweezers *Appl. Opt.* **42** 3915–26
[21] http://www.microscopyu.com/articles/optics/cfintro.html
[22] Goodman J W 1996 *Introduction to Fourier Optics* (New York: McGraw-Hill)
[23] http://www.bnonlinear.com/products/XYphase/data/XYPSLM0105.pdf
[24] http://sales.hamamatsu.com/assets/pdf/parts_X/X8077_X8267.pdf
[25] Hossack W, Theofanidou E, Crain J, Heggarty K and Birch M 2003 High-speed holographic optical tweezers using a ferroelectric liquid crystal microdisplay *Opt. Express* **11** 2053–9
[26] http://www.holoeye.com/download_daten/PhaseCam_Manual.pdf
[27] http://www.holoeye.com/download_daten/Spatial_Light_Modulator_LCHR_2500.pdf
[28] Lu K and Saleh B E A 1990 Theory and design of the liquid crystal TV as an optical spatial phase modulator *Opt. Eng.* **29** 240–6
[29] Efron U 1995 *Spatial Light Modulator Technology: Materials, Devices and Applications* (New York: Dekker)
[30] Martín-Badosa E, Carnicer A, Juvells I and Vallmitjana S 1997 Complex modulation characterization of liquid crystal devices by interferometric data correlation *Meas. Sci. Technol.* **8** 764–72
[31] Gerchberg R W and Saxton W O 1971 A practical algorithm for the determination of phase from image and diffraction plane pictures *Optik* **35** 237–46
[32] Di Leonardo R, Ianni F and Ruocco G 2007 Computer generation of optimal holograms for optical trap arrays *Opt. Express* **15** 1913–22
[33] Fukuchi N, Ye B, Igasaki Y, Yoshida N, Kobayashi Y and Hara T 2005 Oblique-incidence characteristics of a parallel-aligned nematic-liquid-crystal spatial light modulator *Opt. Rev.* **12** 372–7
[34] Seunarine K, Calton D W, Underwood I, Stevenson J T M, Gundlach A M and Begbie M 1999 Techniques to improve the flatness of reflective micro-optical arrays *Sensors Actuators* A **78** 18–27
[35] Wulff K D, Cole D G, Clark R L, Di Leonardo R, Leach J, Cooper J, Gibson G and Padgett M J 2006 Aberration correction in holographic optical tweezers *Opt. Express* **14** 4170–5
[36] Roichman Y, Waldron A, Gardel E and Grier D G 2006 Optical traps with geometric aberrations *Appl. Opt.* **45** 3425–9
[37] Vermeulen K C, Wuite G J L, Stienen G J M and Schmidt C F 2006 Optical trap stiffness in the presence and absence of spherical aberrations *Appl. Opt.* **45** 1812–9
[38] Smith W J 2000 *Modern Optical Engineering* (New York: McGraw-Hill)

# Appendix C

## Fast generation of holographic optical tweezers by random mask encoding of Fourier components

Published in

Optics Express
Vol.: 14, Issue: 6, Mar. 2006

# Fast generation of holographic optical tweezers by random mask encoding of Fourier components

**Mario Montes-Usategui, Encarnación Pleguezuelos, Jordi Andilla, and Estela Martín-Badosa**

*Grup de Recerca en Òptica Física, Departament de Física Aplicada i Òptica, Universitat de Barcelona, Martí i Franquès 1, Barcelona 08028, Spain*
*mario_montes@ub.edu*

*http://www.ub.edu/optics*

**Abstract:** The random mask encoding technique of multiplexing phase-only filters can be easily adapted to the generation of holographic optical tweezers. The result is a direct, non-iterative and extremely fast algorithm that can be used for computing arbitrary arrays of optical traps. Additional benefits include the possibility of modifying any existing hologram to quickly add more trapping sites and the inexistence of ghost traps or replicas.



**OCIS codes:** (090.2890) Holographic optical elements; (100.5090) Phase-only filters (kinoforms); (230.6120) Spatial light modulators; (999.9999) Optical tweezers.

## References and links

1. A. Ashkin, "Optical trapping and manipulation of neutral particles using lasers," Proc. Natl. Acad. Sci. USA **94**, 4853-4860 (1997).
2. M. J. Lang and S. M. Block, "Resource letter: LBOT-1: Laser-based optical tweezers," Am. J. Phys. **71**, 201-215 (2003).
3. K. C. Neuman and S. M. Block, "Optical trapping," Rev. Sci. Instrum. **75**, 2787-2809 (2004).
4. W. Grange, S. Husale, H. Güntherodt, and M. Hegner, "Optical tweezers system measuring the change in light momentum flux," Rev. Sci. Instrum. **73**, 2308-2316 (2002).
5. S. M. Block, "Constructing optical tweezers," in *Cell Biology: A Laboratory Manual*, D. Spector, R. Goldman, and L. Leinward, eds. (Cold Spring Harbor Press, Cold Spring Harbor, NY, 1998).
6. E. Fällman and O. Axner, "Design for fully steerable dual-trap optical tweezers," Appl. Opt. **36**, 2107-2113 (1997), http://www.opticsinfobase.org/abstract.cfm?URI=ao-36-10-2107
7. M. Reicherter, T. Haist, E. Wagemann, and H. Tiziani, "Optical particle trapping with computer-generated holograms written on a liquid-crystal display," Opt. Lett. **24**, 608-610 (1999), http://www.opticsinfobase.org/abstract.cfm?URI=ol-24-9-608
8. D. G. Grier, "A revolution in optical manipulation," Nature **424**, 810-816 (2003).
9. J. E. Curtis, B. A. Koss, and D. G. Grier, "Dynamic holographic optical tweezers," Opt. Commun. **207**, 169–175 (2002).
10. R. Tudela, E. Martín-Badosa, I. Labastida, S. Vallmitjana, I. Juvells, and A. Carnicer, "Full complex Fresnel holograms displayed on liquid crystal devices," J. Opt. A: Pure Appl. Opt. **5**, S189-S194 (2003).
11. K. Lu and B. E. A. Saleh, "Theory and design of the liquid crystal TV as an optical spatial phase modulator," Opt. Eng. **29**, 240-246 (1990).
12. E. Martín-Badosa, A. Carnicer, I. Juvells, and S. Vallmitjana, "Complex modulation characterization of liquid crystal devices by interferometric data correlation," Meas. Sci. Technol. **8**, 764-772 (1997).
13. L. Neto, D. Roberge, and Y. Sheng, "Programmable optical phase-mostly holograms with coupled-mode modulation liquid-crystal television," Appl. Opt. **34**, 1944- (1995), http://www.opticsinfobase.org/abstract.cfm?URI=ao-34-11-1944
14. N. Konforti, E. Marom, and S. Wu, "Phase-only modulation with twisted nematic liquid-crystal spatial light modulators," Opt. Lett. **13**, 251- (1996), http://www.opticsinfobase.org/abstract.cfm?URI=ol-13-3-251
15. G. Sinclair, J. Leach, P. Jordan, G. Gibson, E. Yao, Z. J. Laczik, M. J. Padgett, and J. Courtial, "Interactive application in holographic optical tweezers of a multi-plane Gerchberg-Saxton algorithm for three-dimensional

#10248 - $15.00 USD Received 10 January 2006; revised 2 March 2006; accepted 6 March 2006

light shaping," Opt. Express **12,** 1665-1670 (2004), http://www.opticsexpress.org/abstract.cfm?URI=OPEX-12-8-1665
16. M. Polin, K. Ladavac, S. Lee, Y. Roichman, and D. G. Grier, "Optimized holographic optical traps," Opt. Express **13,** 5831-5845 (2005), http://www.opticsexpress.org/abstract.cfm?URI=OPEX-13-15-5831
17. J. Curtis, C. Schmitz, and J. Spatz, "Symmetry dependence of holograms for optical trapping," Opt. Lett. **30**, 2086-2088 (2005), http://www.opticsinfobase.org/abstract.cfm?URI=ol-30-16-2086
18. K. Visscher, S. P. Gross, and S. M. Block "Construction of multiple-beam optical traps with nanometer-resolution position sensing," IEEE J. Sel. Top. Quantum Electron. **2**, 1066-1076 (1996).
19. R. Eriksen, P. Mogensen, and J. Glückstad, "Multiple-beam optical tweezers generated by the generalized phase-contrast method," Opt. Lett. **27**, 267-269 (2002), http://www.opticsinfobase.org/abstract.cfm?URI=ol-27-4-267
20. P. J. Rodrigo, V. R. Daria, and J. Glückstad, "Four-dimensional optical manipulation of colloidal particles," Appl. Phys. Lett. **86**, 074103 (2005).
21. J. Davis and D. Cottrell, "Random mask encoding of multiplexed phase-only and binary phase-only filters," Opt. Lett. **19**, 496- (1994), http://www.opticsinfobase.org/abstract.cfm?URI=ol-19-7-496
22. J. W. Goodman, *Introduction to Fourier Optics* (McGraw-Hill, 1996).

## 1. Introduction

Small dielectric objects can be trapped and moved using light alone. Part of the linear momentum carried by photons is transferred to microscopic samples when light gets reflected and refracted at their boundaries. Under the right conditions [1], the resulting balance of forces leads to stable confinement of the samples in a small region of space: the optical trap. Optical traps or tweezers are rapidly becoming an established technique for the manipulation of microscopic samples in several fields [2]. Accuracy, harmlessness and the possibility of calibration to measure the forces applied are salient features of the technique. There is also an excellent literature on how to build the required optical setups [3-6] and commercial systems are currently available from several vendors [3].

Typically, an optical tweezer setup consists of a high power laser and an inverted microscope modified with additional optics for beam shaping and steering [6]. A microscope objective with a high numerical aperture focuses the laser beam down to a diffraction-limited spot, creating the conditions for stable trapping.

A major improvement in optical tweezers has been brought about by the introduction of holograms displayed onto spatial light modulators (SLMs) [7-9]. With these in the setup, the laser wavefront can be spatially modified prior to the focusing step, resulting in a completely programmable intensity landscape over the sample plane. Large arrays of optical traps, position three-dimensional control or traps with exotic properties are among the new possibilities of holographic optical tweezers [8, 9].

Unfortunately, liquid crystal SLMs are notoriously unable to modulate the whole unit circle in complex space [10], that is, they are incapable of modifying both phase and amplitude of the incoming wavefront on an independent basis. They are constrained to modulate along one-dimensional manifolds through the complex plane, coupling phase and amplitude [11]. Most frequently the spatial light modulator is set to a phase-only configuration [12-14]. Although there is no control over the amplitude, the phase of the light beam can be changed at will.

The limited modulation capabilities of SLMs lead to problems in hologram generation that prevent holographic optical tweezers from reaching their full potential. Although, given a desired array of traps, the required hologram can be easily obtained by computing an inverse Fourier transform, the result is, in general, a full complex object that cannot be accommodated on the display. Algorithms have been developed that provide solutions by constraining the hologram to be a pure phase function but still generate usable traps, but they are time consuming. Computational load makes user interaction with the sample difficult in real time so there is a clear need for faster algorithms [15-17] and better displays.

There are alternatives but we believe these lack the simplicity and universality of the holographic approach. For example, acousto-optic scanners can produce arbitrary arrays of

#10248 - $15.00 USD Received 10 January 2006; revised 2 March 2006; accepted 6 March 2006

light spots at high speed [18], through time-sharing, but only in two dimensions. The generalized phase contrast method [19] allows an instant conversion of phase patterns into intensity patterns by optical means and is therefore extremely fast. However, it needs a specially fabricated phase plate and, probably, careful alignment. Also, its generalization to three dimensions seems rather elaborate [20].

The present paper introduces a new algorithm for producing holographic optical traps. It is based on the random mask encoding method [21] for multiplexing phase-only filters. The result is a very fast algorithm that gives the desired hologram with just a few simple computations. The algorithm can also be used to modify or multiplex any existing hologram very quickly and has an added advantage in that it does not produce the ghost traps or replicas that frequently plague other methods [16].

## 2. Experimental setup

Our experimental setup is sketched in Fig. 1. A continuous-wave, frequency-doubled Nd:$YVO_4$ laser beam (Viasho Technology, $\lambda$=532 nm, 1W) is expanded by a spatial filter, collimated by lens L1 and linearly polarized by a high quality polarizer. It illuminates a twisted-nematic liquid-crystal spatial light modulator (Holoeye Photonics, LC-R 2500) sandwiched between a half-wave plate and an analyzer with the proper orientations to achieve phase-only modulation [12-14]. Light then enters an inverted microscope (Motic AE-31) through the fluorescence port and is reflected upwards by a dichroic mirror to an oil-immersion, high numerical aperture, objective (Motic Plan achromatic 100x, 1.25 NA). Lenses L2 and L3, image the SLM onto the exit pupil of the microscope objective to prevent vignetting of high frequency Fourier components [8, 9]. They are arranged to form a telescope so as to still provide parallel illumination to the infinity-corrected objective. Finally, a CCD camera (Qimaging QICAM 1394) allows observation and recording of the experiments.

Since the spatial light modulator is illuminated by collimated light and the diffracted beams are observed at the focal plane of the objective lens (focal length, *f'*), the relation between the complex reflectance, *R(u,v)*, of the modulator and the electric field at the observation plane, *E(x,y)*, is, except for irrelevant phase terms [22], that of a Fourier transform:

$$E(x,y) = \iint R(u,v) e^{-i\frac{2\pi}{\lambda f'}(ux+vy)} du dv \,. \tag{1}$$

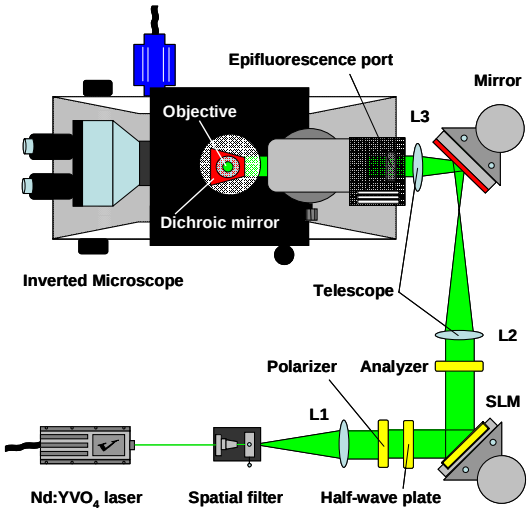


Fig. 1. Optical setup for generating holographic optical tweezers.

#10248 - $15.00 USD Received 10 January 2006; revised 2 March 2006; accepted 6 March 2006

## 3. Algorithm

Given Eq. (1) above, when the spatial light modulator displays the hologram:

$$R(u,v)=\sum_{k=1}^{N} e^{i\frac{2\pi}{\lambda f'}(x_k u+y_k v)}, \tag{2}$$

a set of N off-axis traps will appear at positions $(x_k,y_k)$ on the sample plane, according to:

$$E(x,y)=\sum_{k=1}^{N}\iint e^{-i\frac{2\pi}{\lambda f'}[(x-x_k)u+(y-y_k)v]}dudv=\sum_{k=1}^{N}\delta(x-x_k,y-y_k). \tag{3}$$

Hologram *R(u,v)* is the superposition of N linear phase functions with slopes $(x_k,y_k)$. Unfortunately, *R(u,v)* is not a pure phase function and cannot be directly displayed on a modulator working in a phase-only configuration. Therefore, this problem needs to be solved if optical tweezers arrays by means of holographic optical elements on spatial light modulators are to be generated. The algorithms [7-9, 15-17] try to find a hologram that, being a phase function, does not deviate significantly from the expected goal, that of producing the desired trap array. Such algorithms are usually iterative and computationally expensive.

Our solution is non-iterative. It is an adaptation of the random-mask encoding technique [21] to this particular problem and consists of the multiplication of the linear phase functions in Eq. (2) by spatially disjoint binary masks, i.e.:

$$R(u,v)=\sum_{k=1}^{N} h_k(u,v)e^{i\frac{2\pi}{\lambda f'}(x_k u+y_k v)}, \tag{4}$$

where

$$h_k(u,v)=\begin{cases}1 & iff\ (u,v)\in I_k\\ 0 & otherwise\end{cases}, \tag{5}$$

with

$$I_l\cap I_m=\varnothing\ \ \forall\, l,m \mid l\neq m \quad and \quad \bigcup_{k=1}^{N} I_k=\Re^2\ . \tag{6}$$

That is, the method involves dividing the spatial light modulator into as many subdomains, $I_k$, as traps are required so that these subdomains do not overlap and jointly cover the whole modulator area. Then, each linear phase function is displayed only on the pixels of a given $I_k$. (see Fig. 2).

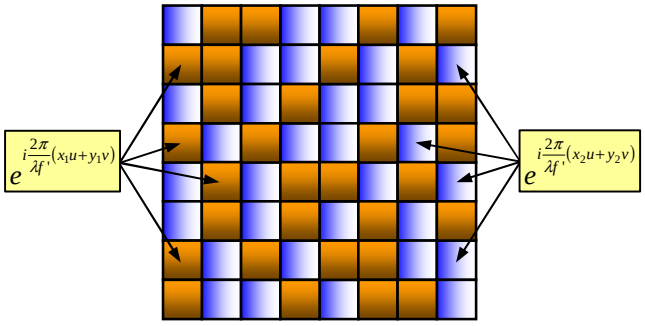


Fig. 2. Encoding two linear phases by complementary random binary masks.

#10248 - $15.00 USD Received 10 January 2006; revised 2 March 2006; accepted 6 March 2006

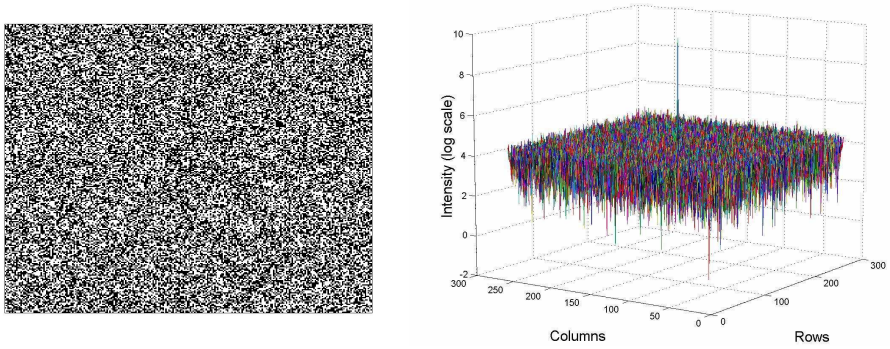


Fig. 3. (a) Binary mask, 256x256 pixels. (b) Magnitude squared of its Fourier transform in logarithmic scale.

With this arrangement, *R(u,v)* is trivially a pure phase function with no further modification.

Applying the convolution theorem [22] and Eq. (3), the field at the sample plane is:

$$E(x,y)=\sum_{k=1}^{N} H_k\left(x-x_k, y-y_k\right), \tag{7}$$

where $H_k(x,y)$ is the Fourier Transform of $h_k(u,v)$. Thus, function $H_k(x,y)$ appears centered at position $(x_k,y_k)$. If the binary masks are selected such that their Fourier transforms $H_k(x,y)$ consist of a single peak with flat sidelobes, then E(x,y) will be a good approximation to the desired array of optical traps.

Random masks, as proposed in Ref. [21], give good results in this respect. For example, Fig. 3(a) shows a random binary mask with 50% of its pixels set to one and the remaining 50% to zero. Figure 3(b) shows the magnitude squared of its Fourier transform, a sharp peak on a small random background. The scale on the Z axis is logarithmic so as better to show small intensity features, since the background is five orders of magnitude lower than the central peak.

Figure 4(a) shows a hologram that encodes a 2x2 array of optical traps using four disjoint binary masks, each of them having active the same number of pixels, one fourth of the total.

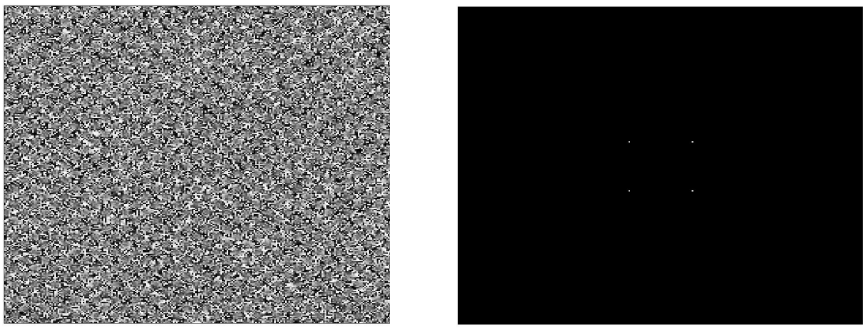


Fig. 4. (a) Hologram encoding an array of 4 optical traps and b) resulting traps.

#10248 - $15.00 USD Received 10 January 2006; revised 2 March 2006; accepted 6 March 2006

Fig. 4(b) shows the resulting traps obtained by computing the Fourier transform of the hologram. Notice the total absence of ghost traps since off-trap energy tends to scatter over the whole sample plane, instead of concentrating at specific locations (giving undesired trapping sites).

It should be finally mentioned that the algorithm can be extended to three dimensions quite straightforwardly by encoding a combination of linear and quadratic phase functions (see for example [9]) with no loss of functionality.

## 4. Additional useful properties

This procedure shows some other useful features that we comment on below.

### *4.1. Intensity control*

The intensity of optical traps generated by the algorithm shows a remarkable uniformity for a small number of traps. For example, in our experiments we have found maximum variations in intensity of less than 4% for arrays of 2x2 optical traps (512x512 pixel holograms). However, for larger arrays (6x6) the intensity variations may increase up to 25%. When this is a problem or if the optical traps have to be of different intensity, a slightly more elaborate algorithm needs to be used [21]. Masks corresponding to traps that are required to be brighter are selected with a somewhat larger pixel count at the expense of other masks (those corresponding to traps need to be weaker).

### *4.2. Incremental updating and hologram multiplexing*

Contrary to other algorithms, all information is very well localized within the binary masks so addition of new trapping sites can be done without recomputing the whole hologram. Specifically, for a hologram of $N$ pixels that encode $m$ traps, $N/[m(m+1)]$ pixels from each binary mask are randomly discarded. Then, the resulting $N/(m+1)$ pixels are used to codify the new linear phase. Only these latter pixels need to be updated.

Interestingly, this can be done over a hologram computed with any other algorithm, in which the information is distributed: discard a number of pixels and use them to produce a new trapping site with the random mask encoding technique. None of the existing traps is more affected than the others, the net effect is a lower-energy set of existing traps and a new trapping site at the desired location. This may be used to temporarily add a new trap to a pre-existing, higher-quality hologram, for example, for loading an array of optical traps with microscopic samples. Finally, the loading trap can be removed by restoring the original pixels.

Figure 5 shows the result of adding a new trapping site to a hologram computed by the Gerchberg-Saxton algorithm [9, 15, 17] to produce an array of 2x2 optical traps. One fifth of its pixels were used to encode the new linear phase function. The figure also illustrates the main drawback of our method. The additional trap is significantly less energetic than equivalent traps computed by the other algorithm.

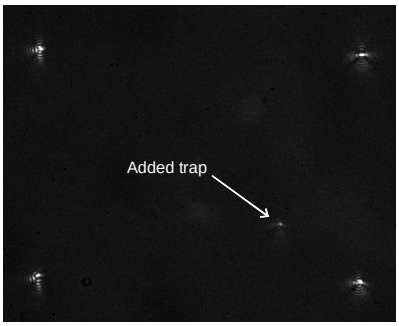


Fig. 5. New trapping site added to a Gerchberg-Saxton hologram.

#10248 - $15.00 USD Received 10 January 2006; revised 2 March 2006; accepted 6 March 2006

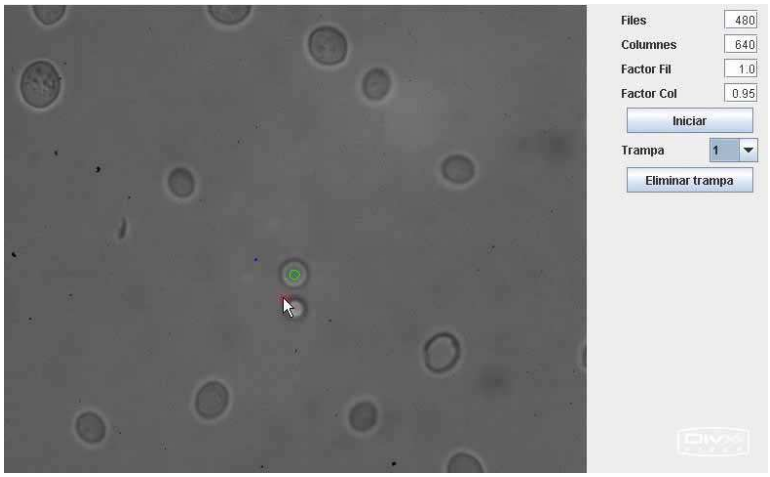


Fig. 6. (2.21 MB) Real-time, interactive manipulation of two yeast cells by means of tweezers generated with the algorithm.

We are further studying the origin of this low efficiency and a possible solution based on reducing the randomness of the binary masks.

Finally, two or more holograms can be multiplexed by multiplication of binary disjoint random masks to merge their individual properties into a single hologram.

*4.3. Speed*

Once the random masks are selected, the hologram can be directly written onto the spatial light modulator without performing any further computation. Thus, the procedure is very fast and can be easily carried out at near video-rates, therefore enabling real-time interaction with the user. We have developed an interactive holographic optical manipulation system based on this algorithm, as shown in the accompanying video (Fig. 6). The control software is implemented in Java and is capable of displaying holograms (512x512 pixels) at an average rate of 10-12 Hz (including aberration correction of the Holoeye SLM and compensation of the operating curve nonlinearities), using a Pentium IV HT, 3.2 Ghz, computer.

## 5. Conclusion

We propose a new procedure for the generation of holographic optical tweezers based on the random mask encoding technique. The result is a direct, non-iterative algorithm that has a number of positive features. Specifically, the algorithm is very fast and video-rate generation is easy to achieve. Moreover, the algorithm does not produce ghost traps and can be used to add further trapping sites to existing holograms, even those generated by other algorithms, without the need to re-compute them. Finally, the main limitation of this procedure seems to be a reduced efficiency, being suitable only to generate a small number of traps.

## Acknowledgments

We would like to thank A. Carnicer for his help during the real-time implementation of the algorithm and to I. Juvells and S. Vallmitjana for many fruitful discussions. Also, we are in debt to D. Petrov and his group at the Institute of Photonic Sciences (ICFO, Barcelona) for their advice on several issues concerning the construction of our optical tweezer setup. This work has been funded by the Spanish Ministry of Education and Science, under grants FIS2004-03450 and NAN2004-09348-C04-03.

# Appendix D

## HoloTrap: Interactive hologram design for multiple dynamic optical trapping

Published in

Computer Physics Communications
Vol.: 176, Issues: 11-12, Jun. 2007

Available online at www.sciencedirect.com
ScienceDirect
Computer Physics Communications 176 (2007) 701–709
Computer Physics Communications
www.elsevier.com/locate/cpc

# HoloTrap: Interactive hologram design for multiple dynamic optical trapping ☆

E. Pleguezuelos *, A. Carnicer, J. Andilla, E. Martín-Badosa, M. Montes-Usategui

*Universitat de Barcelona, Departament de Física Aplicada i Òptica, Martí i Franquès 1, 08028 Barcelona, Spain*

Received 10 January 2007; received in revised form 12 March 2007; accepted 23 March 2007

Available online 30 March 2007

**Abstract**

This work presents an application that generates real-time holograms to be displayed on a holographic optical tweezers setup; a technique that allows the manipulation of particles in the range from micrometres to nanometres. The software is written in Java, and uses random binary masks to generate the holograms. It allows customization of several parameters that are dependent on the experimental setup, such as the specific characteristics of the device displaying the hologram, or the presence of aberrations. We evaluate the software's performance and conclude that real-time interaction is achieved. We give our experimental results from manipulating 5 μm microspheres using the program.

**Program summary**

*Title of program:* HoloTrap
*Catalogue identifier:* ADZB_v1_0
*Program summary URL:* http://cpc.cs.qub.ac.uk/summaries/ADZB_v1_0
*Program obtainable from:* CPC Program Library, Queen's University of Belfast, N. Ireland
*Computer for which the program is designed and others on which it has been tested:* General computer
*Operating systems or monitors under which the program has been tested:* Windows, Linux
*Programming language used:* Java
*Memory required to execute with typical data:* up to 34 MB including the Java Virtual Machine
*No. of bits in a word:* 8 bits
*No. of processors used:* 1
*Has the code been vectorized or parallelized?:* No
*No. of lines in distributed program, including test data, etc.:* 471 145
*No. of bytes in distributed program, including test data, etc.:* 1 141 457
*Distribution format:* tar.gz
*Nature of physical problem:* To calculate and display holograms for generating multiple and dynamic optical tweezers to be reconfigured interactively.
*Method of solution:* Fast random binary mask for the simultaneous codification of multiple phase functions into a phase modulation device.
*Typical running time:* Up to 10 frames per second
*Unusual features of the program:* None
*References:* The method for calculating holograms can be found in [M. Montes-Usategui, E. Pleguezuelos, J. Andilla, E. Martín-Badosa, Fast generation of holographic optical tweezers by random mask encoding of Fourier components, Opt. Express 14 (2006) 2101–2107].


☆ This paper and its associated computer program are available via the Computer Physics Communications homepage on ScienceDirect (http://www.sciencedirect.com/science/journal/00104655).

* Corresponding author.
*E-mail address:* encarni.pleguezuelos@ub.edu (E. Pleguezuelos).

0010-4655/$ – see front matter 
doi:10.1016/j.cpc.2007.03.003

*PACS:* 87.80.Cc; 87.80.y; 42.40.Jv; 42.79.Kr

*Keywords:* Optical tweezers; Interactive manipulation; Digital holography; Spatial light modulators

## 1. Introduction

In this paper we describe an application that interactively generates multiple dynamic holographic optical tweezers. The program allows the user to compute holograms displayed in an optical tweezers setup, resulting in trap patterns that are reconfigurable in real time. Experimental setup factors are application parameters resulting in a completely customizable program.

Optical tweezers are generated by strongly focusing a laser beam, thus creating an optical gradient that traps dielectric particles from micrometric samples down to the nanometric scale [1], due to the transfer of light momentum to the trapped particle. This technique has many applications in the manipulation of biological samples [2] because it is harmless if the trapping light wavelength is not absorbed by the sample (that is, in the infrared) and the forces involved in molecular and biological processes (which are in the same range as the forces applied by optical tweezers—about pN) can be measured.

Holography allows the synthesis of a light wavefront by spatially modifying the amplitude and phase of the beam [3]. Knowing how light propagates in the setup allows us to determine the relationship between the field amplitudes in any two planes along the optical train. In this way, we can calculate the hologram that reconstructs a desired light distribution on another plane. The use of digital holography in optical tweezers provides a lot of flexibility in the design of trap patterns. This technique has resulted in the introduction of large arrays of optical traps and three-dimensional control [4,5]. Moreover, the shape and properties of the beam can be modified to generate non-Gaussian beams such as vortex beams, which are capable of transferring angular momentum to the trapped particle [6], or non-diffracting beams [7].

Spatial Light Modulators (SLMs), which are used to display digital holograms, allow dynamic, computer-controlled modification of the complex transmittance/reflectance of the device. The relationship between the sample plane and the hologram plane is an inverse Fourier transform, so, in general, the hologram is complex. These devices are constrained to display a set of complex transmittance values, so we should limit our hologram values to those available from the modulator. Algorithms have to be designed to find an optimal solution constraining the hologram to the discrete set of values accessible. These algorithms are based on iterative methods [8,9] or on extensive search procedures [10]. Both approaches are time consuming and do not allow real-time interaction with the sample, since they cannot be calculated and displayed as fast as necessary. We recently proposed a method for calculating holograms in order to generate optical tweezers. It is based on the random mask encoding method for multiplexing phase-only filters [11], and is, to our knowledge, the fastest method with 3D control of the trap. This is because it is not iterative and the number of operations involved is lower than in other direct methods, such as the gratings and lenses (or prisms and lenses) method [12]. Another advantage of the algorithm is that it does not produce the ghost traps or replicas reported in other methods [13].

Other possibilities—such as the generalized phase contrast approach [14] or time sharing of the laser beam—allow real-time interaction with the sample, but are limited to two-dimensional trap patterns and do not allow generation of non-Gaussian beams. The gratings and lenses method has also been used to calculate the desired trap pattern for interactive hologram generation applications, in a LabVIEW click-and-drag interface [15], with an interface that allows the manipulation of samples by means of the user's hands [16] or by direct programming of the graphics card [17]. This last technique allows a faster update rate by taking advantage of the Graphics Processing Unit (GPU) acceleration capabilities. Other applications are designed to be used with their commercial setup and do not allow customization [18].

We present software developed to interact with trapped particles in real time. The application calculates and displays the holograms that generate the trap pattern according to the user's commands. In Section 2 we outline the experimental setup, emphasizing the aspects that have to be taken into account in the software design. The implemented algorithm is explained in Section 3. The developed application, written in Java™ 2 Platform Standard Edition 5.0 is detailed in Section 4. The sample plane is visualized on another monitor, using the camera. The camera image can be integrated in the program. We show how to do that in Section 4.3. However, the camera driver is proprietary and cannot be attached due to licensing restrictions. The performance of the software and experimental results are given in Section 5.

## 2. Holographic optical tweezers

In optical trapping, a highly focused laser beam exerts gradient forces on the sample. Typically, an inverted microscope is modified to focus the beam, while still being able to image the sample. Fig. 1 shows our experimental setup. The laser is a frequency-doubled Nd:$YVO_4$ laser from Viasho Technologies. The laser beam is expanded and collimated before being reflected by the Spatial Light Modulator, a HoloEye LCR-2500. On reflection, the SLM modulates the phase of the wavefront. The beam size is reduced using an auxiliary telescopic system (lenses L1 and L2 in Fig. 1), to adapt it to cover the whole of the objective's aperture; which is important for stable trapping [1]. The beam is fed into the inverted microscope (a Nikon TE2000) through a rear aperture, usually used in fluorescence imaging, and focused in the sample plane by the microscope objective (a Plan Fluor 100X Nikon oil-immersion objective with numerical aperture 1.3). Further information about the design of our experimental setup can be found in [19].

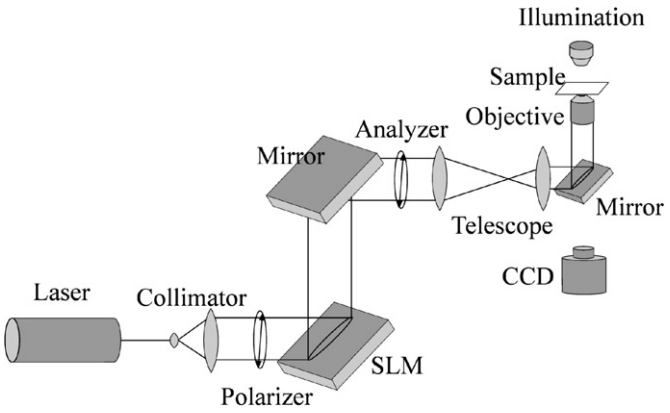


Fig. 1. Holographic optical tweezers setup.

The sample is placed at the focal plane of the objective, so the relationship between the device and the sample is an inverse Fourier transform except for multiplicative phase terms that do not affect our discussion [20]:

$$H(u,v) = \iint_{-\infty}^{\infty} g(x,y) e^{-i\frac{2\pi}{\lambda f'}(xu+yv)}\,\mathrm{d}x\,\mathrm{d}y, \tag{1}$$

where $H(u,v)$ is the hologram, $g(x,y)$ the trap pattern, $\lambda$ the wavelength of the light and $f'$ the focal length of the objective. The wavelength, the telescope, the modulator and the objective determine the scale factor between our sample plane and the hologram. This is left as a parameter in the application, as explained in Section 4.

The introduction of the Spatial Light Modulator allows us to design the shape of the beam by spatially modifying the amplitude and phase of the light distribution in the plane where the modulator is placed. There are different kinds of SLM, such as liquid crystal displays (LCDs) in which the grey level sent to each pixel of the modulator is translated into a change in amplitude and phase of the incident beam at that point, thus achieving spatial control of the light distribution. The modulation also depends on the polarization of the input and output light. It is necessary to know the modulation response for each grey level. This can be achieved by characterizing the device modulation with the polarization conditions [21] in which it will be used. The most common configuration is phase-only modulation, which has the least amplitude variation.

LCDs are unable to modulate the whole complex plane [22]. Fig. 2 shows the experimental characterization of the LCD we use, a HoloEye LCR-2500. It shows the complex transmittance value that corresponds to each grey level. It is almost a phase modulation from 0 to $2\pi$, although there is a small amplitude modulation. The hologram values have to be built using the available modulation values. To do this, the minimum Euclidean distance between the phase in each pixel and the available phase values is calculated, and the nearest phase modulation value is used to display the theoretical hologram value.

To summarize, our synthesized hologram is a grey-level image that results in a local modification of the phase of the incident wavefront, and will generate a given trapping pattern in the focal plane of the objective (where the sample is located).

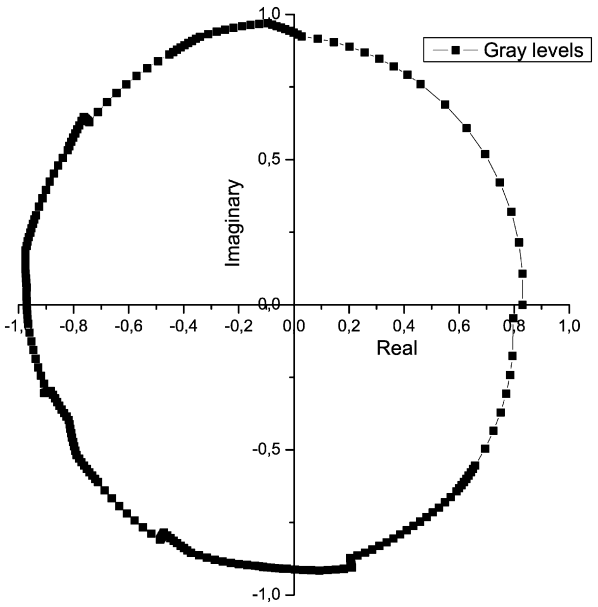


Fig. 2. Experimental complex modulation values of the SLM as a function of the gray level.

## 3. Fast method of hologram calculation

In order to generate holograms in real time we have to use direct methods of calculation as opposed to iterative methods. Direct methods consist of generating the hologram from analytic solutions, that is, determining analytically the inverse Fourier transform of the trap pattern taking into account that one is limited in general to phase functions due to modulation constraints. Holographically we have the ability to set the three-dimensional position of each trap. A trap centred at $(a,b)$ can be described as $g(x,y) = \delta(x-a, y-b)$. The hologram that generates this distribution is its Fourier transform, that is:

$$H_D(u,v) = \mathcal{F}^{-1}\big(g(x,y)\big) = \exp\left(i\frac{2\pi}{\lambda f}(u\cdot a + v\cdot b)\right). \tag{2}$$

If the trap is focused at a depth $z$ from the focal plane, the required function is a quadratic phase term such as:

$$H_Z(u,v) = \exp\left(i\frac{2\pi}{\lambda z}(u^2+v^2)\right), \tag{3}$$

whose Fourier transform is another quadratic phase function.

To generate a vortex, which can transfer angular momentum to the trapped particle [23], the following phase function is needed:

$$H_V(u,v) = \exp\left(i\cdot l\tan^{-1}\left(\frac{v}{u}\right)\right), \tag{4}$$

this function modifies the wavefront to convert it to a Laguerre–Gaussian mode, which carries angular momentum. The quantity $l$ is called the topological charge and is related to the orbital angular momentum of each photon by $L = l\hbar$.

In these examples the solution is a pure phase function, so codifying it using phase-only modulation is straightforward: simply choose the closest phase given by the device. However,

if $N$ traps are required, the hologram is a sum of as many phases as traps displayed, resulting in a complex function that cannot be directly displayed with a phase-only modulation:

$$H(u,v) = \sum_{k=0}^{N} (H_{Dk} + H_{Lk} + H_{Vk}) \neq \exp\bigl(i\phi(u,v)\bigr). \tag{5}$$

The method for the codification of the hologram cannot be time-consuming if we require it to be implemented in real time. Our approach, more detailed in [11], defines as many different domains $I_k$ of the modulator as traps to be displayed. Each domain consists of a set of modulator pixels that shows a phase function. In this way, each set is in charge of generating a single trap. The hologram (Eq. (6)) consists in the multiplication of the phase functions, $H_k(u,v)$ (as in Eqs. (2) and (3)) by spatially disjoint binary masks, $m_k(u,v)$—the set of pixels of the domains $I_k$.

$$H(u,v) = \sum_{k=0}^{N} m_k(u,v) \cdot H_k(u,v), \tag{6}$$

where

$$m_k(u,v) = \begin{cases} 1 & \text{if } (u,v) \in I_k, \\ 0 & \text{elsewhere.} \end{cases}$$

The domains $I_k$ do not overlap, and together they cover the whole modulator. For example, we can generate the domains by randomly deciding which pixels will belong to each trap. This is a good choice since the mask that defines every sub-hologram is not a geometric function: the convolution of the shape of the trap with the Fourier transform of the mask would result in noise distributed through the resulting plane [11]. This noise distribution prevents the apparition of replicas reported in other methods [13], which tend to concentrate the energy not located in the traps in bright spots, resulting in false traps. As can be seen, the solution is as fast as generating the $I_k$ domains each time a trap is added or deleted, and computing the arguments of the complex exponentials $H_k(u,v)$ to display the hologram. Fig. 3 shows an example of a hologram in which half of the pixels display a linear phase function and the other half a quadratic phase. The resulting light distribution would be two different traps placed off-centre, at two different depths.

This method is—to our knowledge—the fastest way to generate simple trap patterns. The most common fast method for the generation of optical tweezers (the gratings and lenses method) consists of generating the analytic hologram from Eq. (5) and discarding the amplitude information. This method is slower than our random binary masks method because the calculation time increases with the number of traps and requires the computation of trigonometric functions [12]. Due to the discarded amplitude information, the intensity distribution among the traps may be different from that expected. Another advantage of our random binary masks method is, as it has been already explained, that the trap pattern generated does not present replicas. The downside is that the efficiency of the traps is lower than that achieved with other methods.

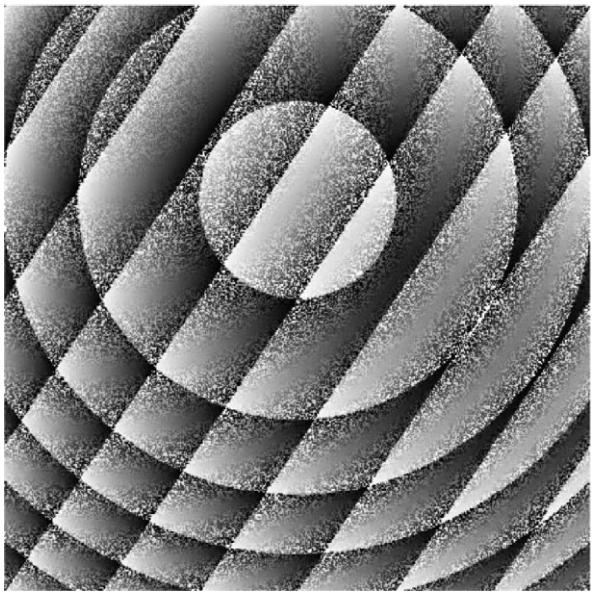

Fig. 3. Hologram calculated using the random binary masks method.

## 4. Description of the program

The software we present calculates and displays holograms to generate optical tweezers allowing real-time interaction with samples. Each change in the number or position of the trap requires recalculation of the hologram. The program responds quickly enough to provide close to video-rate feedback from the sample.

The reason for using Java is that development costs are low. Moreover Java allows easy generation of the Graphical User Interface (GUI) and easy integration with C++ generated dlls; the most generalized hardware driver distribution method. Another advantage of using Java is simple remote control of the experiment over the Internet. If the computer controlling the camera acts as a web server, you just have to transform the program generated into a Servlet and use the Remote Method Invocation (RMI) classes.

The source code is distributed into three different classes. The first class, TRBase, generates the GUI and handles the events related to the input parameters. It also initiates the second class, PanelCoord, the panel in which the user clicks and drags to generate and move a trap, and so this class monitors these mouse events and calls to the third class, FrameHolo. This third class calculates and displays the hologram using the mouse coordinates and the input parameters. The documentation of the application, in which the different classes and implemented methods are detailed, can be found in the folder */html* zipped within the application jar file. This documentation can be also found in our website [24].

### 4.1. Graphical User Interface

A screen capture of the GUI can be found in Fig. 4. This program allows user control of several variables and initial data:

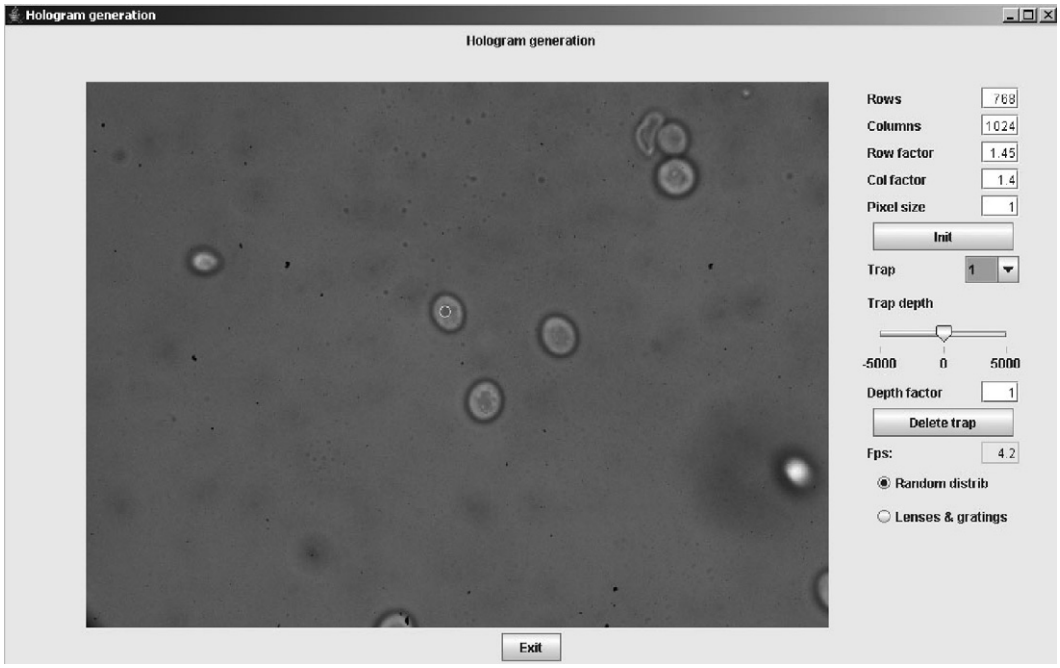


Fig. 4. Application user interface.

- The hologram size, in pixels. If the size is set to $1024 \times 768$, which is our SLM full resolution, the hologram is calculated with half the number of and zoomed to fill the modulator, reducing computation time. Any other resolution can be used.
- The scale factors between the Spatial Light Modulator plane and the visualization plane. These factors multiply the coordinates in rows and columns of the hologram, allowing us to adjust the position of the traps with the position of the mouse coordinates. They can be found experimentally by changing the scale factor and checking the trap position, a trial and error procedure. The analytic expression of the factors can be inferred from the geometric magnification due to the telescope, the Fourier transform scale factor given by the objective lens and the light wavelength and from CCD scale factor. The resulting relationship is:

$$\text{Row factor} = \frac{N_y}{\lambda f}\frac{f_2}{f_1} p_y \beta,$$
$$\text{Column factor} = \frac{N_x}{\lambda f}\frac{f_2}{f_1} p_x \beta, \tag{7}$$

  where $N_y$ and $N_x$ are the number of rows and columns of the hologram, $\lambda$ is the laser wavelength, $f_1$ and $f_2$ the focal length of L1 and L2 (the telescope lenses), $f$ the focal length of the objective lens, $p_x$ and $p_y$ are the SLM pixel size in each direction and $\beta$ is the CCD factor between pixel and micrometers of the field of view. The Intro key has to be pressed after changing the factor.
- The Init button asks for a file containing a precalculated map of the phase modulation and a phase aberration correction (see Section 4.2). In our case, the aberration is a distortion of the wavefront due to the curvature of the modulator surface but other aberration correction can be considered. There is an example of a phase-only function map and a null aberration correction attached in the *.jar* file to check the required format. To run the application using these two ideal condition files, after pressing the Init button, just press OK on the dialog box "Use the default aberration and modulation files". Each time a hologram is generated, the correction is added and then the nearest grey value is assigned using the precalculated map. If the user SLM has been characterized the nearest grey value map can be computed and loaded in the application instead of the ideal phase function we attach.
- A selector allows you to choose the manipulated trap if more than one trap is generated. The selected trap is indicated by a red circle, whereas the unselected traps are in green.
- A slider allows you to modify the trap depth, from $-5$ to 5 μm. The "Depth Factor" text field allows you to modify the available depth range.
- By changing the integer in the "lvortex" text field (see Fig. 4) an optical vortex carrying angular momentum is generated by adding a vortex phase function (Eq. (4)) with the specified topological charge.
- The Delete trap button deletes the selected trap. This involves a reconfiguration of the random binary masks, which have to be recalculated.
- The hologram is calculated by the method selected in the Radio Button. The default calculation method is random binary masks, but gratings and lenses is also available.

### 4.2. Calculating and displaying a hologram

This section details the computational process of generating a hologram, see Fig. 5. First, the application is initiated and the user enters the desired parameters (such as hologram size

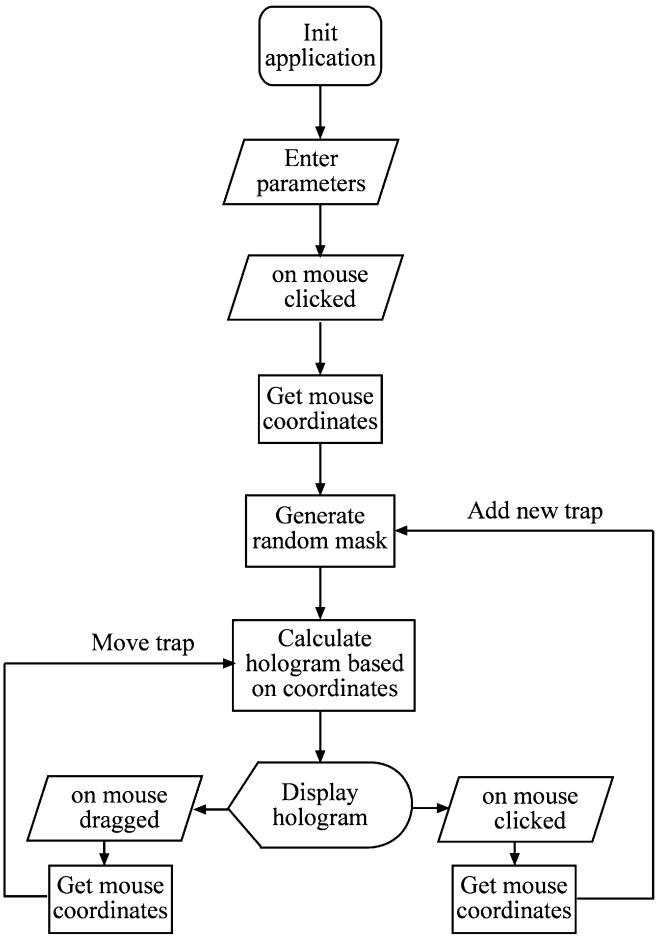


Fig. 5. Program flowchart.

or scale factors). The central panel in the application controls the event handling of the user interaction. When the mouse is clicked on the panel, the mouse coordinates are obtained. The random mask is calculated, resulting in the whole modulator, because there is one single trap in this first step. With the mouse coordinates, a phase grating corresponding to the trap is calculated (Eq. (2)) and the hologram is displayed. Each time another trap is added, the random binary masks have to be calculated and then each set of pixels show the corresponding phase function. If the mouse is dragged or the depth slider is moved, the coordinates of the selected trap change. A change in the coordinates of a single trap means that only the pixels of the mask corresponding to that trap have to be recalculated.

To generate traps in real time, the algorithm has to be fast, but there are also other considerations that affect the performance of the process. We have optimized the process of adaptation of the hologram to the modulation values by generating a map of the correspondence between all the possible phase values between 0 and $2\pi$ and the nearest phase given by a grey level. In general this is not a linear relationship. The phase value assigned to each grey level is stored in a file that the program reads as an initial parameter. An example of an ideal phase assignment can be found in the *map_ideal.txt* file distributed in the jar. Once the analytical phase value is calculated, the map provides the grey level to be displayed. An incorrect assignment can cause variations in the reconstructed trap pattern.

Another experimental issue that affects the calculation time is the possible existence of aberrations in the optical system, which can be corrected with the SLM when generating the trap pattern. In our case, the modulator reflected wavefront is distorted because the device is not flat. We can correct this aberration by adding a fixed phase pattern to each hologram. As an example, the file *phaberr*_1024x768.*txt* is a null aberration correction attached in the jar file, that shows the format of the aberration file for the specified hologram size.

In order to ensure a fast response of the displayed hologram, two main factors have to be taken into account. First, the hologram generation has to be as fast as possible, including algorithm calculation, addition of the aberration correction and adaptation to the modulation. Second, speed of access to the graphic hardware has to be ensured. Our approach is to take advantage of the *VolatileImage* class in the Java SDK. The hologram is stored as a hardware-accelerated off-screen image, in such a way that rendering operations are accelerated through the graphics card. Thus, hologram is displayed without using the CPU. This class parallelizes the display of the hologram and the calculation processes, with the CPU performing the calculation.

The hologram is displayed in an independent window, which can be placed anywhere in the screen. The most common way to display an image onto a SLM is to setup this device as a second monitor of your computer. This can be achieve by defining a second monitor in the screen's configuration options of the operating system. Once activated, this second screen can be used as an extension of the desktop. Consequently, the hologram window can be dragged into the second monitor-SLM in order to have it displayed.

### 4.3. Camera control

The image of the sample can be displayed on another monitor to control manipulation. Our program is enhanced if the camera image is incorporated into the interactive interface, although it can be used with the image separated from it. In this section we explain how we integrated our video stream management, as a guide for users on how to embed their own. We used a QICam Fast 1934 from QImaging Corp. [25] camera. It is not compliant with the IIDC Digital Camera Specification (DCAM), which is the standard protocol FireWire cameras should follow, so the SDK provided by the manufacturer had to be used. This is a drawback to distributing the camera-integrated version of the program, and so a version without a camera accompanies the paper. If a DCAM-compliant camera is used, the Java API for FireWire *jlibdc*1394 [26] can be incorporated into the program instead of the camera SDK, making it suitable for all DCAM-compliant cameras.

The Qimaging libraries have to be used with a C++ compiler, so the Java Native Interface (JNI) class [27] is needed to embed the camera library into the Java structure. JNI is a common trick for gaining compatibility with native methods across a Java virtual machine. We need the following native functions:

public native int initCamera(); (Detects the camera)
public native int initGrab(); (Initiates the recording)
public native int doGrab(byte[] pix); (Saves the image into a pixel array)
public native int StopGrab(); (Stops recording)

Each native Java method has its corresponding function in C++. The process of calling from a Java program code contained in the proprietary library is [27]:

- Declaration of the native methods in the Java application, in our case the methods listed above.
- The loading of the library containing the native code implementation, by calling the function *System.load("JNIQCam.dll")*, where 'JNIQCam.dll' is our generated library name (even it does not exist yet). The Java application has to be compiled at this point without being executed. This library is not the proprietary library, but one generated by the user, defining what each native method does.
- Generation of the header (.h) file that contains the interface assigning the Java methods to the C native functions. As an example, the functions are defined in this header as:

  JNIEXPORT jint JNICALL Java_initCamera(JNIEnv*, jobject);
  JNIEXPORT jint JNICALL Java_initGrab(JNIEnv*, jobject);
  JNIEXPORT jint JNICALL Java_doGrab(JNIEnv*, jobject, jbyteArray);
  JNIEXPORT jint JNICALL Java_StopGrab(JNIEnv*, jobject);

  This file is the communication channel between the two languages.
- Creation of the C++ functions. The library (JNIQCam.dll) has to contain the C++ source calling to the camera library. As an example, our C++ method that disconnects the camera is:

```
JNIEXPORT jint JNICALL Java_tr_StopGrab(JNIEnv*, jobject){
delete [] pixels;
if(hCamera != NULL)
{
QCam_CloseCamera(hCamera);
}
QCam_ReleaseDriver();
return 0;
}
```

  In this example we free the image memory through the *delete* order. The calling to *CloseCamera(hCamera)* frees the *hCamera* object, *hCamera* is the object initiated in the method *initCamera*, which contains the camera properties and prevents other applications accessing the camera. Next, the camera driver is released with the command *ReleaseDriver()*.
- Compilation and execution of the code.

If the user had the same camera, a.dll file should be generated and the commented lines in the.java source, marked as "//Comment if there is no QICam available", should be uncommented.

## 5. Performance of the software

Fig. 4 shows a screen capture of the program. The tests were carried out on a Pentium IV HT, 3.2 GHz, with lite versions of

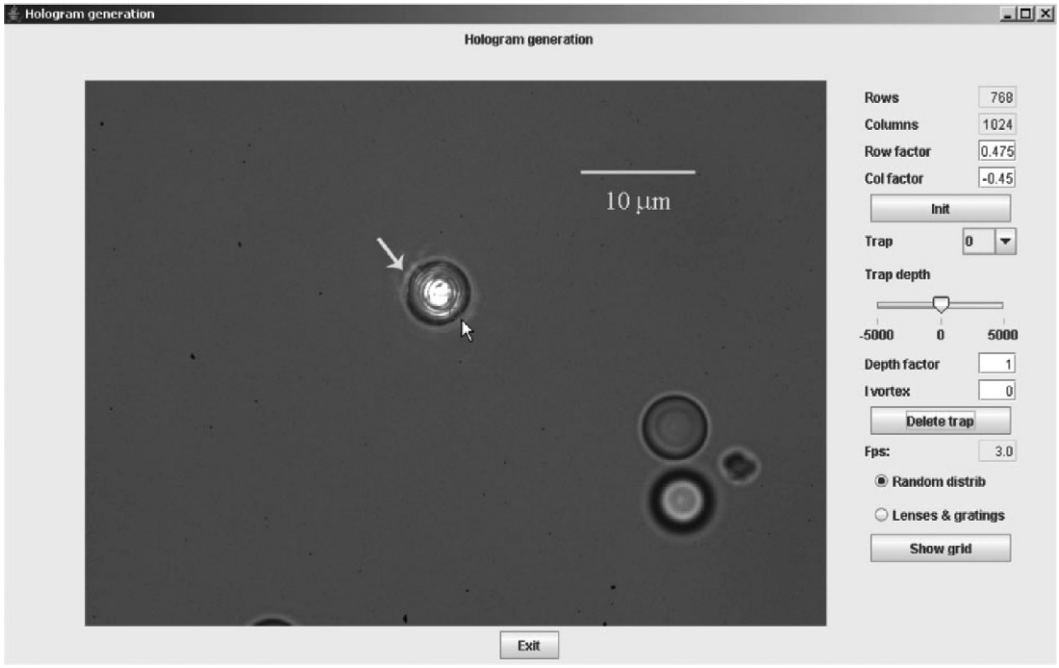


Fig. 6. Screen shots showing the experimental manipulation of polystyrene beads, 5 µm diameter.

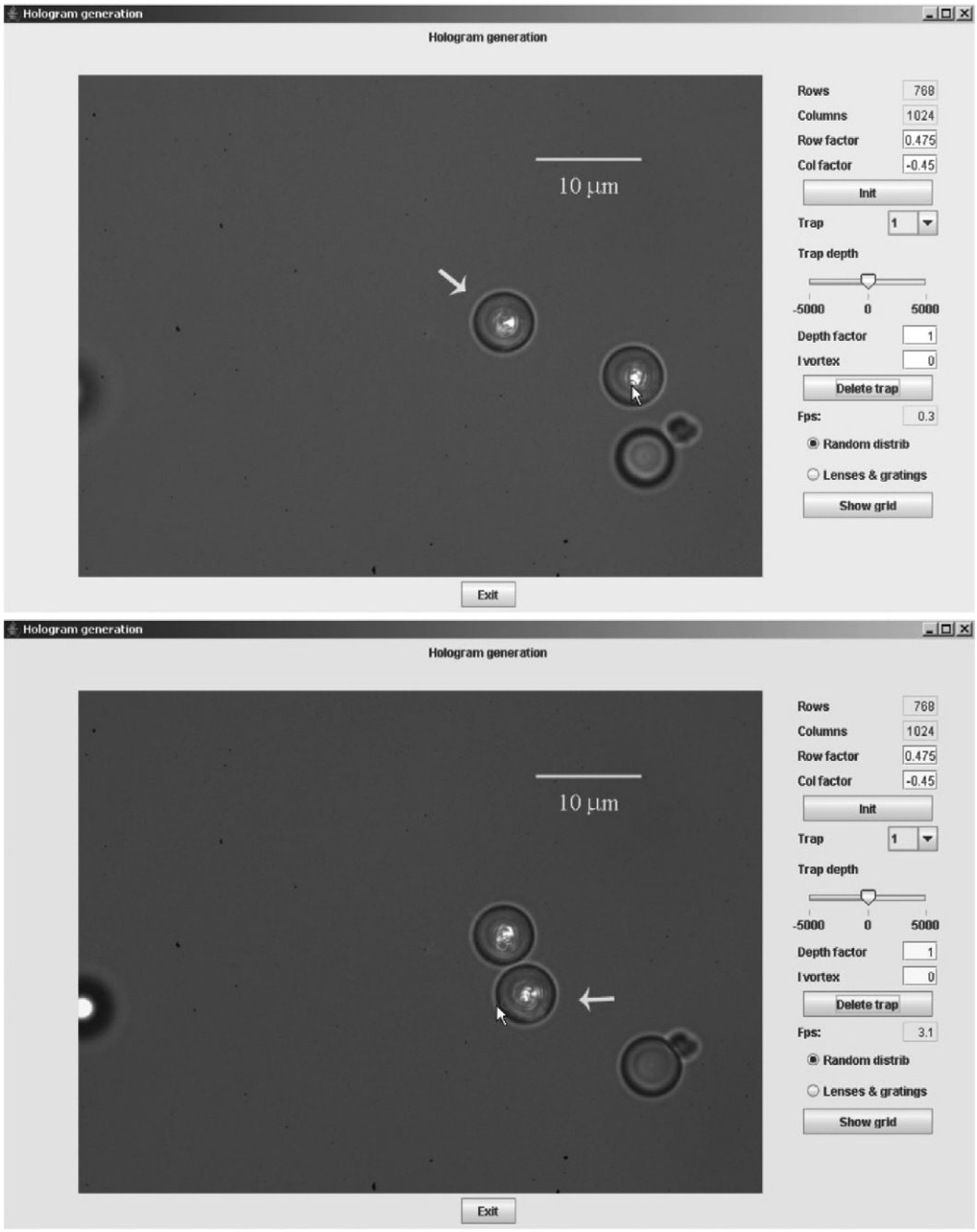


Fig. 6. *Continued*.

the program, where not all the options were available. These lite versions can be obtained from our website [24].

The speed of the software when generating holograms in response to a mouse drag is about 10 fps (frames per second). This value measures the number of holograms displayed per second on the modulator. The full resolution sized holograms are achieved by calculating holograms of $512 \times 384$ pixels and resizing them into $1024 \times 768$ pixels. The adaptation mapping that we have created from the experimental phase modulation values does not affect the speed of the hologram generation. In contrast, the inclusion of the aberration correction affects slightly the performance by decreasing the hologram calculation speed. The time response does not increase with the number of traps, because the number of pixels the phases have to be computed for (the number of pixels defining each mask) decreases as the number of traps increases.

Fig. 6 shows screen shots of experimental manipulation of polystyrene beads of 5 μm diameter. A first microsphere is captured and dragged close to another, which is trapped and moved with a second trap.

## 6. Concluding remarks

We have presented an application for calculating and displaying holograms in real time to generate multiple recon-

figurable optical tweezers. The application allows the user to generate, delete or modify optical traps interactively. We used the random binary masks method because of its speed. The software takes into account different parameters given by the experimental setup, and so it is not limited to a single configuration. The different options have been detailed, including the adaptation to the modulation and the correction of possible aberrations. The scale factor and the hologram size can also be modified. Some strategies for accelerating hologram calculation and display are explained. A second version of the program takes advantage of the proprietary libraries of the camera used in order to embed the image provided by the camera and the program. The viability of the software is comparable to that of other applications in the literature. We include an example of optical manipulation using this program. In future work we would like to make the software compatible with IICAM-compliant FireWire cameras.

## Acknowledgements

This work has been funded by the Spanish Ministry of Education and Science, under grants FIS2004-03450 and NAN2004-09348-C04-03.

## References

[1] A. Ashkin, Optical trapping and manipulation of neutral particles using lasers, Proc. Natl. Acad. Sci. USA 94 (1997) 4853–4860.
[2] K.C. Neuman, S.M. Block, Optical trapping, Rev. Sci. Instrum. 75 (2004) 2787–2809.
[3] R. Tudela, I. Labastida, E. Martín-Badosa, S. Vallmitjana, I. Juvells, A. Carnicer, A simple method for displaying Fresnel holograms on liquid crystal panels, Opt. Commun. 214 (2002) 107–114.
[4] G. Sinclair, P. Jordan, J. Courtial, M. Padgett, J. Cooper, Z. Laczik, Assembly of 3-dimensional structures using programmable holographic optical tweezers, Opt. Express 12 (2004) 5475–5480.
[5] Y. Roichman, D. Grier, Holographic assembly of quasicrystalline photonic heterostructures, Opt. Express 13 (2005) 5434–5439.
[6] P. Prentice, M. MacDonald, T. Frank, A. Cuschier, G. Spalding, W. Sibbett, P. Campbell, K. Dholakia, Manipulation and filtration of low index particles with holographic Laguerre–Gaussian optical trap arrays, Opt. Express 12 (2004) 593–600.
[7] S.H. Tao, X.-C. Yuan, B.S. Ahluwalia, The generation of an array of non-diffracting beams by a single composite computer generated hologram, J. Opt. A.: Pure Appl. Opt. 7 (2005) 40–46.
[8] R.W. Gerchberg, W.O. Saxton, A practical algorithm for the determination of the phase from image and diffraction plane pictures, Optik 35 (1972) 237–246.
[9] V. Soifer, V. Kotlyar, L. Doskolovich, Iterative Methods for Diffractive Optical Elements Computation, Taylor & Francis Ltd, London, 1997.
[10] M.A. Seldowitz, J.P. Allebach, D.W. Sweeney, Synthesis of digital holograms by direct binary search, Appl. Opt. 26 (1987) 2788–2798.
[11] M. Montes-Usategui, E. Pleguezuelos, J. Andilla, E. Martín-Badosa, Fast generation of holographic optical tweezers by random mask encoding of Fourier components, Opt. Express 14 (2006) 2101–2107.
[12] J. Liesener, M. Reicherter, T. Haist, H.J. Tiziani, Multi-functional optical tweezers using computer-generated hologram, Opt. Comm. 185 (2000) 77–82.
[13] M. Polin, K. Ladavac, S.-H. Lee, Y. Roichman, D. Grier, Optimized holographic optical traps, Opt. Express 19 (2005) 5831–5845.
[14] P. Rodrigo, V. Daria, J. Glückstad, Real-time interactive optical micromanipulation of a mixture of high- and low-index particles, Opt. Express 12 (2004) 1417–1425.
[15] J. Leach, K. Wulff, G. Sinclair, P. Jordan, J. Courtial, L. Thomson, G. Gibson, K. Karunwi, J. Cooper, Z.J. Laczik, M. Padgett, Interactive approach to optical tweezers control, Appl. Opt. 10 (2006) 897–903.
[16] G. Whyte, G. Gibson, J. Leach, M. Padgett, An optical trapped microhand for manipulating micron-sized objects, Opt. Express 14 (2006) 12497–12502.
[17] M. Reicherter, S. Zwick, T. Haist, C. Kohler, H. Tiziani, W. Osten, Fast digital hologram generation and adaptative force measurement in liquid-crystal-display-based holographic tweezers, Appl. Opt. 45 (2006) 888–896.
[18] BioRyx® 200, http://www.arryx.com/bioryxsoftware.html.
[19] E. Martín-Badosa, M. Montes-Usategui, A. Carnicer, J. Andilla, E. Pleguezuelos, I. Juvells, Design strategies for optimizing holographic optical tweezers setups, J. Opt. A: Pure Appl. Opt., submitted for publication; available at http://arxiv.org/abs/physics/0701037.
[20] J.W. Goodman, Introduction to Fourier Optics, McGraw-Hill, 1996.
[21] E. Martín-Badosa, A. Carnicer, I. Juvells, S. Vallmitjana, Complex modulation characterization of liquid crystal devices by interferometric data correlation, Meas. Sci. Technol. 8 (1997) 764–772.
[22] R. Tudela, E. Martín-Badosa, I. Labastida, S. Vallmitjana, I. Juvells, A. Carnicer, Full complex Fresnel holograms displayed on liquid crystal devices, J. Opt. A: Pure Appl. Opt. 5 (2003) S189–S194.
[23] J.E. Curtis, B.A. Koss, D.G. Grier, Dynamic holographic optical tweezers, Opt. Comm. 207 (2002) 169–175.
[24] HoloTrap documentation, http://www.ub.edu/optics/holotrap.
[25] Qimaging Corporation, http://www.qimaging.com/.
[26] Java API for FireWire, http://jlibdc1394.sourceforge.net/.
[27] Java Native Interface, http://java.sun.com/j2se/1.4.2/docs/guide/jni/index.html.

# Appendix E

## Correction of aberration in holographic optical tweezers using a Shack-Hartmann sensor

Sent to

Applied Optics
Sep. 2008

# Correction of aberration in holographic optical tweezers using a Shack-Hartmann sensor

**C. López-Quesada, J. Andilla and E. Martín-Badosa***

[1]*Grup de Recerca en Òptica Física, Departament de Física Aplicada i Òptica, Universitat de Barcelona*

*Martí i Franquès, 1, Barcelona 08028, Spain*

**Corresponding author: estela.martinb@ub.edu*

Optical aberration due to the non-flatness of spatial light modulators used in holographic optical tweezers significantly deteriorates the quality of the trap and may even prevent stable trapping of particles. We use a Shack-Hartmann sensor to measure the distorted wavefront at the modulator plane; the conjugate of this wavefront is then added to the holograms written into the display to counteract its own curvature and thus compensate the optical aberration of the system. For a Holoeye LC-R 2500 reflective device, flatness is improved from 0.8λ to λ/16 (λ = 532 nm), leading to a diffraction-limited spot at the focal plane of the microscope objective. This process could be fully automated in a closed-loop configuration and would eventually allow other sources of aberration in the optical setup to be corrected for. 2008 Optical Society of America

*OCIS codes: (230.6120) Spatial light modulators; (090.1000) Aberration compensation; (140.7010) Laser trapping.*

## Introduction

Optical tweezers are strongly focused laser beams capable of trapping microscopic particles [1]. They have proved to be a very useful tool for exerting and measuring forces on micrometer-sized objects, and have promising applications in cell and molecular biology [2]. The introduction of holograms displayed on spatial light modulators (SLMs) has greatly improved the design of optical tweezers [3-6]. SLMs spatially modify the laser wavefront before the focusing step, resulting in a completely programmable dynamic intensity pattern over the sample plane. Wavefront control easily permits three-dimensional positioning of the traps as well as the creation of beams with special characteristics, such as Bessel or Laguerre-Gaussian beams [7], which carry angular momentum.

In optical tweezers, the gradient component of the light force needs to be greater than the scattering component to guarantee stable trapping, and thus high numerical aperture (NA) microscope objectives are used to bring light to a tight focus. These are very well corrected to form diffraction-limited optical traps, commonly at small distances from the cover glass. The quality of the trap degrades rapidly as depth increases due to spherical aberration arising from refractive index mismatch at the glass-water interface [8,9]. In [10,11] the axial trapping force was enhanced by correcting this aberration with a deformable mirror. Other aberrations, such as optical misalignment or even that caused by the refractive index distribution of the specimen, should be compensated for as well to ensure a diffraction-limited spot. Optical vortices are especially sensitive to aberrations both in their shape and in the distribution of light around their circumference [12-14].

SLMs have proved to be a useful tool for generating Zernike polynomials [15] and correcting aberrations in adaptive optical systems [16-18]. Recently, liquid crystal on silicon (LCoS) technology has provided high resolution, small pixel size and large fill factors at relatively low costs [19]. An LCoS micro-display essentially consists of a liquid crystal layer sandwiched between a cover glass and a silicon backplane that contains the drive electronics and which is commonly coated with aluminum to ensure high reflectivity. The micro-display operates by reflection in a double-pass beam path which increases the phase modulation range and thus makes it particularly suitable for wavefront applications, in which $2\pi$ modulation depth is desirable.

Unfortunately, the silicon backplane manufactured using standard CMOS methods is not flat [20], which frequently gives rise to important optical aberration. Such distortion is too strong to ignore when using SLMs for wavefront control in applications such as laser beam steering, diffractive optical element generation or emulation of atmospheric turbulence. Therefore, much effort has been made to measure and correct the static aberrations of LCoS displays, mainly by interferometry. In [18, 21-23] a Boulder Nonlinear Systems (BNS) SLM [24] of the XY Phase Series (P256 or P512 model, depending on the reference) is characterized, while in [25,26] a Hana Microdisplay device [27] is analyzed. Furthermore, Holoeye devices [28] are dealt with in [22] (Holoeye HEO 1080P) and [14] (Holoeye LC-R 720). In the latter, Jesacher *et al.* use the high sensitivity to aberrations of Laguerre-Gaussian modes to determine the phase errors from the distorted shape of a focused doughnut mode: a phase retrieval algorithm is applied to find the hologram that would produce the observed distorted doughnut if displayed on an ideally flat SLM and imaged with "perfect" optics. This method could be applied in holographic optical tweezers, in which aberrations of the SLM might dominate compared to optical misalignments and microscope objective malfunction, as pointed out above.

M. Reicherter and co-workers present in [29] a method to correct aberrations in microscopy inspired by astronomy, in which an illuminated microsphere serves as a nearly spherical reference wavefront. Holographic optical tweezers are used to move this artificial point source within the object space, thus enabling spatially selective aberration measurement. The emitted wavefront is analyzed using either a fiber interferometer or a Shack-Hartmann wavefront sensor. The complex conjugate of the measured distorted wavefront is then written into the same SLM that is used for the manipulation of the particle, and therefore corrects the trapping light beam itself. This method has been tested for defocus but has never been applied to actual holographic setups. In contrast, K. Wulff *et al.* report in [30] a method for correcting aberrations in holographic optical tweezers and show some results of using a Holoeye LC-R 2500 SLM. The basic idea is to add an appropriate hologram to the SLM display, by arbitrary generation of Zernike polynomials characterizing the unknown wavefront distortion, until a tightly focused spot is obtained thus optimizing trap performance. The goodness of the correction is quantified by establishing the mean-square displacement of the trapped beads from their respective trapping centers, which is related to trap stiffness. For the SLM used in their study, K. Wulff *et al.* show that astigmatism correction leads to an improvement in the fidelity of the focused spot. The

impact of this correction on the performance of the optical trap is most noticeable for small particles (0.8 and 2 μm silica microspheres). They also state that any quantifiable impact was difficult to separate from other aberrations such as coma, trefoil, and spherical aberration.

We have previously shown [31] that the beam reflected by our Holoeye LC-R 2500 modulator, placed at 45º with respect to the optical axis, when focused by the microscope objective in a holographic optical tweezers setup forms two lines of light instead of a diffraction-limited spot. We have manually found a phase function that reverses this effect (similar to astigmatism) and eventually corrects the aberration, at least in the central part of the modulator.

In this work, we use a Shack-Hartmann wavefront sensor to measure the distorted wavefront at the SLM plane. The conjugate of this wavefront is then added to the holograms displayed on the SLM to counteract its own curvature and thus compensate the optical aberrations of the system. This process could be fully automated in a closed-loop configuration.

## Experimental setup and procedure

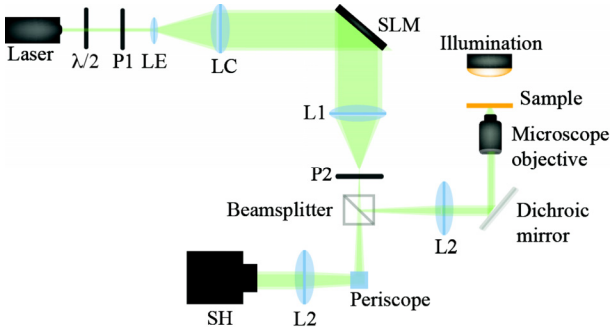


Fig. 1. Experimental setup for holographic optical trapping and correction of SLM optical aberrations (LE: expander lens; LC: collimating lens; P1 and P2: polarizers; SH: Shack-Hartmann wavefront sensor).

Fig. 1 shows the layout that combines holographic optical tweezers with adaptive optics for aberration correction. A continuous wave, $TEM_{00}$ laser beam ($\lambda = 532$ nm) is first expanded and then collimated by lenses LE and LC. A pinhole spatially filters the light at the back focal plane of the expander lens, to ensure clean, Gaussian illumination of the SLM. We used an LCoS reflective SLM (Holoeye LC-R 2500), which has an active area of 19.5x14.6 $mm^2$ and supports DVI-signals with a resolution of 1024x768 pixels (pixel pitch 19 μm, fill factor 93%) [28]. The SLM was tilted 45º with respect to the optical axis [31] and sandwiched between two linear polarizers (P1 and P2) with proper orientations to provide phase-mostly modulation [32,33]. A

beam splitter divides the beam in two: one half enters a commercial microscope to trap microscopic particles, while the other is redirected to a Shack-Hartmann wavefront sensor (SH). In our setup, a Motic AE-31 inverse microscope equipped with an oil-immersion objective (100x, 1.25 NA) was used; the beam was reflected upwards by a dichroic mirror and focused at the sample plane by the objective. Along the other arm, wavefront distortions were measured with a HASO 32 Imagine Optics sensor [35], which has 32x32 microlenses and an aperture of 5x5 $mm^2$. The telescope formed by lenses L1 and L2 provided parallel illumination to the infinity-corrected microscope objective and imaged the SLM onto both the exit pupil of the objective and the wavefront sensor. To make use of its whole active area, the image of the modulator was scaled down to match the size of the objective back aperture (around 3.5 mm in diameter) and, at the same time, it was fitted into the sensor aperture. Considering that the longest side of the modulator was reduced by a factor of $\sqrt{2}$ due to its 45º tilt, a telescope magnification of 0.25 gave an image of the modulator which slightly overfilled the objective pupil and occupied 22x24 sub-apertures of the Shack-Hartmann sensor.

If the SLM is placed at the front focal plane of lens L1, its image is formed at the back focal plane of lens L2. To keep the overall length of the optical system reasonably small, the focal length of lens L2 is $f_{L2}$ = 100 mm and, consequently, $f_{L1}$ = 400 mm. Unfortunately, 100 mm is too short a distance to allow us to divide the two beams after passing through lens L2 and before entering the microscope: a periscope system is required to adapt the heights of the beams to the microscope and the sensor, which is assembled on a rotating stage with micrometric controls to facilitate its alignment. This means that, even if lens L2 is duplicated in both arms of the system and thus contributes to the final wavefront on the sensor, the latter does not actually measure possible misalignments of lens L2 and the objective lens in the optical tweezers path. However, we are mostly concerned here with the predominant aberrations caused by the modulator; we ignore distortions derived from incorrect alignment of the system or from the highly-corrected microscope objective. Further developments would allow us to measure distortions of the trap itself, which would then allow us to correct other aberrations such as the spherical aberration due to refractive index mismatch [8,9].

To correct SLM aberrations, the Shack-Hartmann sensor was set up to receive an incoming wavefront with minimum tilt and defocus. The wavefront aberration was then measured and a conjugated correction phase (modulo $2\pi$) was displayed on the SLM, taking into

account its modulation curve [32,33]. This relates phase modulation with the grey level displayed; as images on the sensor have only 22x24 pixels, grey level values of the remaining pixels of the SLM were computed by interpolation. Next, the residual wavefront error was measured and added to the previous correction; this procedure was repeated iteratively to obtain a minimal aberration, such that, if no other hologram were added to the SLM, a plane wavefront should be achieved. By requiring the beam exiting the SLM to be a plane wave, even if the input illumination is a Gaussian beam, we are somehow also improving trapping efficiency by increasing the energy of high-NA rays compared to low-NA rays.

## Results and discussion

The distorted wavefront received by the Shack Hartmann sensor at the SLM plane is shown in Fig. 2a; it has a peak-to-valley (PV) value of 7.6λ and a root-mean-square (RMS) value of 1.4λ. By applying the procedure described in the previous section, after 9 iterations we obtained the correction hologram shown in Fig. 3, which should give an exit plane wavefront when displayed on the SLM. The residual aberration measured by the sensor is shown in Fig. 2c, for which the PV and RMS deviations are 1.4λ and 0.1λ, respectively. In the holographic optical tweezers setup, only the inscribed circular area highlighted in Fig. 2a and 2c enters the microscope objective, to avoid diffraction through the rectangular active area of the SLM and to maximize the numerical aperture. Then, if we disregard aberrations outside the inscribed round pupil, flatness is improved from 0.8λ RMS (4.7λ PV) to λ/16 RMS (λ/3 PV), yielding a diffraction-limited spot when focused through the objective lens. The Strehl ratios associated with the simulated PSFs before and after compensation (Fig. 2b and 2d) are 0.13 and 0.86, respectively.

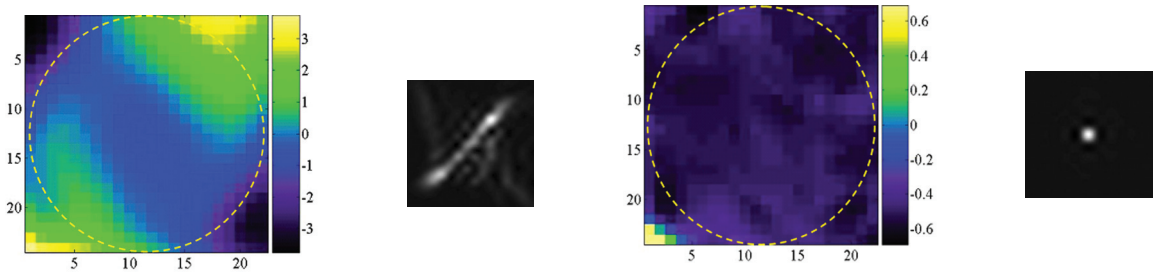


Fig. 2. Wavefront at the SLM plane and the corresponding PSF: (a) and (b) without correction; (c) and (d) after correction.

We believe that residual aberrations close to the edges are mainly due to the spatial non-uniformity of the SLM, meaning that its response actually changes from pixel to pixel; when scaling the conjugated phase into grey-level values, we used a single phase modulation curve, which was measured in a central area of the SLM of about 3 mm in diameter [33], far away from the edges. As pointed out by other authors [18, 22], aberration correction could be improved by using a spatially varying phase response. In fact, our experimental system could be used to determine the local phase modulation in each of the pixels of the wavefront sensor (which corresponds to an SLM area of about 32x32 pixels), by measuring phase changes when each of the 256 grey-level values were displayed on the modulator. A closed-loop configuration would then be desirable to fully automate the process. Moreover, this would allow iterative correction of SLM distortions without previous knowledge of its phase response, just by trial-and-error.

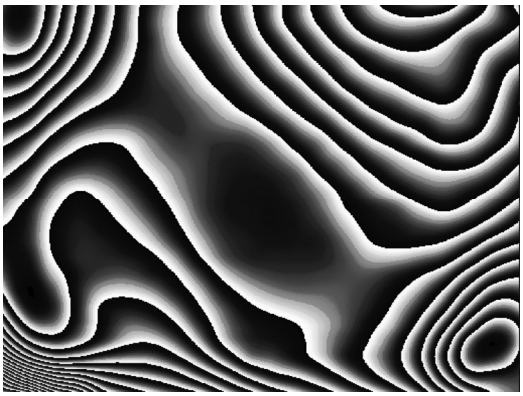

Fig. 3. Hologram displayed on the SLM for self aberration correction.

We compared the quality of the trap before and after correction: the left column of Fig. 4 shows several images of an uncorrected trap for different planes along the optical axis, revealing the lack of symmetry typical of astigmatism (as we will see below when analyzing the aberrations of the system); the circular symmetry of the experimental corrected trap at different planes (right column of Fig. 4) shows the improvement of trap quality after aberration correction. It also proves that the main aberration was indeed due to the SLM and not to misalignment of the optical setup.

Furthermore, we used the corrected trap to stably trap and move a 5 μm polystyrene bead, as shown in Fig. 5. Linear phase patterns were added to the correction hologram of Fig. 3 to displace the trapped particle to the desired position; spherical wavefronts were also used to move

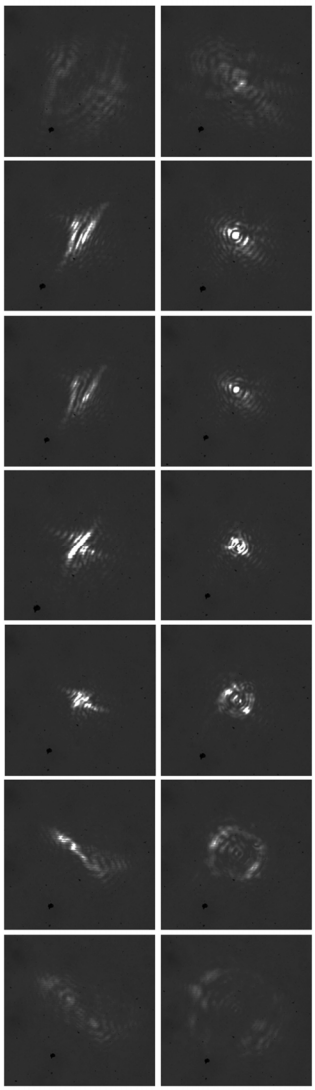

Fig. 4. Images of the experimental trap for different planes along the optical axis, before correction (left column) and after aberration correction (right column). The distance between the top and the bottom plane is around 1 μm.

the sample along the optical axis. We would like to point out here that it was not necessary in our setup to block the central undiffracted beam, which nearly vanished [33].

On the other hand, we further analyzed aberrations of our optical system by decomposing the wavefronts inside the circular pupil in Fig. 2a and 2c by means of Zernike polynomials. We used the first 32 coefficients, as defined in [35]. Table 1 lists the most significant terms, revealing for the distorted wavefront a predominant astigmatism aberration (both third and fifth order) followed by third-order spherical aberration. After correction, all Zernike coefficients were below λ/20.

| Zernike term - Aberration | Zernike coefficient (waves at 532 nm) | |
|---|---|---|
| | Before correction | After correction |
| 4 - Astigmatism at 0º | 0.40 | -0.04 |
| 5 - Astigmatism at 45º | 1.66 | -0.04 |
| 6 - Coma at 0º | 0.04 | 0.00 |
| 7 - Coma at 45º | 0.00 | -0.02 |
| 8 - 3rd order Spherical | -0.42 | 0.00 |
| 9 - Trefoil at 0º | -0.11 | 0.05 |
| 10 - Trefoil at 45º | 0.14 | -0.05 |
| 11 - 5th order Astigmatism at 0º | 0.48 | 0.00 |
| 12 - 5th order Astigmatism at 45º | 0.19 | 0.00 |

Table 1. Zernike coefficients of uncorrected and corrected wavefronts.

Wang *et al.* report in [26] the predominance of low-order defocus and astigmatism for a Hana Microdisplay device. Hart *et al.* compare in [23] the static aberrations of three BNS devices: they all show important defocus and astigmatism, among other aberrations. The same conclusion can be drawn from [18].

In our case, the system was aligned to obtain minimum tilt and defocus, which are therefore not shown in Table 1. This means that the beam onto the sensor is collimated and we are actually correcting any defocus introduced by the SLM by axially displacing lens L2. This procedure is correct as long as lens L2 in the beam entering the microscope is also displaced; in

fact, we think this could even be helpful when aligning the optical tweezers, as we are forcing the beam to be parallel before it enters the microscope objective. Anyway, defocus could be compensated at the end by adjusting the observation and the trapping plane, if necessary. Furthermore, excluding defocus from aberration compensation means measuring a less distorted wavefront with the Shack-Hartmann sensor and displaying a smoother hologram on the SLM, which is desirable.

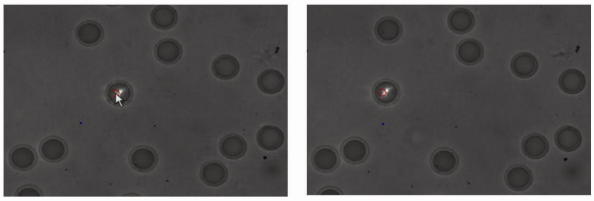

Fig. 5. A 5 μm polystyrene bead was trapped and moved to the left hand side by the corrected optical trap. The laser light was filtered to avoid saturating the images; the red empty circle indicates the trap center.

So far we have seen that aberrations produced by the SLM curvature can be corrected to obtain a diffraction-limited pattern. Ignoring focus effects, an analysis of Zernike coefficients reveals aberration predominantly due to astigmatism, as reported for other LCoS devices. We wonder now whether correction of solely low-order astigmatism would yield acceptable results; this would allow the use of a simplified method in which no wavefront sensor or interferometric setup would be required, and correction could be achieved by adjusting the few parameters that model low-order astigmatism, as we reported in [31]. When considering the whole circular aperture of the SLM (as indicated in Fig. 2), the RMS deviation after astigmatism correction is 0.4λ (1.6λ PV), even in the ideal case in which there was no residual tilt or defocus. We studied the quality of astigmatism correction for smaller apertures: Fig. 6 shows the evolution of the RMS error of corrected wavefronts as the diameter of the aperture, which is normalized to the maximum inscribed pupil, diminishes. We can see that to achieve the commonly accepted diffraction-limited criteria of λ/14 for the RMS value, indicated by a dashed line in the figure, we need to reduce the aperture to around 0.65 times the maximum. The hologram displayed on the SLM for this purpose is shown in Fig. 6b. This means that the non-flatness of our modulator could eventually be compensated this way if a diaphragm is used to ensure that only the central part of the device is illuminated, covering around 40% of its maximum circular aperture or 20% of the rectangular SLM active area. It also explains our previous work [31]: in that case, the

hologram compensated both astigmatism and defocus (lens L2 was not artificially displaced, as it was here) and thus required a larger amount of wave variation.

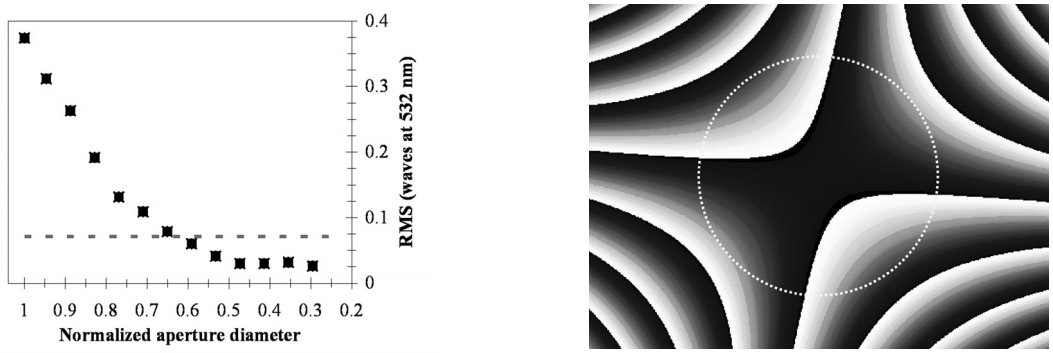


Fig. 6. (a) Residual RMS error after low-order astigmatism correction, as a function of the normalized SLM aperture; diffraction-limited results are obtained for RMS values below the dashed line. (b) Hologram to compensate astigmatism for an aperture indicated by the dashed line.

## Conclusion

In this work, we correct the aberration of an LCoS SLM used in a holographic optical tweezers setup. We measure the distorted wavefront at the SLM plane with a Shack-Hartmann sensor and iteratively compute a compensation phase hologram, which is displayed on the SLM for self correction. RMS deviations improve from 0.8λ to λ/16, ensuring a diffraction-limited trap in the focal plane of the microscope objective, which allows stable trapping and manipulation of microscopic samples. An analysis of Zernike polynomials describing the aberrated wavefront indicates a predominance of astigmatism and third-order spherical aberration. We also demonstrate that correction of low-order astigmatism alone can yield diffraction-limited beams if a central circular aperture of the modulator is considered. A generalization of this conclusion to other LCoS devices would hopefully indicate that aberration can be corrected with no need for interferometric setups or wavefront sensors. In our case, the use of a Shack-Hartmann sensor enables a series of enhancements to be considered in the future, especially if the wavefront detection and SLM addressing work in a closed-loop feedback configuration: the process can then be fully automated and dynamic distortion correction is feasible, even with no previous knowledge of SLM phase response, which could actually be characterized this way. Furthermore, additional phase patterns can be considered to correct for other aberrations, such as misalignment. In optical tweezers, apart from the well-known spherical aberration of the microscope objective due to refractive index mismatch, aberrations derived from the use of a

wavelength of light for which the objective is not corrected and distortions due to non-uniformity of biological samples could be also be compensated for.

## Acknowledgments

We acknowledge Dr. M. Montes-Usategui for many fruitful discussions, E. Pleguezuelos and M. Roth for help and advice with the alignment of the optical system, and F. Gómez-Morales who contributed to the set up of the Shack-Hartmann sensor. This work was funded by the Spanish Ministry of Education and Science, under grants FIS2004-03450 and NAN2004-09348-C04-03.

## References


1. A. Ashkin, J. M. Dziedzic, J. E. Bjorkholm, and S. Chu, "Observation of a single-beam gradient force optical trap for dielectric particles," Opt. Lett. **11**, 288-290 (1986), http://www.opticsinfobase.org/abstract.cfm?URI=ol-11-5-288.
2. M. J. Lang and S. M. Block, "Resource letter: LBOT-1: Laser-based optical tweezers," Am. J. Phys. **71**, 201-215 (2003).
3. M. Reicherter, T. Haist, E. U. Wagemann, and H. J. Tiziani, "Optical particle trapping with computer-generated holograms written on a liquid-crystal display," Opt. Lett. **24**, 608-610 (1999), http://www.opticsinfobase.org/abstract.cfm?URI=ol-24-9-608.
4. J. Liesener, M. Reicherter, T. Haist, and H. J. Tiziani, "Multi-functional optical tweezers using computer-generated holograms," Opt. Commun. **185**, 77-82 (2000).
5. E. R. Dufresne, G. C. Spalding, M. T. Dearing, S. A. Sheets, and D. G. Grier, "Computer-generated holographic optical tweezer arrays," Rev. Sci. Instrum. **72**, 1810-1816 (2001).
6. J. E. Curtis, B. A. Koss, and D. G. Grier, "Dynamic holographic optical tweezers," Opt. Commun. **207**, 169-175 (2002).
7. D. G. Grier, "A revolution in optical manipulation," Nature **424**, 810-816 (2003).
8. O. Muller, M. Schliwa, and H. Felgner, "Calibration of light forces in optical tweezers," Appl. Opt. **34**, 977- (1995), http://www.opticsinfobase.org/abstract.cfm?URI=ao-34-6-977.
9. A. Rohrbach and E. H. K. Stelzer, "Trapping forces, force constants, and potential depths for dielectric spheres in the presence of spherical aberrations," Appl. Opt. **41**, 2494-2507 (2002), http://www.opticsinfobase.org/abstract.cfm?URI=ao-41-13-2494.
10. T. Ota, T. Sugiura, S. Kawata, M. J. Booth, M. A. A. Neil, R. Juskaitis, and T. Wilson, "Enhancement of laser trapping force by spherical aberration correction using a deformable mirror," Jpn. J. Appl. Phys. **42**, L701-L703 (2003).
11. E. Theofanidou, L. Wilson, W. J. Hossack, and J. Arlt, "Spherical aberration correction for optical tweezers," Opt. Commun. **236**, 145-150 (2004).
12. K. Ladavac and D. Grier, "Microoptomechanical pumps assembled and driven by holographic optical vortex arrays," Opt. Express **12**, 1144-1149 (2004), http://www.opticsinfobase.org/abstract.cfm?URI=oe-12-6-1144.

13. Y. Roichman, A. Waldron, E. Gardel, and D. G. Grier, "Optical traps with geometric aberrations," Appl. Opt. **45**, 3425-3429 (2006), http://www.opticsinfobase.org/abstract.cfm?URI=ao-45-15-3425.
14. A. Jesacher, A. Schwaighofer, S. Fürhapter, C. Maurer, S. Bernet, and M. Ritsch-Marte, "Wavefront correction of spatial light modulators using an optical vortex image," Opt. Express **15**, 5801-5808 (2007), http://www.opticsinfobase.org/abstract.cfm?URI=oe-15-9-5801.
15. G. D. Love, "Wave-front correction and production of Zernike modes with a liquid-crystal spatial light modulator," Appl. Opt. **36**, 1517-1520 (1997), http://www.opticsinfobase.org/abstract.cfm?URI=ao-36-7-1517.
16. J. Liesener, M. Reicherter, and H. J. Tiziani, "Determination and compensation of aberrations using SLMs," Opt. Commun. **233**, 161-166 (2004).
17. Q. Mu, Z. Cao, L. Hu, D. Li, and L. Xuan, "An adaptive optics imaging system based on a high-resolution liquid crystal on silicon device," Opt. Express **14**, 8013-8018 (2006), http://www.opticsinfobase.org/abstract.cfm?URI=oe-14-18-8013.
18. J. D. Schmidt, M. E. Goda, and B. D. Duncan, "Aberration production using a high-resolution liquid-crystal spatial light modulator," Appl. Opt. **46**, 2423-2433 (2007), http://www.opticsinfobase.org/abstract.cfm?URI=ao-46-13-2423.
19. S. T. Wu and D. K. Yang, *Reflective Liquid Crystal Displays* (John Wiley & Sons Inc., Chichester, 2001).
20. K. Seunarine, D. W. Calton, I. Underwood, J. T. M. Stevenson, A. M. Gundlach, and M. Begbie, “Techniques to improve the flatness of reflective micro-optical arrays,” Sens. Actuat. A **78**, 18-27 (1999).
21. J. Harriman, A. Linnenberger, and S. Serati, "Improving spatial light modulator performance through phase compensation," Proc. SPIE **5553**, 58-67 (2004).
22. J. Otón, P. Ambs, M. S. Millán, and E. Pérez-Cabré, "Multipoint phase calibration for improved compensation of inherent wavefront distortion in parallel aligned liquid crystal on silicon displays," Appl. Opt. **46**, 5667-5679 (2007), http://www.opticsinfobase.org/abstract.cfm?URI=ao-46-23-5667.

23. N. Hart, M.C. Roggemann, A. Sergeyev, and T.J. Schulz, “Characterizing static aberrations in liquid crystal spatial light modulators using phase retrieval,” Opt. Eng. **46**, 086601 (2007).
24. http://www.bnonlinear.com/.
25. X. Wang, B. Wang, J. Pouch, F. Miranda, J. E Anderson, and P. J Bos, “Performance evaluation of a liquid crystal-on-silicon spatial light modulator,” Opt. Eng. **43**, 2769-2774 (2004).
26. X. Wang, B. Wang, P. J. Bos, J. E. Anderson, J. J. Pouch, and F. A. Miranda, “Finite-difference time-domain simulation of a liquid-crystal optical phased array,” J. Opt. Soc. Am. A **22**, 346-354 (2005).
27. http://www.hanaoh.com/.
28. http://www.holoeye.com/.
29. M. Reicherter, W. Gorski, T. Haist, and W. Osten, “Dynamic correction of aberrations in microscopic imaging systems using an artificial point source,” Proc. SPIE **5462**, 68-78 (2004).
30. K. D. Wulff, D. G. Cole, R. L. Clark, R. Di Leonardo, J. Leach, J. Cooper, G. Gibson, and M. J. Padgett, "Aberration correction in holographic optical tweezers," Opt. Express **14**, 4169-4174 (2006), http://www.opticsinfobase.org/abstract.cfm?URI=oe-14-9-4169.
31. E. Martín-Badosa, M. Montes-Usategui, A. Carnicer, J. Andilla, E. Pleguezuelos, and I. Juvells, “Design strategies for optimizing holographic optical tweezers set-ups,” J. Opt. A: Pure Appl. Opt. **9**, S267-S277 (2007).
32. E. Martín-Badosa, A. Carnicer, I. Juvells, and S. Vallmitjana, "Complex modulation characterization of liquid crystal devices by interferometric data correlation," Meas. Sci. Technol. **8**, 764-772 (1997).
33. J. Andilla, S. Vallmitjana, and E. Martín-Badosa, “Prediction of phase-mostly modulation for holographic optical tweezers,” Opt. Commun. **281**, 3786–3791 (2008).
34. http://www.imagine-optic.com/.
35. R. J. Noll, "Zernike polynomials and atmospheric turbulence", J. Opt. Soc. Am. **66**, 207-211 (1976).

# Appendix F

## Holographic optical manipulation of membranous structures in living NG-108 cells

Sent to

Journal of Optics A: Pure and Applied Optics
Nov. 2008

# Holographic optical manipulation of motor-driven membranous structures in living NG-108 cells

**A Farré-Flaquer, C López, J Andilla, E Martín-Badosa and M Montes-Usategui**

Grup de Recerca en Òptica Física-GROF, Departament de Física Aplicada i Òptica
Universitat de Barcelona, Martí i Franquès 1, Barcelona 08028, Spain

E-mail: mario_montes@ub.edu

**Abstract.** Optical tweezers experiments have partially unveiled the mechanical properties of processive motor proteins while driving polystyrene or silica microbeads *in vitro*. However, the set of forces underlying the more complex transport mechanisms in living samples remain poorly understood. Several works have shown that optical tweezers are capable of trapping vesicles and organelles in the cytoplasm of living cells, so as to be used as handles to mechanically interact with engaged (active) motors, or other components regulating the transport. This may ultimately allow exploring the mechanics of this trafficking mechanism *in vivo*. Unfortunately, little information has been provided about the trapping of motor-driven membranous structures using laser traps. Here we show the advantages of using holographic real-time optical tweezers for such a purpose in living NG-108 cells, and we also discuss the need for an interactive trapping system to perform the experiments.

## 1. Introduction

Optical tweezers are currently used in different molecular biology experiments [1]. A highly focused infrared laser beam enables the manipulation of biological samples and the measurement of the forces involved in many relevant molecular processes [2]. Through this biophotonic tool, results of primary importance have been obtained, such as information on the elastic properties of DNA molecules [3], precise values of the basic mechanical properties of the RNA polymerase [4], or a detailed picture of the mechanism by which bacteriophage $\phi$29 infects bacteria [5]. Its non-invasive behavior confers this technique a suitable feature for *in vivo* experiments within living cells. One of the subjects that has notably leaped forward concerns the so-called intracellular transport.

Both anterograde and retrograde intracellular transports mediate many important cellular processes in living neurons and other motile cells such as the NG-108 cells that we use in this study. The disruption of this trafficking mechanism may eventually collapse the main functions of the cell, and seems connected to the appearance of neurodegenerative diseases [6]. Specifically, transport disorders associated with the overexpression of the microtubule-associated protein (MAP) tau, which inhibits the engagement of plus-end-directed motor proteins, appear to play an important role in Alzheimer [7]. Vesicle trafficking disruptions seem to be also involved in Huntington's chorea and amyotrophic lateral sclerosis [6].

The cytoskeleton is the cellular component governing vesicle trafficking in eukaryotic cells. Different enzymatic motor proteins drive cargos along the crowded branched networks of cytoskeletal filaments by means of the chemical energy obtained from the hydrolysis of ATP molecules. Working coordinately with other accessory proteins, they constitute an extremely complex mechanism by which the cellular components are packaged in small vesicles and transported between inner and peripheral regions.

The mechanical and chemical processes underlying this mechanism have been extensively studied *in vitro*. Optical tweezers experiments, in particular, have provided many important results of the fundamental molecular processes involved in transport. The force exerted by the polymerization of the cytoskeletal filaments, as well as their stiffness [8, 9], or the mechanochemical processes that confer motor proteins the ability to sequentially bind and detach from the filaments [10, 11] are just a few examples.

These experiments generally provide a simplified picture of vesicle trafficking. They mainly focus on the properties of processive motors, thus avoiding the complex mechanical interplay arising between the cargo and the cytoskeletal and accessory proteins. However, these secondary actors also promote cargo transport in living cells and might play a fundamental role in the regulation of the actual mechanism *in vivo*. Specifically, mechanical effects derived from the presence of recruiting proteins increasing the number of motors moving the cargo, or the tug-of-war between actin- and microtubule-based motors are known to modify fast axonal transport [12]. It has been suggested that these additional processes partially governing intracellular trafficking could be responsible for the regulation of the whole mechanism.

Unfortunately, although optical tweezers are a powerful technique to study these molecular processes, they still exhibit some limitations to work within living cells. A robust calibration method to measure forces in an optically nonhomogeneous medium, such as the cytoplasm of the cell [13], is not currently available. In the past decade, a few isolated studies showed several ways to obtain quantitative data within living samples [14, 15]. However, they are not suitable because either it is difficult to combine them with advanced microscopy techniques (e.g., phase contrast microscopy, fluorescence, etc.) to observe the cells, or they lack accuracy.

Despite the sparseness of optical tweezers results *in vivo* because of experimental difficulties, there exists an increasing interest in the use of such quantitative techniques to unveil the underlying processes in vesicle trafficking. Recently, several optical trapping experiments demonstrated the manipulation of lipid granules in living cells and contributed with new force *in vivo* calibration methods [16–18]. Jointly with earlier results [19], they have provided important information about trapping free-floating vesicles. Nevertheless, these results refer only to vesicles diffusing free, so the requirements to mechanically interact with motor-driven membranous structures still remain unclear. Although its feasibility is known [14, 20], few details have been given and there is almost no available information about similar results. In these studies, no advanced manipulation interface seems to have been used.

Here, we pursue showing the advantages of using an optimized, interactive, holographic tweezers system for such a purpose. Unlike what happens with free-vesicles, which can be as large as $1\,\mu m$ in size, in our experiments, the typical diameter for motor-driven structures is around $300\,nm$. So, on the one hand, an aberration-free optical system is needed to stably trap such tiny particles. Moreover, motor-driven cargos exhibit a quick intermittent movement along cytoskeletal filaments: sometimes moving forward, others traveling backward and part of the time remaining stopped. Vesicles are propelled simultaneously by different fast processive motors (speed $\sim 1\mu m/s$) moving long distances, up to $10\,\mu m$ [12]. Thus, on the other hand, the use of dynamic tweezers to create and move the trap rapidly may be very convenient.

The holographic technology we have developed provides a powerful tool to quickly create, move and remove traps [21–23], making the blocking and manipulation of driven vesicles feasible. As we will discuss in section 3, holographic technology exhibits some advantages compared to other dynamic devices such as acousto-optic deflectors (AODs).

## 2. Experimental setup and methods

The optical setup used in the experiments is shown in figures 1 and 2. An $Nd:YVO_4$ infrared laser ($1064\,nm$) is located on an auxiliary shelf below the optical table to avoid noise from its cooling fans. The beam is brought to the desired traveling height by means of a periscope system (P).

A half-wave plate (HWP) provides the right polarization to the beam incident on the spatial light modulator (SLM, Hamamatsu X10468-03), which generates steerable

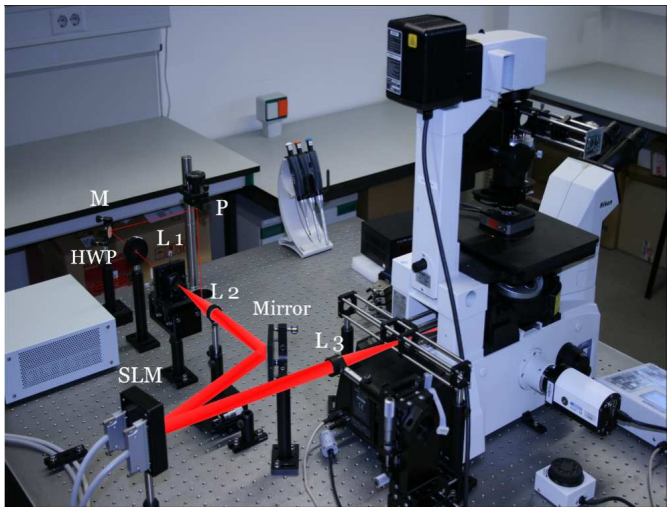


**Figure 1.** General view of the optical setup used in the experiments. (P: periscope, M: mirror, HWP: half-wave plate, L1-L4: lenses, SLM: spatial light modulator).

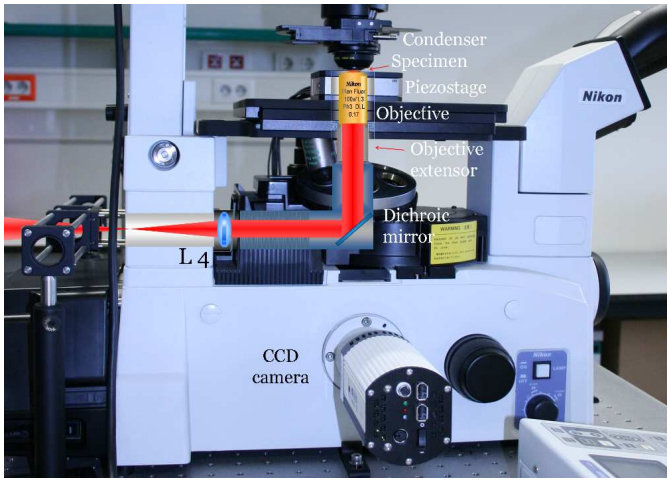


**Figure 2.** Detailed laser pathway inside the microscope.

holographic traps. Two sets of telescopes (lenses L1 and L2, and L3 and L4) allow us to adjust the beam width to the size of the SLM screen and to overfill the entrance pupil of the objective in which we generate the image of the modulator [22]. We take advantage of the objective lens (Nikon Plan Fluor 100x 1.3 NA, oil-immersion, phase contrast) of the microscope (Nikon, Eclipse TE-2000E) to tightly focus the laser beam on the sample and to simultaneously observe the cells with a CCD camera (QImaging, QICAM). A dichroic mirror inserted in between, before the objective lens, redirects the beam so the same path can be used for both the laser and the illumination light coming from the condenser. The light passes through the mirror and reaches the CCD camera at the bottom of the microscope. Finally, the objective focuses the laser on a tiny spot at the specimen plane to generate the optical trap. By means of a user-friendly software we can dynamically create, move and remove traps to perform the experiments

conveniently [23].

Estimation of the size of trapped subcellular structures is desirable for our experiments, since this is an important characteristic of vesicles, which are larger or smaller depending on the contained components. We determined the relation between the dimension of the sample and the corresponding pixel count from the magnification (100x) and the size of the pixels ($4.65\,\mu m$) of the CCD camera used to observe the sample. The apparent size of trapped particles was, then, computed by applying the scale factor $m = 4.65/100 = 0.0465\,\mu m/pix$.

Cell culture

The differentiated type of neuroblastoma X glioma hybrid cell line, NG108, has been widely used in the study of neural function and presents an easily visible vesicular trafficking under conventional phase contrast microscopy.

NG108 cells (provided by Dr. T. Betz, University of Leipzig) were grown in a culture medium containing 90% Dulbecco's modified Eagle's medium (DMEM), supplemented by 10% Fetal Calf Serum, 1% $100\,U/ml$ Penicilling/Streptomycin and 1% 1M HEPES yielding 10 mM concentration. The cultures were maintained at 37 °C in a humidified atmosphere containing 95% air and 5% $CO_2$. The medium was replaced every 2 days.

For optical manipulation, cells were plated onto a laminin-coated chamber ($40\,\mu g/ml$, L2020 Sigma Aldrich) in order to stimulate neurite outgrowth, cell differentiation and to promote cell attachment. Optimal cell density is attained by transferring 1500 cells per chamber.

## 3. Results and discussion

Optical tweezers experiments exploring cargo transport *in vitro* generally focus on the study of the mechanical properties of single kinesin or dynein motors under well-controlled conditions, using a silica or polystyrene bead as a handle. However, the actual mechanism in living cells takes place in an extremely noisy and crowded environment in which several motors, as well as many other often overlooked proteins, mediate the transport simultaneously.

Several papers recently showed that laser traps allow the manipulation of vesicles diffusing freely within living samples [17–19]. Our goal consists of expanding these trapping experiments to membranous structures propelled along cytoskeletal filaments by fast kinesin and dynein proteins. Here, we show the advantages of using holographic tweezers to trap these motor-driven vesicles and organelles in the cytosol of living NG-108 cells (fig. 3). This is important because it may allow the study, in subsequent experiments, of the mechanics of vesicle trafficking *in vivo*. Using the trapped cargo as a sensing probe, force measurements [14–16] could disclose which components in the cytoplasm mechanically interact with this subcellular structure and thus are capable of regulating its transport. For example, the mean number of active motors propelling

the cargo, and how they work together when competing with each other [12] might be studied. Also, the effect of the polymerization and depolymerization of cytoskeletal filaments or other cellular structures perturbing the movement may be determined.

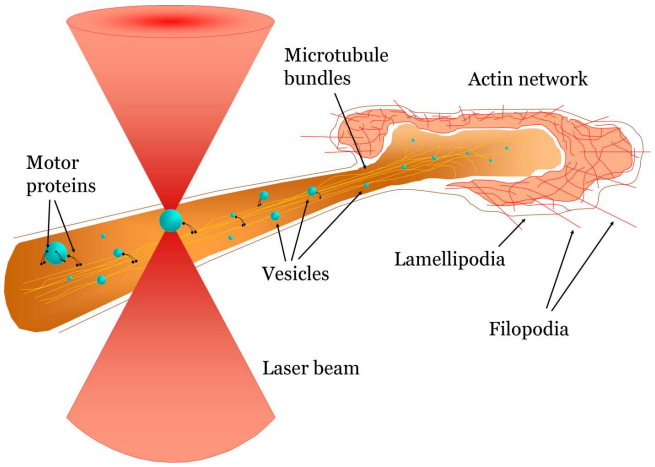


**Figure 3.** Cartoon of the experimental procedure. The infrared laser is used to trap vesicles within living NG-108 cells.

Fast axonal transport is a process in which loads are moved at high speed, up to $1 - 2\,\mu m/s$. It is, hence, natural the use of dynamic tweezers capable of being moved rapidly to follow the particles. There are several experimental techniques that guarantee such requirements: acousto-optic deflectors are probably the most common devices for this purpose, but holographic tweezers provide some advantages that led us to choose this solution [23]. The powerful features that this technology exhibits are promoting an increasing development of important optical applications [24]. Specifically, they allow to move the vesicle or organelle not just on the sample plane as happens with AODs, but also in the axial direction, to get a complete picture of the interactions between the cargo and the surrounding proteins. Also non-gaussian beams might be generated such as size-selective traps [25], which could be useful in certain cases to avoid trapping other vesicles. Finally, holography could be used to compensate for the aberrations of the laser beam due to cell shape irregularities, to the varying cytosol index of refraction, or to the optical setup itself.

Decreased trap stiffness due to optical aberrations appears, for example, when a trap works several microns above the coverslip, because of the distortions produced by the oil-immersion objective. This can seriously affect the trapping of vesicles when moving deep into the cell. Fortunately, contrary to the non-holographic tweezers case, aberrations can be compensated for by modifying the holograms used to generate the trap [26]. This is particularly relevant here because the maximum force applied *in vivo* is almost halved with respect to *in vitro* experiments, since the vesicle refractive index ($n \sim 1.52$) is close to that of the surrounding medium ($n_m \sim 1.39$) [19]. Therefore, all those aberrations affecting the elastic constant of the trap should be corrected in order

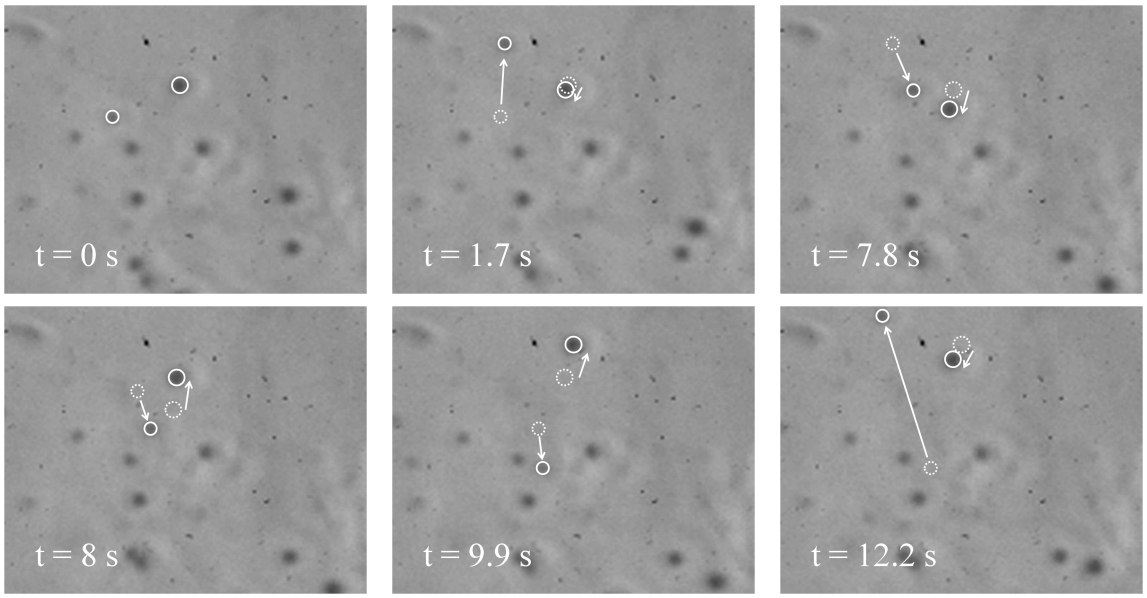


**Figure 4.** Sequence of micro-vesicles moving around the cytosol

to generate large forces.


**Figure 5.** Manipulation of a 770 $nm$ subcellular structure (endosome, lysosome, ...) near the nucleus of an NG-108 cell (Media 1). The arrow indicates the position of the vesicle that is moved by means of the holographic trap. Scale bar, 3 $\mu m$.

We were able to manipulate organelles in living NG-108 cells using the holographic system although in a somewhat unpredictable way, a common difficulty when dealing with biological samples. In a first series of experiments, we immobilized free-floating particles that moved at low speeds by mere thermal agitation. Figure 5 shows a 770 $nm$ membranous structure near the cell nucleus that was trapped and interactively moved using the software. These vesicles seemed often surrounded by stiff filamentous networks that confined their movement into small regions. We could easily move them until

reaching the limits of these inner compartments.

Although more difficult, manipulation of long-directed-driven cargos was also possible. By using the laser, we were able to block single-vesicle transport along a neurite. Specifically, with our holographic system, we easily performed experiments similar to those carried out, independently, by A. Ashkin et al. [14] and M. A. Welte et al. [20], in which they measured the stall forces of motor proteins in living giant amoeba *Reticulomyxa* and in *Drosophila* cells. Grabbing organelles and holding them against the pulling forces allowed us to interact with the engaged motors.

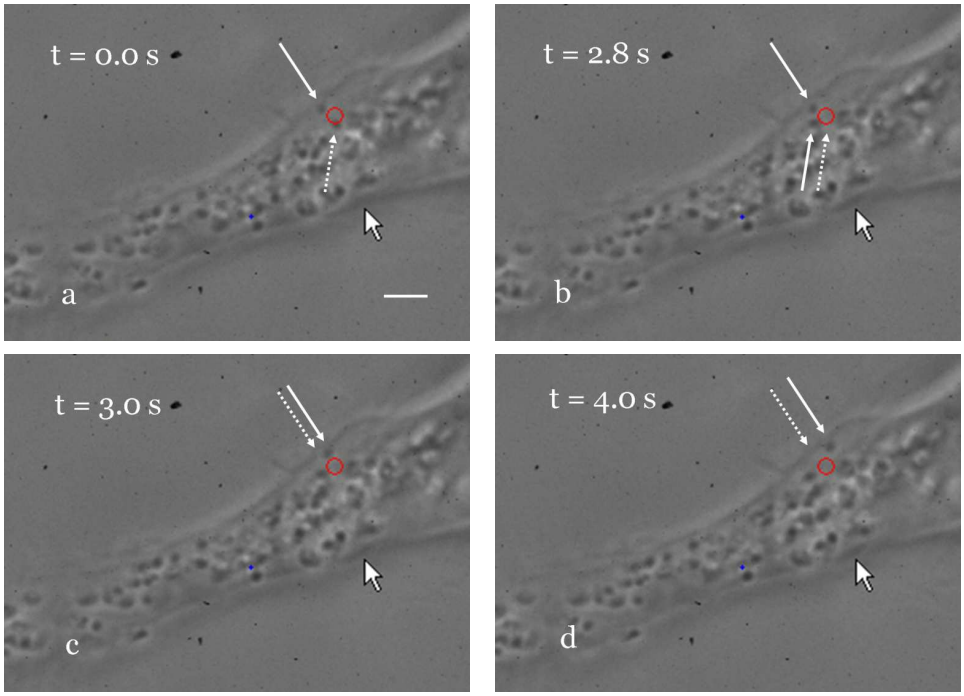


**Figure 6.** (a) A solid-line arrow shows a 270 $nm$ stalled vesicle. The position of the holographic trap lies close to the red circle. On the other hand, a second freely-moving vesicle is also shown (dotted arrow). (b) After almost 3 seconds this latter vesicle has been transported $\sim 1\,\mu m$ away from its initial position, whereas the trapped vesicle remains at the same point. (c) During these 3 seconds the power of the laser beam was reduced until the motor was able to overcome the force from the trap. (d) Just one second later the vesicle has been transported almost $1\,\mu m$. Considering that the growth cone is on the left side of the image, the motor driving the cargo must be a cytoplasmic dynein since we are working in a microtubule rich area (Media 2). Scale bar, $2\,\mu m$.

The trapping of driven vesicles is further complicated by their small size ($200 - 400\,nm$). A well corrected optical system was necessary for interacting with such tiny particles. Figure 6 shows one of these experiments in which a $270\,nm$ vesicle was immobilized using $80\,mW$ at the sample plane. The laser power was, then, continuously reduced until the force generated by the motor was larger than that exerted by the light, at $45\,mW$. At that point, the vesicle escaped from the trap and carried on with

its path. The motor propelling the cargo was presumably a cytoplasmic dynein, since the movement was directed toward the microtubule minus-end [27]. Transport always seemed to resume normally, thus, motors were believed not to be altered by the laser.

The same procedure was repeated on different particles, yet we were not able to stop plus-end-directed transport mediated by kinesins (results not shown). To ensure that the load was effectively applied on motor proteins, we estimated the forces involved in the vesicle movement. Ashkin et al. [14] came up with an approximate force calibration method suitable for experiments in living cells, based on the linear relation between the force and the laser power. We used Ashkin's force calibration data to estimate the trapping force in the previous experiment, exactly when the motor overcomes the opposing action of the laser at $45\,mW$. Their result, $1\,mW$ corresponding to a force of $\sim 0.041\,pN$ on a $320\,nm$ mitochondria, can be easily adapted to our experimental conditions. This leads to a trapping force of $\sim 1.3\,pN$, which is very similar to the dynein stall force *in vitro*, $F_{stall} = 1.1\,pN$ [10], thus supporting the fact that the cargo was driven by a cytoplasmic dynein along a tubulin filament. On the other hand, the maximum laser power that we could reach with our experimental setup, $80\,mW$, corresponds to a force of $\sim 2.3\,pN$. This means insufficient laser power was responsible for the negative trapping experiments with kinesins, since their stall force is larger than that of dyneins, reaching a value of over $6\,pN$. Finally, the laser did not seem to cause any damage on the living cells after a few hours performing the experiments.

## 4. Conclusion

We have discussed the requirement of using dynamic optical tweezers capable of quickly generating traps for *in vivo* vesicle trafficking experiments. Specifically, we have assessed the convenience of using holographic optical tweezers in order to block single-vesicle transport. This is a powerful technology that may provide some advantages with respect to other beam-steering techniques in such experiments. To this effect, vesicles lying free in the cytosol of NG-108 cells were moved to ensure that we were able to interact with these small particles, and, afterwards, dynein-driven cargos moving along neurite microtubule bundles were blocked. In the whole set of experiments, the point-and-click capabilities of our system were instrumental for dealing with these moving particles.

## 5. Acknowledgments

We would like to thank M. Roth for her help with the experimental setup, T. Betz for providing the cell line used in the experiments, and G. Egea for fruitful discussions about the biological content. This work has been funded by the Spanish Ministry of Education and Science, under grants FIS2007-65880 and NAN2004-09348-C04-03.

## References


[1] Lang M J and Block S M 2003 Resource Letter: LBOT-1: Laser-based optical tweezers *Am. J. Phys.* **71** 201–215

[2] Ashkin A, Dziedzic J M, Bjorkholm J E and Chu S 1986 Observation of a single-beam gradient force optical trap for dielectric particles *Opt. Lett.* **11** 288–290 http://ol.osa.org/abstract.cfm?uri=ol-11-5-288

[3] Smith S B, Cui Y and Bustamante C 1996 Overstretching B-DNA: The Elastic Response of Individual Double-Stranded and Single-Stranded DNA Molecules *Science* **271** 795–799 http://www.sciencemag.org/cgi/content/abstract/271/5250/795

[4] Shaevitz J, Abbondanzieri E, Landick R and Block S M 2003 Backtracking by single RNA polymerase molecules observed at near-base-pair resolution *Nature* **426** 684–687 http://www.nature.com/nature/journal/v426/n6967/abs/nature02191.html

[5] Smith D E, Tans S J, Smith S B, Grimes S, Anderson D L and Bustamante C 2001 The Bacteriophage $\phi$29 Portal Motor can Package DNA Against a Large Internal Force *Nature* **413** 748–752 http://www.nature.com/nature/journal/v413/n6857/abs/413748a0.html

[6] Duncan J E and Goldstein L S B 2006 The Genetics of Axonal Transport and Axonal Transport Disorders *PLOS Gen.* **2** 1275–1284 http://www.plosgenetics.org/article/info:doi/10.1371/journal.pgen.0020124

[7] Ebneth A, Godemann R, Stamer K, Illenberger S, Trinczek B, Mandelkow E M and Mandelkow E 1998 Overexpresion of Tau Protein Inhibits Kinesin-dependent Trafficking of Vesicles, Mitochondria, and Endoplasmic Reticulum: Implications for Alzheimer's Disease *J. Cell Biol.* **143** 777–794 http://www.jcb.org/cgi/content/abstract/143/3/777

[8] Dogterom M and Yurke B 1997 Measurement of the Force-Velocity Relation for Growing Microtubules *Science* **278** 856–860 http://www.sciencemag.org/cgi/content/abstract/278/5339/856

[9] Footer M J, Kerssemakers J W J, Theriot J A and Dogterom M 2007 Direct measurement of force generation by actin filament polymerization using an optical trap *Proc. Natl. Acad. Sci. USA* **104** 2181–2186 http://www.pnas.org/content/104/7/2181.abstract

[10] Mallik R, Carter B C, Lex S A, King S J and Gross S P 2004 Cytoplasmic dynein functions as a gear in response to load *Nature* **427** 649–652 http://www.nature.com/nature/journal/v427/n6975/abs/nature02293.html

[11] Svoboda K, Schmidt C F, Schnapp B J and Block S M 1993 Direct observation of kinesin stepping by optical trapping interferometry *Nature* **365** 721–727 http://www.nature.com/nature/journal/v365/n6448/abs/365721a0.html

[12] Gross S P, Vershinin M and Shubeita G T 2007 Cargo Transport: Two Motors Are Sometimes Better Than One *Curr. Biol.* **17** 478–486 http://www.current-biology.com/content/article/abstract?uid=PIIS0960982207012663

[13] Rappaz B, Charrière F, Depeursinge C, Magistretti P J and Marquet P 2008 Simultaneous cell morphometry and refractive index measurement with dual-wavelength digital holographic microscopy and dye-enhanced dispersion of perfusion medium *Opt. Lett.* **33** 744–746 http://ol.osa.org/abstract.cfm?uri=ol-33-7-744

[14] Ashkin A, Schutze K, Dziedzic J M, Euteneuer U and Schliwa M 1990 Force generation of organelle transport measured in vivo by an infrared laser trap *Nature* **348** 346–348 http://www.nature.com/nature/journal/v348/n6299/abs/348346a0.html

[15] Smith S B, Cui Y and Bustamante C 2003 Optical-Trap Force Transducer That Operates by Direct Measurement of Light Momentum *Methods Enzymol.* **361** 134–162

[16] Fischer M and Berg-Sørensen K 2007 Calibration of trapping force and response function of optical tweezers in viscoelastic media *J. Opt. A: Pure Appl. Opt.* **9** S239–S250 http://iopscience.iop.org/1464-4258/9/8/S18/pdf?ejredirect=.iopscience

[17] Sacconi L, Tolić-Nørrelykke I M, Stringari C, Antolini R and Pavone F S 2005 Optical micromanipulation inside yeast cells *Appl. Opt.* **44** 2001–2007 http://ao.osa.org/abstract.cfm?uri=ao-

44-11-2001

[18] Tolić-Nørrelykke I M, Munteanu E L, Thon G, Oddershede L and Berg-Sørensen K 2004 Anomalous diffusion in living yeast cells *Phys. Rev. Lett.* **93** 078102 http://prola.aps.org/abstract/PRL/v93/i7/e078102

[19] Gross S P 2003 Application of Optical Traps In Vivo *Methods Enzymol.* **361** 162–174

[20] Welte M A, Gross S P, Postner M, Block S M and Wieschaus E F 1998 Developmental Regulation of Vesicle Transport in Drosophila Embryos: Forces and Kinetics *Cell* **92** 547–557 http://www.cell.com/content/article/abstract?uid=PIIS0092867400809472

[21] Montes-Usategui M, Pleguezuelos E, Andilla J and Martín-Badosa E 2006 Fast generation of holographic optical tweezers by random mask encoding of Fourier components *Opt. Express* **14** 2101–2107 http://www.opticsinfobase.org/abstract.cfm?URI=oe-14-6-2101

[22] Martín-Badosa E, Montes-Usategui M, Carnicer A, Andilla J, Pleguezuelos E and Juvells I 2007 Design strategies for optimizing holographic optical tweezers set-ups *J. Opt. A: Pure Appl. Opt.* **9** 267–277 http://www.iop.org/EJ/abstract/1464-4258/9/8/S22

[23] Pleguezuelos E, Carnicer A, Andilla J, Martín-Badosa E and Montes-Usategui M 2007 HoloTrap: Interactive hologram design for multiple dynamic optical trapping *Comput. Phys. Commun.* **176** 701–709

[24] Grier D G 2003 A revolution in optical manipulation *Nature* **424** 21–27 http://www.nature.com/nphoton/journal/vsample/nsample/full/nature01935.html

[25] Jesacher A, Furhapter S, Bernet S and Ritsch-Marte M 2004 Size selective trapping with optical "cogwheel" tweezers *Opt. Express* **12** 4129–4135 http://www.opticsinfobase.org/abstract.cfm?URI=oe-12-17-4129

[26] Wulff K D, Cole D G, Clark R L, DiLeonardo R, Leach J, Cooper J, Gibson G and Padgett M J 2006 Aberration correction in holographic optical tweezers *Opt. Express* **14** 4169–4174 http://www.opticsinfobase.org/abstract.cfm?URI=oe-14-9-4169

[27] Hirokawa N 1998 Kinesin and Dynein Superfamily Proteins and the Mechanism of Organelle Transport *Science* **279** 519–526 http://www.sciencemag.org/cgi/content/full/279/5350/519?ijkey=RTBl1yxfCaRzU

# Appendix G

## Design of a low-cost, interactive, holographic optical tweezers system

Conference Proceeding, published in

Proceedings of SPIE
Vol.: 6326, 63262Q, Sep. 2006

# Design of a low-cost, interactive, holographic optical tweezers system

E. Pleguezuelos, J. Andilla, A. Carnicer, E. Martín-Badosa,
S. Vallmitjana and M. Montes-Usategui

Universitat de Barcelona, Departament de Física Aplicada i Òptica,
Martí i Franquès 1, 08028 Barcelona, Spain

## ABSTRACT

The paper describes the design of an inexpensive holographic optical tweezers setup. The setup is accompanied by software that allows real-time manipulation of the sample and takes into account the experimental features of the setup, such as aberration correction and LCD modulation. The LCD, a HoloEye LCR-2500, is the physical support of the holograms, which are calculated using the fast random binary mask algorithm. The real-time software achieves 12 fps at full LCD resolution (including aberration correction and modulation) when run on a Pentium IV HT, 3.2 GHz computer.

**Keywords:** Optical Trapping, Digital holography

## 1. INTRODUCTION

This paper describes the design procedure for a real-time, reconfigurable, holographic optical tweezers setup. The device has been built using low-cost components, for a total amount not in excess of 10,000 € (about $12,500). The experimental set-up is based on a Motic AE31 inverted microscope using a 100x N.A. 1.25 objective, illuminated by a 532 nm 120 mW Viasho laser. The sample plane can be observed with a CCD camera through the dichroic mirror.

A HoloEye LC-R 2500 reflective SLM is been used to display the holograms that generate the desired trap pattern at the focal plane of the objective lens. The modulator is placed at 45° with respect to the incident beam, which allows better control of the different SLM operating modes. The device has been fully characterized in order to obtain an almost phase-only configuration that optimizes light efficiency. For a wavelength of 532 nm, we have found a phase modulation of $2\pi$, where the amplitude is almost constant. We have observed that the traps show astigmatic behavior when focused at different planes. This may be caused by the SLM panel not being completely flat and having a small optical power. This problem can be overcome by adding the proper phase pattern to all the holograms.

The traps are controlled by means of a fast algorithm that directly gives the desired hologram with straightforward computations. The algorithm can also be used to modify any existing hologram very quickly and it does not produce ghost traps or replicas. The control software is implemented in Java and is capable of displaying 1024×768 pixel holograms at an average rate of 12 Hz (including aberration correction of the SLM and compensation of the operating curve nonlinearities) when run on a Pentium IV HT, 3.2 GHz computer.

## 2. THE OPTICAL SETUP

In this section we describe the design of the experimental setup. The setup is shown in Figure 1(a). It is based on a Motic AE31 inverted microscope using a 100x N.A. 1.25 objective. This microscope has been modified to introduce the laser beam through the epifluorescence port. The laser is a continuous-wave, frequency-doubled Nd:$YVO_4$ laser of 120 mW from Viasho Technology ($\lambda = 512$ nm).

A pinhole filters high frequency terms in the Fourier plane of the expander lens (8mm of focal length) and the beam is collimated with a 75 mm focal lens. Taking into account that the beam waist is 0.9 mm wide and the

E.P. E-mail: encarni.pleguezuelos@ub.edu

Optical Trapping and Optical Micromanipulation III, edited by Kishan Dholakia, Gabriel C. Spalding,
Proc. of SPIE Vol. 6326, 63262Q, (2006) · 0277-786X/06/$15 · doi: 10.1117/12.680593

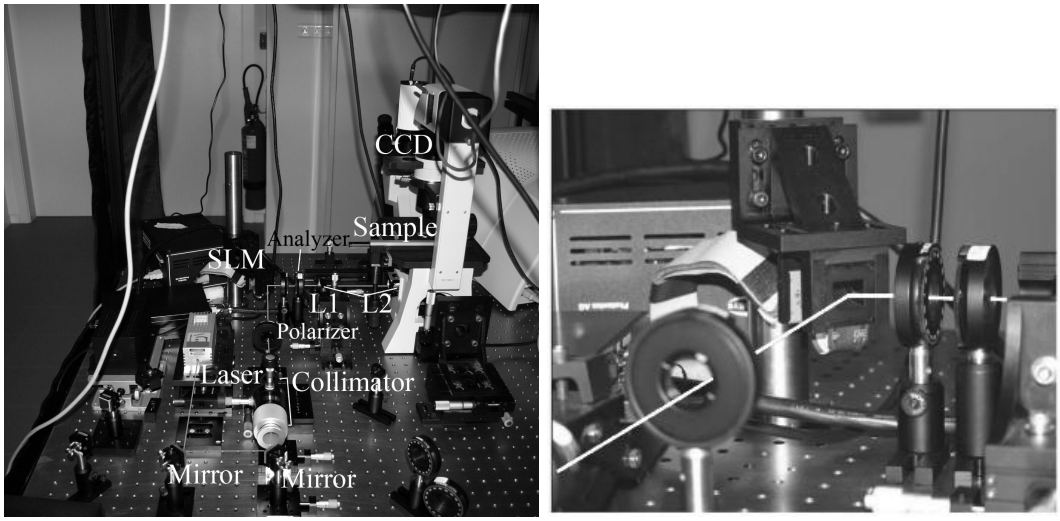


(a) (b)

**Figure 1.** (a) Experimental setup for the generation of holographic optical tweezers. L1 and L2 are the two lenses of the telescope, while the collimator is a system comprising an expander lens, a pinhole and a second lens which collimates the beam. (b) The modulator placed in the setup with an inclination angle of 45° with respect to the beam direction.

magnification of the collimator system is 8/75 (the focal ratio of the collimator), the beam is thus expanded to 8.7 mm.

The reflective modulator, a HoloEye LC-2500, is placed at 45° with respect to the beam direction (as seen in Figure 1(b)). This inclination avoids the need for a beam-splitter, which would reduce the efficiency to 25%. The experimental characterization of the modulation curve has been obtained with this inclination angle. As the illuminated area is $8.7\times(8.7\times\sqrt{2})$ mm and the HoloEye area is 14.6×19.6 mm, the borders of the modulator are not illuminated, thus avoiding the distortion they might cause to the beam.

Once reflected by the modulator the beam is resized by the telescope and enters the microscope. This telescope adapts the size of the beam to the objective pupil diameter. It comprises lenses L1 and L2 in Figure 1(a) and has a magnification of $M_{tel}$ = -0.4. The focal lengths are, respectively, $f_{L1}$ = 125 mm and $f_{L2}$ = 50 mm. The beam fills up the objective pupil after being reflected by the dichroic mirror inside the microscope. The SLM is placed between polarizing elements, whose function is to polarize the incident and reflected light in such a way as to achieve the nearly phase-only configuration shown in Figure 3.

The microscope objective focal length can be obtained from its magnification ($M$=100X). Figure 2 shows the objective and the visualization system. The lens that images the sample plane over the CCD camera is known as the tube lens. Its focal length is $f'_{tube}$ = 200 mm. The relationship between the objective focal length in air ($f$), $f'_{tube}$ and $M$ is $f = f'_{tube}/M = 2$ mm. The objective focal length in oil, $f'$, is obtained from the refraction index relationship: $f' = fn = 2mm \cdot 1.51 = 3.02$ mm. The position of the exit focal length of the telescope and the objective pupil should be as coincident as possible to avoid light loss. The above mentioned factors are important in the hologram generation because they determine the scale factor between the modulator plane and the sample plane.

The dichroic mirror has a dual function: it reflects the laser beam into the objective and allows the sample visualization of the CCD camera by filtering the reflected laser, thus avoiding camera saturation. The CCD camera used in the experiment is a QICam Fast 1934 from QImaging.

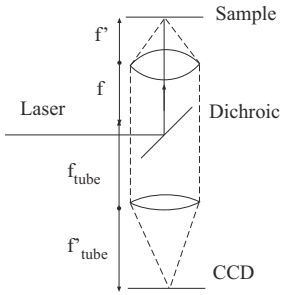


**Figure 2.** Objective-tube lens system in the microscope.

We have estimated the energy concentrated in one simple trap. The power concentrated in the sample plane is about a 25% of the incident power, taking into account the different transmittances of the optic elements and the efficiency of the modulation configuration.

## 2.1. Liquid Crystal Display HoloEye LCR2500

In this study we used a reflection twisted nematic LCoS (Liquid Crystal on Silicon). This offers phase modulation from 0 to $2\pi$ in the configuration considered, although the phase is coupled with a certain amplitude variation. A summary of its technical specifications[1] is shown in the table 1. This modulator was chosen for its high resolution and minor cost when compared with other commercial devices.

| **Parameter** | **HoloEye LCR2500** |
|---|---|
| In signal | XGA (1024×768 pixel) |
| Effective area | 19.6×14.6 mm |
| Pixel size | 19 $\mu$m × 19 $\mu$m |
| Frame rate | 72 Hz |
| Phase level modulation | $2\pi$ (400 nm-700 nm) |

**Table 1.** Technical specifications of the HoloEye LCR 2500 modulator

The display was characterized with a beam incident direction of 45° from the normal device surface, as placed in the experimental setup (see Figure 1(a)). The best phase operating curve achieved is shown in Figure 3.

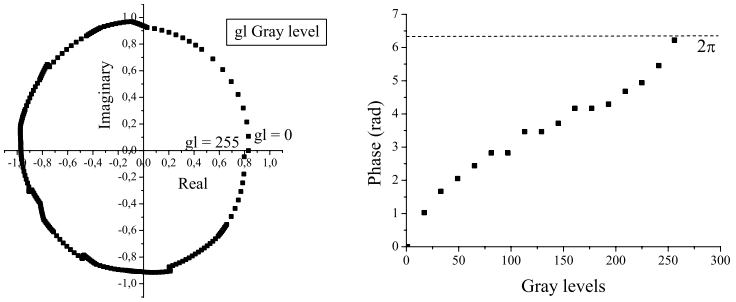


(a) (b)

**Figure 3.** (a) HoloEye LCR 2500 phase operating curve obtained (b) Experimental phase values vs. gray level

This characterization was obtained with $\lambda = 532$ nm, and the phase reaches $2\pi$. Its contrast is 1.25:1. The configuration efficiency is about 50%.

## 2.2. Aberration correction

The focalization of the beam in the microscope reveals two light lines instead of a diffraction limited spot. The two lines are perpendicular and appear at two different focal lengths. This behavior is similar to the presence of astigmatism, an aberration produced when a system converges at two different focal lengths. This kind of aberration is shown in Figure 4a.

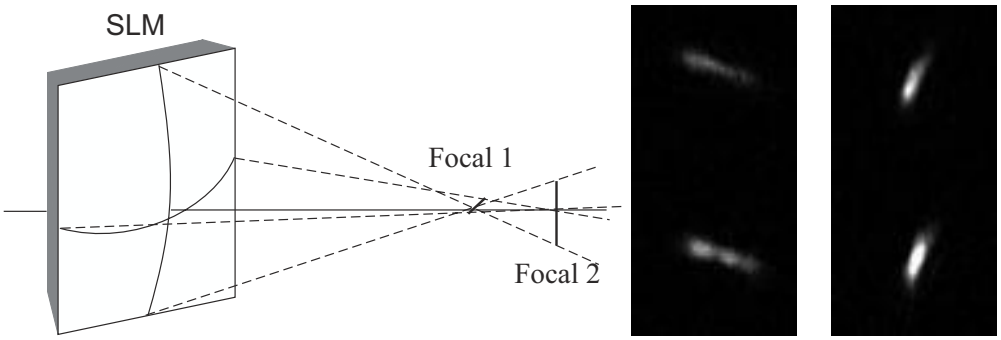


**Figure 4.** (a) Convergence of the reflected light from the modulator at two different focal lengths. (b) and (c) Experimental images showing two traps captured in the microscope in the Sturm focal lengths.

The light lines are known as Sturm focal lengths. Figures 4b and 4c show the captured images for the two Sturm focal lengths in the microscope for the generation of two traps. This behavior is shown even at normal incidence, thus revealing the lack of flatness of the device surface.

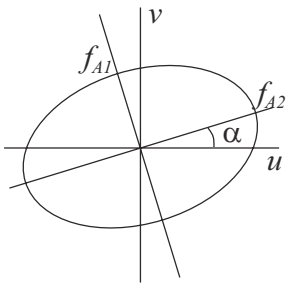


**Figure 5.** Correction of the modulator's aberration parameters

Let $(u, v)$ and $\alpha$ be the coordinates in the hologram plane and the angle between $u$ and the direction in which the focal length $f_{A1}$ is defined, respectively (see Figure 5). The aberration has been corrected by adding empirically a phase that counteracts it. The correction is dependent of focal lengths $f_{A1}$, $f_{A2}$ and $\alpha$. The phase function that corrects the aberration, $\phi_{ab}$, is modeled with the phase in equation 1. $u'$ and $v'$ are the $\alpha$-rotated axes of $u$ and $v$ (the modulator horizontal and vertical coordinates).

$$\phi_{ab} = -\frac{\pi}{\lambda}\left(\left(\frac{u'}{f_{A1}}\right)^2 + \left(\frac{v'}{f_{A2}}\right)^2\right), \quad (1)$$

con $u' = u\cos\alpha + v\sin\alpha$ and y $v' = v\cos\alpha - u\sin\alpha$.

Experimentally, the parameters obtained were $f_{A1} = 30$ m, $f_{A2} = 8$ m and $\alpha = 17^0$. The resulting phase correction, adapted to the modulator operating curve (Figure 3 (b)), is shown in Figure 6(a)a. Figures 6(c)b and 6(c)c show the experimental captured images of the traps in the middle distance between the two Sturm focal lengths and the post-correction spots, respectively. An explanation of how to characterize and correct aberrations in an SLM can be found in reference.[2]

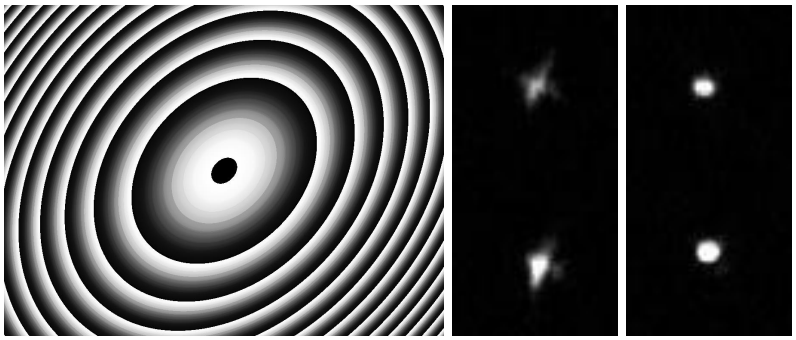

(a) (b) (c)

**Figure 6.** Spherical phase that corrects the HoloEye modulator aberration. Image of the two traps in the microscope (a) without correction (b) corrected.

## 3. DESCRIPTION OF THE INTERACTIVE APPLICATION

In this section we describe the hologram design process by means of a program that allows interactive manipulation with the sample. This software implements the random binary masks algorithm[3] for the fast generation of holograms and displays the distribution in the LCD in real time.[4]

The application is programmed in Java, a language that allows easy handling of the acceleration hardware capabilities and multi-threading programming. The program takes into account the experimental setup scale factors and different manipulation options, for example multiple vortex generation. The hologram generation includes the aberration correction and the experimental modulation of the LCD. A complete description of the application can be found in reference.[5]

The flowchart of the software is shown in Figure 7. It specifies the three block sources, the event handling class, the camera control class and the hologram calculation source. As an example, the flowchart shows the process of initializing the program, generating a trap and modifying its position.

The main thread of the program is responsible for the calculation and the interface event handling, whereas a second thread controls the camera and its related processes. The VolatileImage class, included in the Software Development Kit (SDK) of the Java Platform 5.0 is used to optimize the hologram displaying. This class takes advantage of the graphic hardware acceleration capabilities to display the images without using the CPU.[6] In this way, the calculation and the displaying of the holograms are parallel processes.

The integration of the camera, a QImaging QICam Fast 1394,[7] is achieved using the SDK provided by the manufacturer. Given that the SDK is designed to be used with C++, this library can be included in our

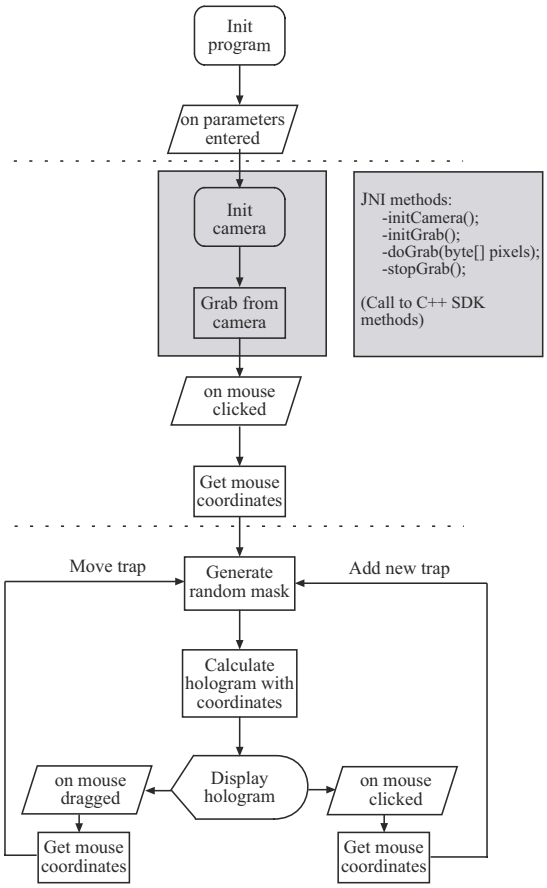


**Figure 7.** Flowchart of the interactive software.

Java software by using the Java Native Interface (JNI).[8] It allows calling to C or C++ functions from Java. A summary of the methods used to control the camera with the software is shown in Figure 7, while a more detailed description of JNI and the integration of FireWire cameras in Java can be found in reference.[8,9] A drawback of the program is that the FireWire camera that is not IEEE1394 compliant, and this limits the software that can be used with this specific camera.

Figure 8 shows the user interface of the application. The options included are:

1. the pixel size of the hologram,
2. the incorporation of the aberration correction and the modulator configuration through the *Init* button,
3. the selection of the trap to modify if there are several generated,
4. the possibility of modifying the trap depth with a slider,
5. multiple vortex generation,[10]
6. the button *Delete trap*, that is used to delete an undesired trap,
7. the user can change the hologram-generation method by clicking on the *RadioButton. The two available methods are the lenses and gratings*[11] *and the random binary masks*[4] *methods.*
8. *the Show/Hide grid shows the scale in the microscope field.*

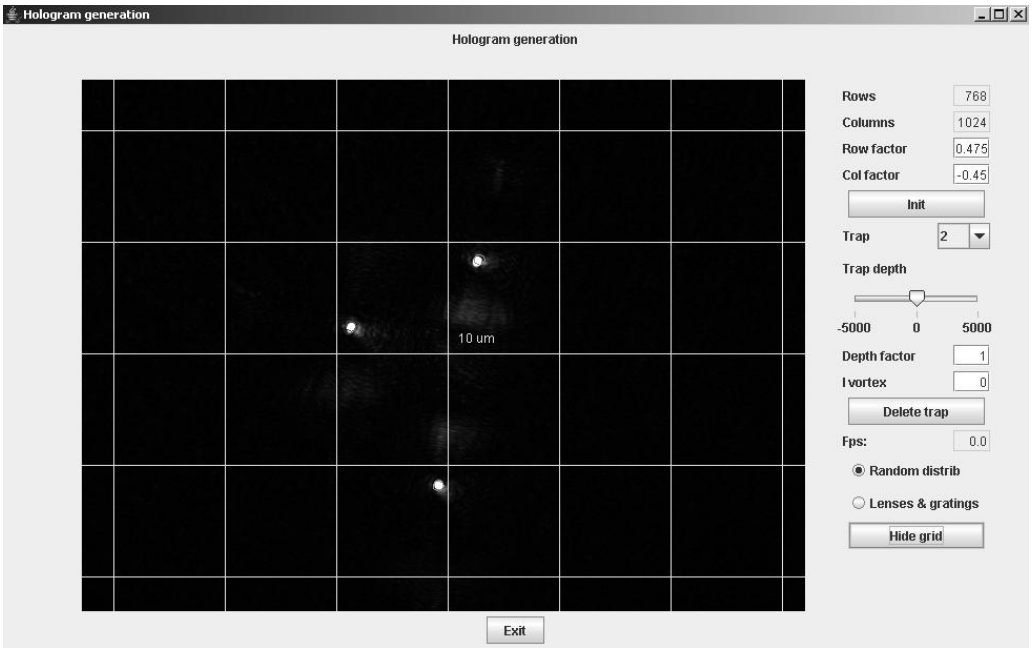


**Figure 8.** Main window program.

### 3.1. Hologram generation process

Once the user interface has been defined, it is necessary to study the steps involved in hologram generation. The modulator and the sample plane are related through a Fourier transform. In general, the hologram is complex-valued, and these values should be constrained to the experimental modulation available (see the operating curve shown in Figure 3). An off-axis trap is achieved with the function:

$$H(u,v) = \exp(i\frac{2\pi}{\lambda f}(ux_p + vy_p)), \tag{2}$$

where $f$ is the effective focal length of the whole optical system. The Fourier transform of the linear phase in Equation 2 is $\delta(x - x_p, y - y_p)$. The sum of different phase grating functions will show multiple off-axis traps. To change the depth by a distance $z$ from the focal plane a spherical phase has to be added to the desired linear phase function[11] (Equation 3).

$$H(u,v) = \exp(i\frac{\pi}{\lambda z}(u^2 + v^2)), \tag{3}$$

A hologram that combines multiple off-axis traps and/or displacements from the focal plane results in a non-phase distribution. There are different strategies to display a complex hologram using phase modulation such as the operating curve in Figure 3. We have used the random binary masks method, which divides the hologram into different pixel sets, each corresponding to a different trap. Each set will show the phase function that generates a single trap.[3,4]

The set of pixels that generates a trap is distributed at random in the hologram. Each set of pixels is called a random mask. The randomness is necessary to avoid the convolution of the trap with a geometric shape. Once the masks are generated, the phase corresponding to each trap is displayed in their disjoint masks. If a trap's coordinates are modified, only the phases in the trap mask have to be recalculated. This means that the calculation time does not increase if the trap number increases. Furthermore, no codification of the hologram distribution is needed because the function shown in each mask is a phase-only function. In contrast, the phases

and gratings method implies increased calculation time because the phase of the total distribution has to be computed.

The adjustment to the operating curve can be a time-consuming operation. To avoid this problem, we implemented a pre-calculated map that assigns a gray level to all the possible phases between 0 and $2\pi$ by means of the minimum Euclidean distance of the phases. The resulting calculation time is equivalent to considering an ideal phase function. However, by not taking into account the experimental modulation there is a loss of quality in the trap pattern.

We have also evaluated the speed of program calculation. Taking into account the aberration correction and a hologram size of 1024×768, the full modulator resolution, the software achieves 12 fps* when run on a Pentium IV HT, 3.2 GHz computer. If the resolution is 512×512 and no aberration correction is needed, the program achieves up to 20 fps. The speed is enough to ensure interactive manipulation of the sample in both cases, and in addition to being independent of the operating curve characteristics it does not increase with the trap number.

### 3.2. Manipulation of yeast cells

In this section we report experimental results of particle manipulation in real time using the software developed. Figure 9 shows different captures of the manipulation of two yeast cells, approximately 5 $\mu$m in diameter. First, a trap is generated to fix one cell position and thereafter another trap is used to move a second cell, moving it toward the first cell.

## 4. CONCLUDING REMARKS

We have presented a low-cost experimental setup designed to generate multiple dynamic holographic optical tweezers. The characteristics of the components have been explained in detail. The holograms displayed in the LCD are generated using a software that allows interactive manipulation, and which uses the random binary masks method. The performance of the software has been discussed and experimental results of trapped particles manipulated interactively have been reported.

## ACKNOWLEDGMENTS

This paper has been funded by the Spanish Ministry of Education and Science projects FIS2004-03450 and NAN2004-09348-C04-03.

## REFERENCES

1. `http://www.holoeye.com/download_daten/flyer_2500.pdf`, 2005.
2. K. D. Wulff, D. G. Cole, R. L. Clark, R. DiLeonardo, J. Leach, J. Cooper, G. Gibson, and M. J. Padgett, "Aberration correction in holographic optical tweezers," *Optics Express* **14**, pp. 4170–4175, 2006.
3. J. A. Davis and D. M. Cottrell, "Random mask encoding of multiplexed phase-only and binary phase-only filters," *Optics Letters* **19**, pp. 496–498, 1994.
4. M. Montes-Usategui, E. Pleguezuelos, J. Andilla, and E. Martín-Badosa, "Fast generation of holographic optical tweezers by random mask encoding of fourier components," *Optics Express* **14**, pp. 2101–2107, 2006.
5. E. Pleguezuelos, A. Carnicer, J. Andilla, and M. Montes, "Holotrap: a new software package for real-time optical trapping." Submitted to Computer Physics Communications. Available at `http://arxiv.org`, 2006.
6. `http://java.sun.com/j2se/1.5.0/docs/api/java/awt/image/VolatileImage.html`, 2004.
7. `http://www.qimaging.com/products/cameras/scientific/index.php`, 2004.
8. `http://java.sun.com/j2se/1.4.2/docs/guide/jni/index.html`, 2004.
9. B.-C. Lai, D. Woolley, and P. J. McKerrow, "Developing a java api for digital video control using the firewire sdk," *Proceedings AUC'2001*, pp. 9.1–8.9, (Townsville), 2001.
10. J. E. Curtis, B. A. Koss, and D. G. Grier, "Dynamic holographic optical tweezers," *Optics Communications* **207**, pp. 169–175, 2002.
11. J. Liesener, M. Reicherter, T. Haist, and H. J. Tiziani, "Multi-funcional optical tweezers using computer-generated holograms," *Optics Communications* **185**, pp. 77–82, 2000.

*frames per second

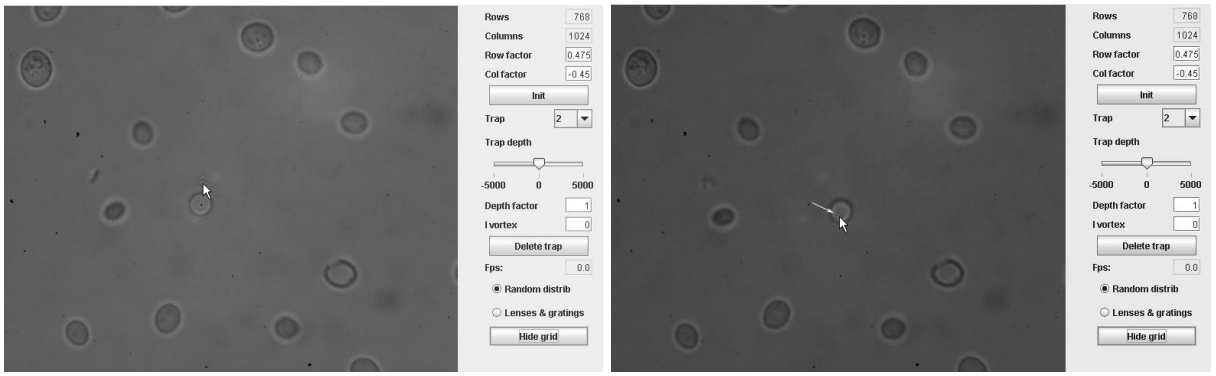


(a) (b)

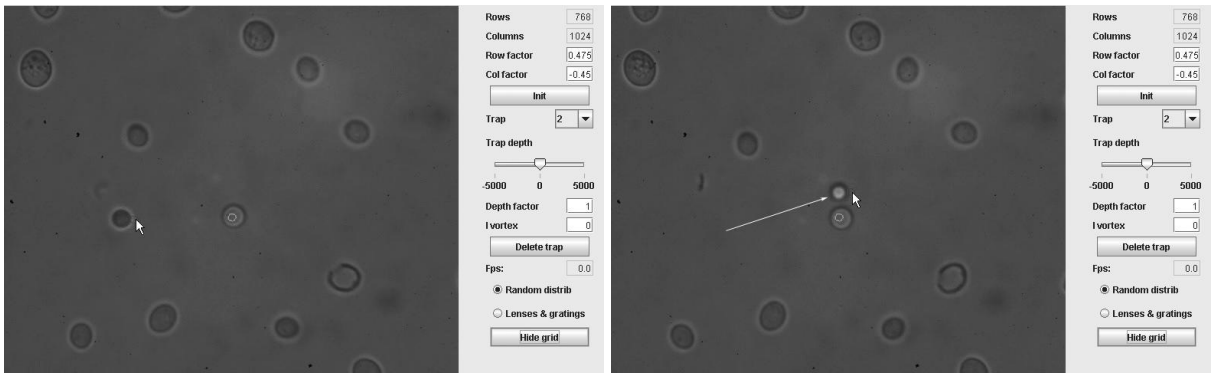


(c) (d)

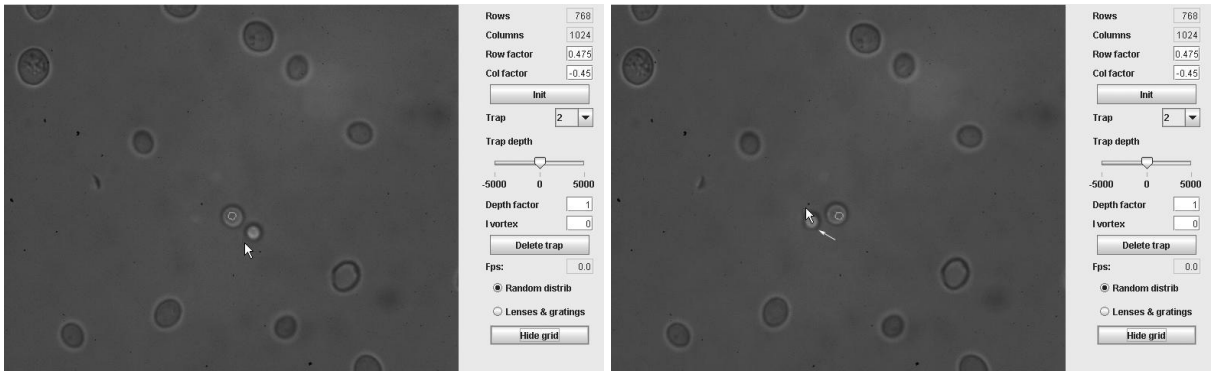


(e) (f)

**Figure 9.** Experimental captures of the interactive manipulation of yeasts cells, using the software developed.

# Appendix H

## Algorithm for computing holographic optical tweezers at video rates

Conference Proceeding, published in

Proceedings of SPIE
Vol.: 6326, 63262X, Sep. 2006

# Algorithm for computing holographic optical tweezers at video rates

Mario Montes-Usategui*, Encarnación Pleguezuelos, Jordi Andilla, Estela Martín-Badosa, and Ignasi Juvells
Grup de Recerca en Òptica Física, Departament de Física Aplicada i Òptica, Universitat de Barcelona, Martí i Franquès 1, Barcelona 08028, Spain

**ABSTRACT**

Digital holography enables the creation of multiple optical traps at arbitrary three-dimensional locations and spatial light modulators permit updating those holograms at video rates. However, the time required for computing the holograms makes interactive optical manipulation of several samples difficult to achieve. We introduce an algorithm for computing holographic optical tweezers that is both easy to implement and capable of speeds in excess of 10 Hz when running on a Pentium IV computer. A discussion of the pros and cons of the algorithm, a mathematical analysis of the efficiency of the resulting traps, as well as results of the three-dimensional manipulation of polystyrene micro spheres are included.

**Keywords:** Digital holography, phase-only filters and kinoforms, spatial light modulators, optical tweezers.

## 1. INTRODUCTION

Fast computation of holograms is a prerequisite for building interactive holographic optical manipulation systems. Unfortunately, the nonlinear and usually non-analytic relations between a hologram displayed onto a spatial light modulator and its corresponding reconstruction at the sample plane make the use of iterative, computational intensive algorithms often necessary [1-3]. Although fast manipulation is still feasible by computing the holograms off-line and then displaying them at video rates, only movements with pre-defined trajectories are then possible. Thus, interaction with a potential human operator needs real-time generation of holograms through faster algorithms [4-8] or by means of more powerful computing platforms, such as the graphic processing units of modern graphics boards [9,10].

As a matter of fact, rapid generation of optical traps can be achieved by alternate methods, which require no computation. For example, time-sharing the laser between traps [11] is a powerful, flexible and inexpensive possibility. However, in high-precision applications, the number of trapping sites needs to be small (4-6) [12] since the laser shifts prevent accurate measurements of applied force. Also, positioning and movement is limited only to two dimensions. The generalized phase contrast method [13] provides an instant conversion between phase and intensity and is therefore well suited to quickly generate optical traps with spatial light modulators (SLMs), through a frequency-filtering, all-optical, non-holographic approach. Nevertheless, the imaging nature of the setup makes it difficult to control the samples in three-dimensions [14].

Fresnel diffraction can be used to advantage [15] in real-time steering of optical tweezers since movement of the hologram on the computer screen translates into a similar movement of the corresponding trap. On the negative side, there seems to be a trade-off among trap efficiency, range of allowed movements and number of simultaneous traps because of the limited real state available on the SLM to display the holograms. In our opinion, all these methods lack the simplicity and universality of the traditional holographic approach.

This communication addresses the problem of the high computational load of most existing algorithms and presents a low-cost solution based on the random mask encoding technique of multiplexing phase-only filters [16]. The result is a direct, non-iterative and extremely fast algorithm that can be used for computing arbitrary arrays of optical traps. Additional benefits include the possibility of modifying any existing hologram to quickly add more trapping sites and the inexistence of ghost traps or replicas. The main drawback of the method is a reduced efficiency, being more suitable to generate a small number of optical traps. We have implemented the procedure on a Pentium IV personal computer and achieved frame rates in excess of 10 Hz with little code optimization. A Java front end allows the user to interactively manipulate microscopic samples just by clicking and dragging on a computer screen.

*mario_montes@ub.edu; www.ub.edu/optics

Optical Trapping and Optical Micromanipulation III, edited by Kishan Dholakia, Gabriel C. Spalding,
Proc. of SPIE Vol. 6326, 63262X, (2006) · 0277-786X/06/$15 · doi: 10.1117/12.680504

## 2. EXPERIMENTAL SETUP

Our experimental setup is shown in Fig. 1. It is very similar to that discussed in detail in Ref. 17 except for the microscope, which has been upgraded to a higher quality instrument.

A continuous-wave, frequency-doubled Nd:$YVO_4$ laser beam (Viasho Technology, $\lambda$=532 nm, 120 mW) is expanded by a spatial filter, collimated by lens L1 and linearly polarized by a high quality polarizer. It illuminates a twisted-nematic liquid-crystal spatial light modulator (Holoeye Photonics, LC-R 2500) sandwiched between a half-wave plate and an analyzer with the proper orientations to achieve phase-only modulation [17]. Interestingly, the Holoeye SLM is a reflective device and we place it tilted 45º with respect to the incident beam (see Figure 2). The usual configuration for a reflective modulator is to place it perpendicular to the optical axis and then redirect the beam out with a beam-splitter. However, the control of the input and output polarization is a much convenient feature of the setup as it allows free access to the different operating modes of the device (such as the phase-only modulation operating curve). Both constraints, polarization control and on-axis operation, can be met by the use of a non-polarizing beam-splitter but the round trip path through that element would result in a loss of 75% of the incident light. This is unacceptable considering the large power required for trapping even a small number of samples, so we discarded that possibility in favor of that shown in Figure 2. It is also very convenient from the point of view of arranging the whole optical setup and we have found that, although not lying on a plane perpendicular to the axis, the SLM is capable of producing fairly good traps.

Light finally enters an inverted microscope (Nikon Eclipse TE-2000E) through the fluorescence port and is reflected upwards by a dichroic mirror (Chroma Technology) to an oil-immersion, high numerical aperture, objective (Nikon Plan Fluor 100x, 1.30 NA). Lenses L2 and L3 (which is inside the microscope, attached to the fluorescence cube that contains the dichroic), image the SLM onto the exit pupil of the microscope objective to prevent vignetting of high frequency Fourier components [2,3]. They are arranged to form a telescope so as to still provide parallel illumination to the infinity-corrected objective. Finally, a CCD camera (Qimaging QICAM 1394) allows observation and recording of the experiments.

Since the spatial light modulator is illuminated by collimated light and the diffracted beams are observed at the focal plane of the objective lens (focal length, *f'*), the relation between the complex reflectance, *R(u,v)*, of the modulator and the electric field at the observation plane, *E(x,y)*, is, except for irrelevant phase terms [18], that of a Fourier transform:

$$E(x,y) = \iint R(u,v) e^{-i\frac{2\pi}{\lambda f'}(ux+vy)} du dv \,. \tag{1}$$

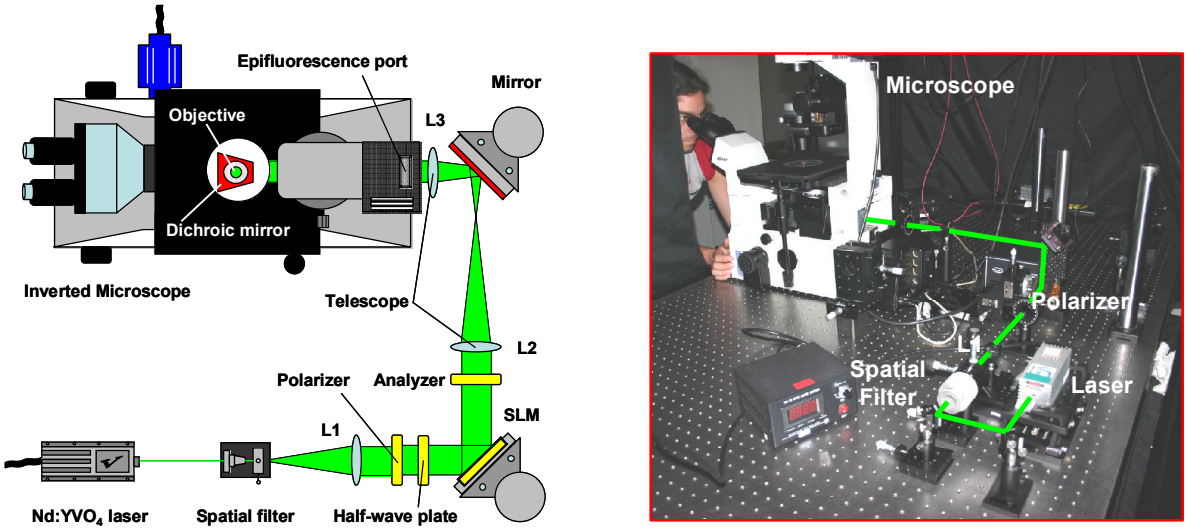


Fig. 1. Optical setup for generating holographic optical tweezers

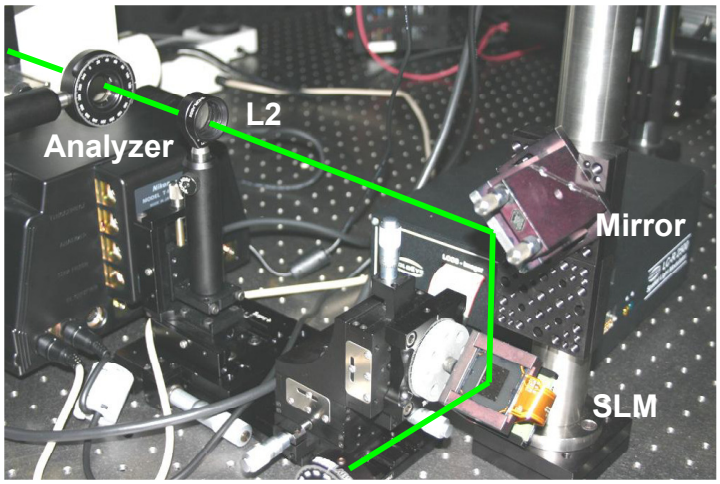


Fig. 2. Holoeye reflective spatial light modulator tilted 45º with respect to the optical axis

## 3. ALGORITHM

Given Eq. (1) above, when the spatial light modulator displays the hologram:

$$R(u,v)=\sum_{k=1}^{N} e^{i\frac{2\pi}{\lambda f'}(x_k u+y_k v)}, \tag{2}$$

a set of N off-axis traps will appear at positions $(x_k,y_k)$ on the sample plane, according to:

$$E(x,y)=\sum_{k=1}^{N}\iint e^{-i\frac{2\pi}{\lambda f'}[(x-x_k)u+(y-y_k)v]}dudv=\sum_{k=1}^{N}\delta(x-x_k,y-y_k). \tag{3}$$

Hologram $R(u,v)$ is the superposition of N linear phase functions with slopes $(x_k,y_k)$. Unfortunately, $R(u,v)$ is not a pure phase function and cannot be directly displayed on a modulator working in a phase-only configuration. Therefore, this problem needs to be solved if optical tweezers arrays by means of holographic optical elements on spatial light modulators are to be generated. The algorithms [1-6] try to find a hologram that, being a phase function, does not deviate significantly from the expected goal, that of producing the desired trap array. Such algorithms are usually iterative and computationally expensive.

Our solution is non-iterative. It is an adaptation of the random-mask encoding technique [7, 16] to this particular problem and consists of the multiplication of the linear phase functions in Eq. (2) by spatially disjoint binary masks, i.e.:

$$R(u,v)=\sum_{k=1}^{N} h_k(u,v)e^{i\frac{2\pi}{\lambda f'}(x_k u+y_k v)}, \tag{4}$$

where

$$h_k(u,v)=\begin{cases}1 & iff\ (u,v)\in I_k\\ 0 & otherwise\end{cases}, \tag{5}$$

with

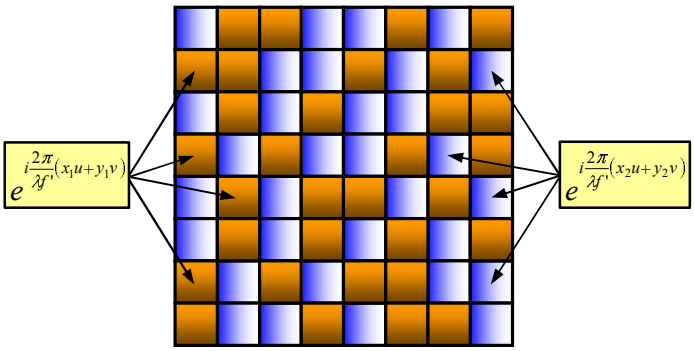


Fig. 3. Encoding two linear phases by complementary random binary masks.

$$I_l \cap I_m = \varnothing \quad \forall\, l,m \,\big|\, l \neq m \quad \text{and} \quad \bigcup_{k=1}^{N} I_k = \Re^2 \,. \tag{6}$$

That is, the method involves dividing the spatial light modulator into as many subdomains, $I_k$, as traps are required so that these subdomains do not overlap and jointly cover the whole modulator area. Then, each linear phase function is displayed only on the pixels of a given $I_k$. (see Fig. 3).

With this arrangement, *R(u,v)* is trivially a pure phase function with no further modification. Applying the convolution theorem [18] and Eq. (3), the field at the sample plane is:

$$E(x,y) = \sum_{k=1}^{N} H_k\left(x - x_k, y - y_k\right), \tag{7}$$

where $H_k(x,y)$ is the Fourier Transform of $h_k(u,v)$. Thus, function $H_k(x,y)$ appears centered at position $(x_k,y_k)$. If the binary masks are selected such that their Fourier transforms $H_k(x,y)$ consist of a single peak with flat sidelobes, then E(x,y) will be a good approximation to the desired array of optical traps. Random masks, as proposed in Ref. 16, give good results in this respect. For example, Fig. 4(a) shows a random binary mask with 50% of its pixels set to one and the remaining 50% to zero. Fig. 4(b) shows the magnitude squared of its Fourier transform, a sharp peak on a small random background. The scale on the Z axis is logarithmic so as better to show small intensity features, since the background is five orders of magnitude lower than the central peak.

Fig. 5 shows a comparison between the experimental results of this algorithm and those obtained by the "gratings and lenses" algorithm [6,8]. Notice the absence of ghost traps in Fig. 5(a) since off-trap energy tends to scatter over the whole sample plane, instead of concentrating at specific locations (giving undesired trapping sites, such as those in Fig. 5(b)).

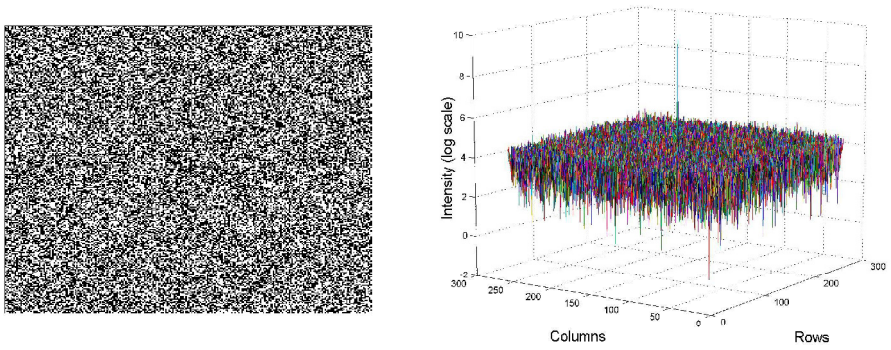


Fig. 4. a) Binary mask, 256x256 pixels. b) Magnitude squared of its Fourier transform (log scale).

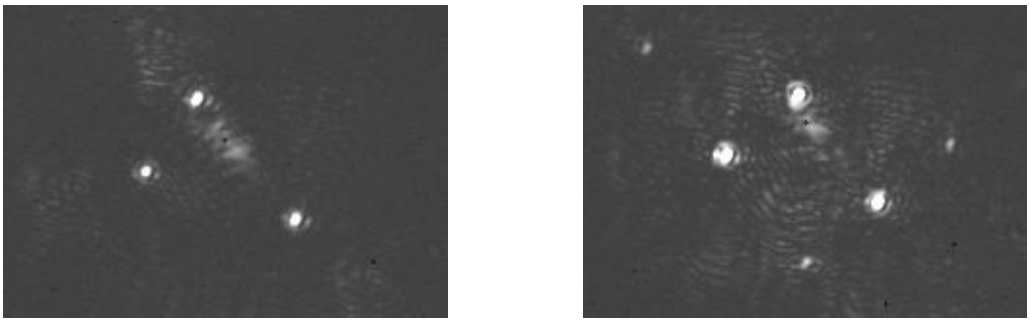

a) b)

Fig. 5. Three traps produced by the "random mask" (a) and the "gratings and lenses" (b) algorithms, respectively.

Also, Figure 5 shows the main drawback of our algorithm, a lower efficiency. The three traps in Fig. 5(a) are substantially less energetic than those in Fig. 5(b). In fact, the random mask encoding technique lends itself easily to analysis in this regard:

Let us consider a hologram, *R(j,k)*, of *NxN* pixels designed to create *P* traps and let us assume, with no loss of generality, that is illuminated by a plane wave of unit amplitude, A=exp(iφ). The energy at a plane immediately after the hologram is:

$$E_{TOT} = \sum_{j=1}^{N}\sum_{k=1}^{N}\left(R(j,k)A\right)^{*} R(j,k)A = \sum_{j=1}^{N}\sum_{k=1}^{N}\left|R\left(j,k\right)\right|^{2} , \tag{8}$$

whence, since the hologram is a pure phase function, we have:

$$E_{TOT} = NxN = N^{2} , \tag{9}$$

which, by virtue of Parseval's theorem, is also the total energy at the reconstruction plane.

On the other hand, the field amplitude at the *m*th trap position, $(r_m,s_m)$, can be written, in discrete notation, as:

$$\begin{aligned} C\left(r_m,s_m\right) &= \frac{1}{N}\sum_{j=1}^{N}\sum_{k=1}^{N} R\left(j,k\right)\exp\left[-i\frac{2\pi}{N}\left(r_m j + s_m k\right)\right] = \\ &= \frac{1}{N}\sum_{j=1}^{N}\sum_{k=1}^{N}\sum_{l=1}^{P} h_l\left(j,k\right)\exp\left\{-i\frac{2\pi}{N}\left[\left(r_m - r_l\right)j + \left(s_m - s_l\right)k\right]\right\} \approx \frac{1}{N}\sum_{j=1}^{N}\sum_{k=1}^{N} h_m\left(j,k\right) = \frac{1}{N}\frac{N^2}{P} = \frac{N}{P} \end{aligned} . \tag{10}$$

where *R(j,k)* represents the hologram and $h_l(j,k)$ the *l*th random binary mask.

Therefore, the total energy reaching the *P* traps is:

$$E_{TRAPS} \approx Px\left(\frac{N}{P}\right)^{2} = \frac{N^2}{P} , \tag{11}$$

whence, the efficiency of the hologram finally takes the form:

$$Efficiency = \frac{E_{TRAPS}}{E_{TOT}} \approx \left(\frac{N^2/P}{N^2}\right) = \frac{1}{P} . \tag{12}$$

## 4. ADDITIONAL USEFUL PROPERTIES

This procedure shows some useful features that we comment on below.

a) Intensity control

The intensity of optical traps generated by the algorithm shows a remarkable uniformity for a small number of traps. For example, in our experiments we have found maximum variations in intensity of less than 4% for arrays of 2x2 optical traps (512x512 pixel holograms). However, for larger arrays (6x6) the intensity variations may increase up to 25%. When this is a problem or if the optical traps have to be of different intensity, a slightly more elaborate algorithm needs to be used [16]. Masks corresponding to traps that are required to be brighter are selected with a somewhat larger pixel count at the expense of other masks (those corresponding to traps need to be weaker).

b) Incremental updating and hologram multiplexing

Contrary to other algorithms, all information is very well localized within the binary masks so addition of new trapping sites can be done without recomputing the whole hologram. Specifically, for a hologram of $N$ pixels that encode $m$ traps, $N/[m(m+1)]$ pixels from each binary mask are randomly discarded. Then, the resulting $N/(m+1)$ pixels are used to codify the new linear phase. Only these latter pixels need to be updated.

Interestingly, this can be done over a hologram computed with any other algorithm, in which the information is distributed: discard a number of pixels and use them to produce a new trapping site with the random mask encoding technique. None of the existing traps is more affected than the others, the net effect is a lower-energy set of existing traps and a new trapping site at the desired location. This may be used to temporarily add a new trap to a pre-existing, higher-quality hologram, for example, for loading an array of optical traps with microscopic samples. Finally, the loading trap can be removed by restoring the original pixels.

Fig. 6 shows the result of adding a new trapping site to a hologram computed by the Gerchberg-Saxton algorithm [3,4,6] to produce an array of 2x2 optical traps. One fifth of its pixels were used to encode the new linear phase function. Again, the figure shows that the new trap is significantly less energetic than equivalent traps computed by the other algorithm. We are studying a possible solution to this low efficiency based on reducing the randomness of the binary masks (Fig. 7, simulated results).

Finally, two or more holograms can be multiplexed by multiplication of binary disjoint random masks to merge their individual properties into a single hologram.

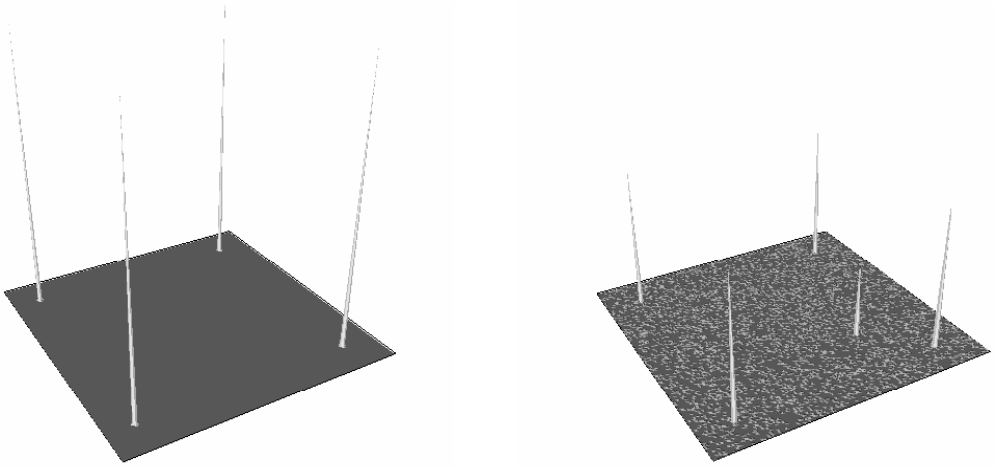

Fig. 6. Addition of a new trap to an already existing hologram.

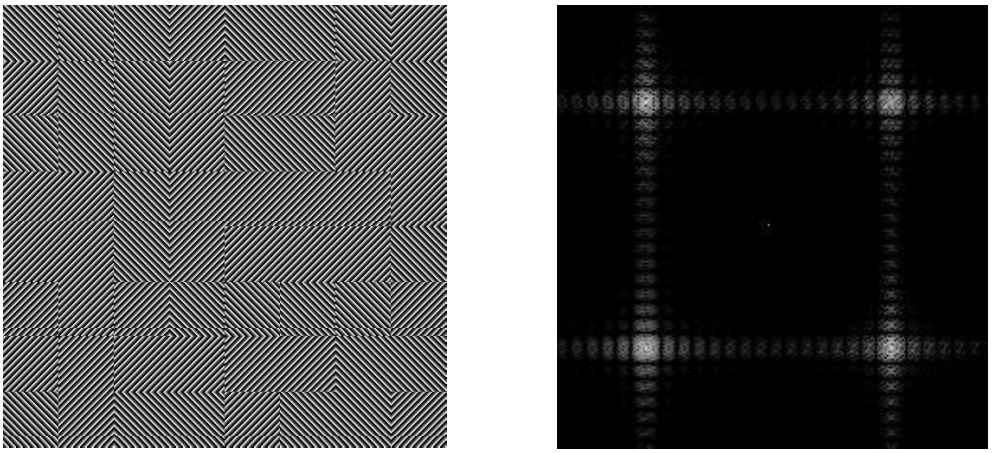

a) b)

Fig. 7. Modified hologram based on less random binary masks (a) and generated traps (b).

c) Speed

Once the random masks are selected, the hologram can be directly written onto the spatial light modulator with little extra computation. Thus, the procedure is very fast and can be easily carried out at near video-rates, therefore enabling real-time interaction with the user. We have developed an interactive holographic optical manipulation system based on this algorithm, as shown in the following image sequences (Figs. 8 and 9). The control software is implemented in Java and is capable of displaying holograms (512x512 pixels) at an average rate of 10-12 Hz (including aberration correction of the Holoeye SLM and compensation of the operating curve nonlinearities), using a Pentium IV HT, 3.2 Ghz, computer.

## 5. CONCLUSIONS

We propose a new procedure for the generation of holographic optical tweezers based on the random mask encoding technique. The result is a direct, non-iterative algorithm that has a number of positive features. Specifically, the algorithm is very fast and video-rate generation is easy to achieve. Moreover, the algorithm does not produce ghost traps and can be used to add further trapping sites to existing holograms, even those generated by other algorithms, without the need to re-compute them. Finally, the main limitation of this procedure seems to be hologram efficiency. We have shown that the efficiency, defined as the ratio between the energy of the traps to the total energy at the sample plane, decreases monotonically with increasing number of traps. Thus the algorithm seems suitable only to generate a small number of optical tweezers.

## ACKNOWLEDGEMENTS

This work has been funded by the Spanish Ministry of Education and Science, under grants FIS2004-03450 and NAN2004-09348-C04-03.

## REFERENCES

1. M. Reicherter, T. Haist, E. Wagemann, and H. Tiziani, "Optical particle trapping with computer-generated holograms written on a liquid-crystal display," Opt. Lett. **24**, 608-610 (1999).
2. D. G. Grier, "A revolution in optical manipulation," Nature **424**, 810-816 (2003).

3. J. E. Curtis, B. A. Koss, and D. G. Grier, “Dynamic holographic optical tweezers,” Opt. Commun. **207**, 169–175 (2002).
4. G. Sinclair, J. Leach, P. Jordan, G. Gibson, E. Yao, Z. J. Laczik, M. J. Padgett, and J. Courtial, "Interactive application in holographic optical tweezers of a multi-plane Gerchberg-Saxton algorithm for three-dimensional light shaping," Opt. Express **12,** 1665-1670 (2004).
5. M. Polin, K. Ladavac, S. Lee, Y. Roichman, and D. G. Grier, "Optimized holographic optical traps," Opt. Express **13,** 5831-5845 (2005).
6. J. Curtis, C. Schmitz, and J. Spatz, "Symmetry dependence of holograms for optical trapping," Opt. Lett. **30**, 2086-2088 (2005).
7. M. Montes-Usategui, E. Pleguezuelos, J. Andilla, and E. Martín-Badosa, "Fast generation of holographic optical tweezers by random mask encoding of Fourier components," Opt. Express **14**, 2101-2107 (2006).
8. J. Leach, K. Wulff, G. Sinclair, P. Jordan, J. Courtial, L. Thomson, G. Gibson, K. Karunwi, J. Cooper, Z. J. Laczik, and M. Padgett, "Interactive approach to optical tweezers control," Appl. Opt. **45**, 897-903 (2006).
9. N. Masuda, T. Ito, T. Tanaka, A. Shiraki, and T. Sugie, "Computer generated holography using a graphics processing unit," Opt. Express **14**, 603-608 (2006)
10. M. Reicherter, S. Zwick, T. Haist, C. Kohler, H. Tiziani, and W. Osten, "Fast digital hologram generation and adaptive force measurement in liquid-crystal-display-based holographic tweezers," Appl. Opt. **45**, 888-896 (2006)
11. K. Visscher, S. P. Gross, and S. M. Block “Construction of multiple-beam optical traps with nanometer-resolution position sensing,” IEEE J. Sel. Top. Quantum Electron. **2**, 1066-1076 (1996).
12. Guilford, W.H., J.A. Tournas, D. Dascalu, and D.S. Watson, “Creating multiple, time-shared laser traps with simultaneous displacement detection using digital signal processing hardware.” Anal. Biochem. **326**, 153-166 (2004).
13. R. Eriksen, P. Mogensen, and J. Glückstad, "Multiple-beam optical tweezers generated by the generalized phase-contrast method," Opt. Lett. **27**, 267-269 (2002).
14. P. J. Rodrigo, V. R. Daria, and J. Glückstad, “Four-dimensional optical manipulation of colloidal particles,” Appl. Phys. Lett. **86**, 074103 (2005).
15. A. Jesacher, S. Fürhapter, S. Bernet, and M. Ritsch-Marte, "Diffractive optical tweezers in the Fresnel regime," Opt. Express **12**, 2243-2250 (2004)
16. J. Davis and D. Cottrell, "Random mask encoding of multiplexed phase-only and binary phase-only filters," Opt. Lett. **19**, 496-498 (1994).
17. E. Pleguezuelos, J. Andilla, A. Carnicer, E. Martín-Badosa, S. Vallmitjana, and M. Montes-Usategui, “Design of a low-cost, interactive, holographic optical tweezers system,” Proc of SPIE, this same volume.
18. J. W. Goodman, *Introduction to Fourier Optics* (McGraw-Hill, 1996).

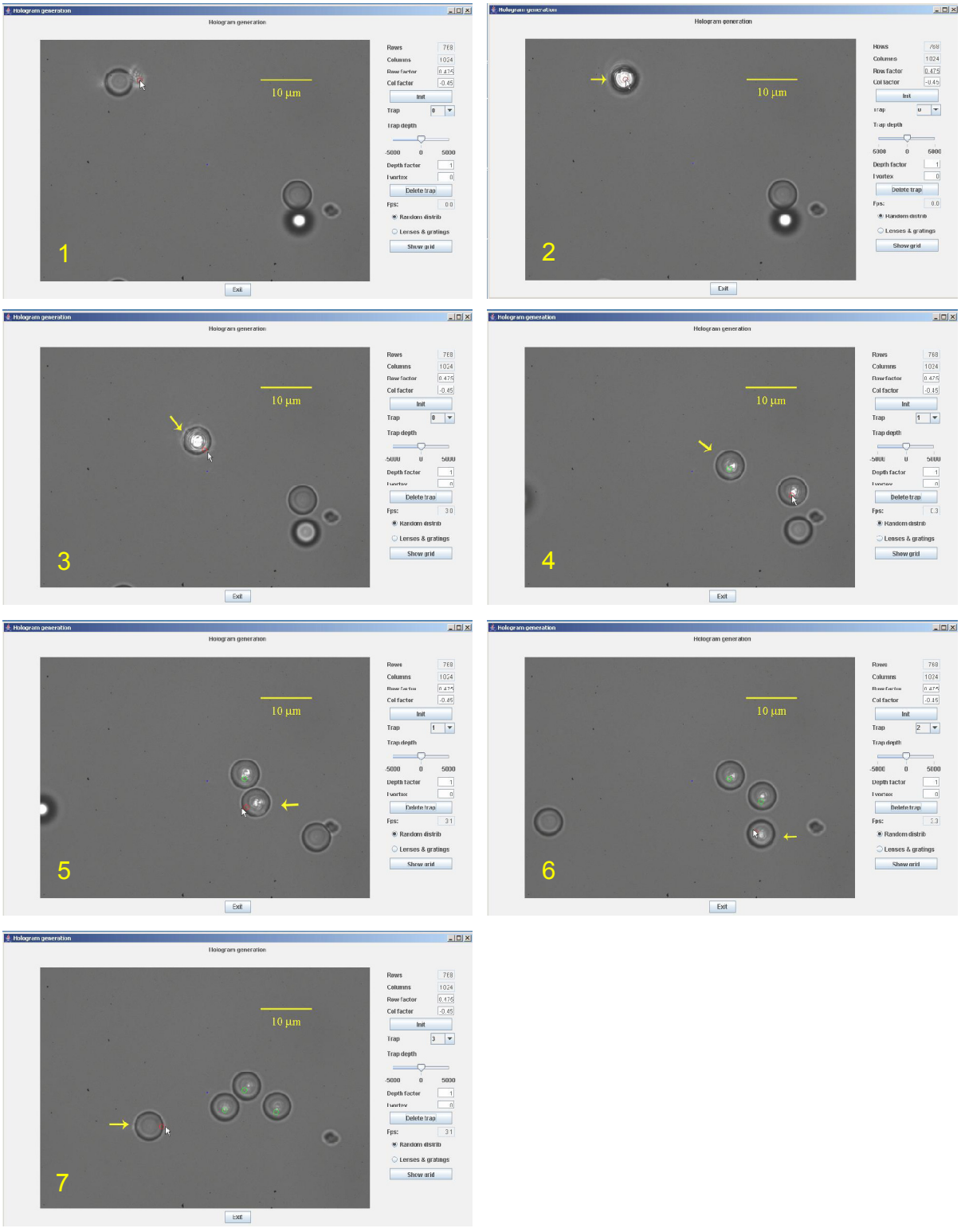


Fig. 8. Sequence of images showing the trapping and manipulation of four polystyrene microspheres.

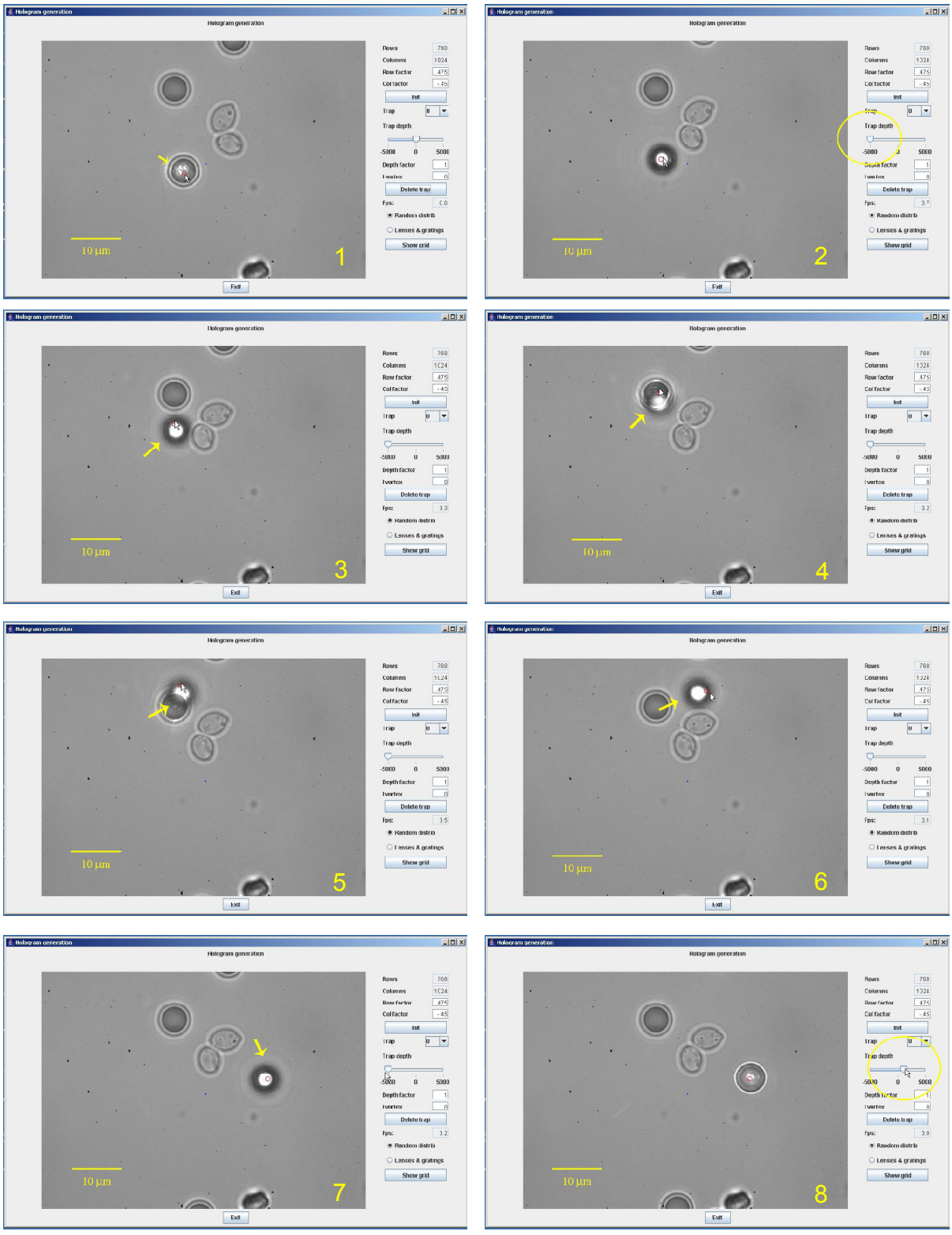


Fig. 9. Sequence of images showing trapping and manipulation in three dimensions.

# References


[AD87] A. Ashkin and J. Dziedzic, 'Optical trapping and manipulation of viruses and bacteria', *Science* 235(4795), 1517–1520 (1987).

[ADBC86] A. Ashkin, J. M. Dziedzic, J. E. Bjorkholm and S. Chu, 'Observation of a single-beam gradient force optical trap for dielectric particles', *Opt. Lett.* 11(5), 288–290 (1986).

[ADY87] A. Ashkin, J. M. Dziedzic and T. Yamanet, 'Optical trapping and manipulation of single cells using infrared laser beams', *Nature* 330, 769–771 (1987).

[AGCSD01] J. Arlt, V. Garces-Chavez, W. Sibbett and K. Dholakia, 'Optical micromanipulation using a bessel light beam', *Opt. Commun.* 197, 239–245 (2001).

[AGS+05] E. A. Abbondanzieri, W. J. Greenleaf, J. W. Shaevitz, R. Landick and S. M. Block, 'Direct observation of base-pair stepping by RNA polymerase', *Nature* 438(24), 460–465 (2005).

[AJL+02] B. Alberts, A. Johnson, J. Lewis, M. Raff, K. Roberts and P. Walter. *Molecular biology of the cell. 4th edn.*. Garland Science, New York (2002).

[ASD+90] A. Ashkin, K. Schütze, J. M. Dziedzic, U. Euteneuer and M. Schliwa, 'Force generation of organelle transport measured in vivo by an infrared laser trap', *Nature* 348, 346–348 (1990).

[Ash70] A. Ashkin, 'Acceleration and trapping of particles by radiation pressure', *Phys. Rev. Lett.* 24, 156–159 (1970).

[Ash72] A. Ashkin, 'The pressure of laser light', *Sci. Am.* 281, 63–71 (1972).

[Ash92] A. Ashkin, 'Forces of a single-beam gradient laser trap on a dielectric sphere in the ray optics regime', *Biophys. J.* 61, 569–582 (1992).

[BJ95] R. S. Barton and R. D. Juday. 'Minimum Euclidean distance optimal filter (MEDOF): version 2.0'. vol. 2490, pp. 14–22. SPIE (1995).

[Blo90] S. Block. 'Chapter 15, Optical tweezers: a new tool for biophysics'. S. Grinstein and K. Foskett, (Ed), *Vol. 9, Noninvasive Techniques in Cell Biology*, pp. 375–401. Wiley-Liss, New York (1990).

[BMMS08] F. Belloni, S. Monneret, F. Monduc and M. Scordia, 'Multiple holographic optical tweezers parallel calibration with optical potential well characterization', *Opt. Express* 16(12), 9011–9020 (2008).

[BSF04] K. Berg-Sørensen and H. Flyvbjergb, 'Power spectrum analysis for optical tweezers', *Rev. Sci. Inst.* 75(3), 594–612 (2004).

[BSG+03] Z. Bryant, M. D. Stone, J. Gore, S. B. Smith, N. R. Cozzarelli and C. Bustamante, 'Structural transitions and elasticity from torque measurements on DNA', *Nature* 424, 338–341 (2003).

[BWA+99] C. Bouchiat, M. D. Wang, J. F. Allemand, T. Strick, S. M. Block and V. Croquette, 'Estimating the persistence length of a worm-like chain molecule from force-extension curves', *Biophys. J.* 76, 409–413 (1999).

[BWRM07] D. R. Burnham, G. D. Wright, N. D. Read and D. McGloin, 'Holographic and single beam optical manipulation of hyphal growth in filamentous fungi', *J. Opt. A: Pure Appl. Opt.* 9, S172–S179 (2007).

[CEV97] J. Conia, B. S. Edwards and S. Voelkel, 'The micro-robotic laboratory: Optical trapping and scissing for the biologist', *J. Clin. Lab. Anal.* 11, 28–38 (1997).

[CKG02] J. E. Curtis, B. A. Koss and D. G. Grier, 'Dynamic holographic optical tweezers', *Opt. Commun.* 207, 169–175 (2002).

[CMVP07] M. Capitanio, D. Maggi, F. Vanzi and F. S. Pavone, 'Fiona in the trap: the advantages of combining optical tweezers and fluorescence', *J. Opt. A: Pure Appl. Opt.* 9, S157–S163 (2007).

[CRB+02] M. Capitanio, G. Romano, R. Ballerini, M. Giuntini, F. S. Pavone, D. Dunlap and L. Finzi., 'Calibration of optical tweezers with differential interference contrast signals', *Rev. Sci. Inst.* 73(4), 1687–1696 (2002).

[CRJ+05] D. Collin, F. Ritort, C. Jarzynski, S. B. Smith, I. Tinoco and C. Bustamante, 'Verification of the Crooks fluctuation theorem and recovery of RNA folding free energies', *Nature* 437, 231–234 (2005).

[CSS05] J. E. Curtis, C. H. J. Schmitz and J. P. Spatz, 'Symmetry dependence of holograms for optical trapping', *Opt. Lett.* 30(16), 2086–2088 (2005).

[DC94] J. A. Davis and D. M. Cottrell, 'Random mask encoding of multiplexed phase-only and binary phase-only filters', *Opt. Lett.* 19, 496–498 (1994).

[DG98] E. R. Dufresne and D. G. Grier, 'Optical tweezer arrays and optical substrates created with diffractive optics', *Rev. Sci. Inst.* 69(5), 1974–1977 (1998).

[DKM+04] M. A. van Dijk, L. C. Kapitein, J. van Mameren, C. F. Schmidt and E. J. G. Peterman, 'Combining optical trapping and single-molecule fluorescence spectroscopy: Enhanced photobleaching of fluorophores', *J. Phys. Chem. B* 108, 6479–6484 (2004).

[DS95] J. Dai and M. P. Sheetz, 'Mechanical properties of neuronal growth cone membranes studied by tether formation with laser optical tweezers', *Biophys. J.* 68, 988–996 (1995).

[EBS+02] A. Ehrlicher, T. Betz, B. Stuhrmann, D. Koch, V. Milner, M. Raizen and J. Käs, 'Guiding neuronal growth with light', *Proc. Natl. Acad. Sci. U.S.A.* 99(25), 16024–16028 (2002).

[EBS+07] A. Ehrlicher, T. Betz, B. Stuhrmann, M. Gögler, D. Koch, K. Franze, Y. Lu and J. Käs. 'Chapter 21, Optical neuronal guidance'. *Vol. 83, Methods Cell Biol.*, pp. 495–520. Elsevier Inc. (2007).

[EDG02] R. L. Eriksen, V. R. Daria and J. Glückstad, 'Fully dynamic multiple-beam optical tweezers', *Opt. Express* 10(14), 597–602 (2002).

[EKL+07] E. Eriksson, S. Keen, J. Leach, M. Goksör and M. J. Padgett, 'The effect of external forces on discrete motion within holographic optical tweezers', *Opt. Express* 15(26), 18268–18274 (2007).

[FA97] E. Fällman and O. Axner, 'Design for fully steerable dual-trap optical tweezers', *Appl. Opt.* 36, 2107–2113 (1997).

[FA03] E. Fällman and O. Axner, 'Influence of a glass-water interface on the on-axis trapping of micrometer-sized spherical objects by optical tweezers', *Appl. Opt.* 42, 3915–3926 (2003).

[FBI+05] N. Fukuchi, Y. Biqing, Y. Igasaki, N. Yoshida, Y. Kobayashi and T. Hara, 'Oblique-incidence characteristics of a parallel-aligned nematic-liquid-crystal spatial light modulator', *Opt. Rev.* 12(5), 372–377 (2005).

[FSS94] J. Finer, R. Simmons and J. Spudich, 'Single myosin molecule mechanics: piconewton forces and nanometre steps', *Nature* 368, 113–119 (1994).

[GO01] P. Galajda and P. Ormos, 'Complex micromachines produced and driven by light', *Appl. Phys. Lett.* 78(2), 249–251 (2001).

[Goo96] J. W. Goodman. *Introduction to Fourier Optics*. McGraw-Hill, Singapore (1996).

[Gri03] D. G. Grier, 'A revolution in optical manipulation', *Nature* 424, 810–816 (2003).

[GS72] B. Gerchberg and W. Saxton, 'A practical algorithm for the determination of the phase from image and diffraction plane pictures', *Optik* (35), 237–237 (1972).

[GS98] F. Gittes and C. F. Schmidt, 'Interference model for back-focal-plane displacement detection in optical tweezers', *Opt. Lett.* 23(1), 7–9 (1998).

[GTDW04] W. H. Guilford, J. A. Tournas, D. Dascalu and D. S. Watson, 'Creating multiple time-shared laser traps with simultaneous displacement detection using digital signal processing hardware', *Anal. Bioch.* 326, 153–166 (2004).

[HA96] Y. Harada and T. Asakura, 'Radiation forces on a dielectric sphere in the Rayleigh scattering regime', *Opt. Commun.* 124, 529–541 (1996).

[HGR+85] B. Hamprecht, T. Glaser, G. Reiser, E. Bayer and F. Propst, 'Culture and characteristics of hormone responsive neuroblastoma x glioma hybrid cells', *Meth. Enzymol.* 109, 316–341 (1985).

[HST97] T. Haist, M. Schönleber and H. J. Tiziani, 'Computer-generated holograms from 3d-objects written on twisted-nematic liquid crystal displays', *Opt. Commun.* 140, 299–308 (1997).

[KS93] S. Kuo and M. Sheetz, 'Force of single kinesin molecules measured with optical tweezers', *Science* 260(5105), 232–234 (1993).

[KSH+07] H. Kress, E. H. K. Stelzer, D. Holzer, F. Buss, G. Griffiths and A. Rohrbach, 'Filopodia act as phagocytic tentacles and pull with discrete steps and a load-dependent velocity', *Proc. Natl. Acad. Sci. U.S.A.* 104(28), 11633–11638 (2007).

[LRHT00] J. Liesener, M. Reicherter, T. Haist and H. J. Tiziani, 'Multi-funcional optical tweezers using computer-generated holograms', *Opt. Commun.* 185, 77–82 (2000).

[LRM+07] W. M. Lee, P. J. Reece, R. F. Marchington, N. K. Metzger and K. Dholakia, 'Construction and calibration of an optical trap on a fluorescence optical microscope', *Nat. Protoc.* 2, 3226–3238 (2007).

[LS04] K. Lu and B. E. A. Saleh, 'Complex amplitude reflectance of the liquid crystal light valve', *Appl. Opt.* 30(17), 2354–2362 (2004).

[LWS+06] J. Leach, K. Wulff, G. Sinclair, P. Jordan, J. Courtial, L. Thomson, G. Gibson, K. Karunwi, J. Cooper, Z. J. Laczik and M. Padgett, 'An interactive approach to optical tweezers control', *Appl. Opt.* 5, 897–903 (2006).

[LYC04] W. M. Lee, X.-C. Yuan and W. C. Cheong, 'Optical vortex beam shaping by use of highly efficient irregular spiral phase plates for optical micromanipulation', *Opt. Lett.* 29(15), 1796–1798 (2004).

[MB98] E. Martín-Badosa. *Correlador óptico para el reconocimiento de objetos basado en las propiedades de modulación de los dispositivos de cristal líquido*. Tesi Doctoral, Universitat de Barcelona, Barcelona (1998).

[MCI+06] J. R. Moffitt, Y. R. Chemla, D. Izhaky, and C. Bustamante, 'Differential detection of dual traps improves the spatial resolution of optical tweezers', *Proc. Natl. Acad. Sci. U.S.A.* 103(24), 9006–9011 (2006).

[MCL+04] R. Mallik, B. C. Carter, S. A. Lex, S. J. King and S. P. Gross, 'Cytoplasmic dynein functions as a gear in response to load', *Nature* 427, 649–652 (2004).

[MSK+92] H. Misawa, K. Sasaki, M. Koshioka, N. Kitamura and H. Masuhara, 'Multibeam laser manipulation and fixation of microparticles', *Appl. Phys. Lett.* 60, 310–312 (1992).

[nas78] `http://history.nasa.gov/SP-424/sp424.htm` (1978).

[NBMW07] M. C. Noom, B. van den Broek, J. van Mameren and G. J. L. Wuite, 'Visualizing single DNA-bound proteins using DNA as a scanning probe', *Nat. Methods* 4(12), 1031–1036 (2007).

[Pet07] D. V. Petrov, 'Raman spectroscopy of optically trapped particles', *J. Opt. A: Pure Appl. Opt.* 9, S139–S156 (2007).

[Ple06] E. Pleguezuelos. *Diseño interactivo de hologramas para la obtención de múltiples trampas ópticas dinámicas*. Tesi Doctoral, Universitat de Barcelona, Barcelona (2006).

[RGG94] K. Ren, G. Gréhan and G. Gouesbet, 'Radiation pressure forces exerted on a particle arbitrarily located in a Gaussian beam by using the generalized Lorenz-Mie theory, and associated resonance effects', *Opt. Commun.* 108, 343–354 (1994).

[RHWT99] M. Reicherter, T. Haist, E. U. Wagemann and H. J. Tiziani, 'Optical particle trapping with computer-generated holograms written on a liquid-crystal display', *Opt. Lett.* 24(9), 608–610 (1999).

[RS01] A. Rohrbach and E. H. K. Stelzer, 'Optical trapping of dielectric particles in arbitrary fields', *J. Opt. Soc. Am. A* 18, 839–853 (2001).

[RWGG06] Y. Roichman, A. Waldron, E. Gardel and D. G. Grier, 'Optical traps with geometric aberrations', *Appl. Opt.* 45, 3425–3429 (2006).

[SB94a] K. Svoboda and S. M. Block, 'Biological applications of optical forces.', *Ann. Rev. Biophys. Biomol. Struct.* 23, 247–285 (1994).

[SB94b] K. Svoboda and S. M. Block, 'Force and velocity measured for single kinesin molecules.', *Cell* 77, 773–784 (1994).

[SB05] S. B. Smith and C. Bustamante, *A light-force sensor and method for measuring axial optical-trap forces from changes in light momentum along an optic axis, US Patent # 029139* (2005).

[SCB96] S. B. Smith, Y. Cui and C. Bustamante, 'Overstretching B-DNA: The elastic response of individual double-strandedand single-stranded DNA molecules', *Science* 271(5250), 795–799 (1996).

[SCB03] S. B. Smith, Y. Cui and C. Bustamante, 'Optical-trap force transducer that operates by direct measurement of light momentum', *Meth. Enzymol.* 361, 134–162 (2003).

[SFCS96] R. M. Simmons, J. T. Finer, S. Chu and J. A. Spudich, 'Quantitative measurements of force and displacement using an optical trap', *Biophys. J.* 70, 1813–1822 (1996).

[SSSB94] K. Svoboda, C. F. Schmidt, B. J. Schnapp and S. M. Block, 'Direct observation of kinesin stepping by optical trapping interferometry', *Nature* 365, 721–727 (1994).

[STS+01] D. E. Smith, S. J. Tans, S. B. Smith, S. Grimes, D. L. Anderson and C. Bustamante, 'The bacteriophage $\phi 29$ portal motor can package DNA against a large internal force', *Nature* 413(18), 748–752 (2001).

[TMBZ98] T. Tlusty, A. Meller and R. Bar-Ziv, 'Optical gradient forces of strongly localized fields', *Phys. Rev. Lett.* 81(8), 1738–1741 (1998).

[VBK93] K. Visscher, G. Brakenhoff and J. Krol, 'Micromanipulation by 'multiple' optical traps created by a single fast scanning trap integrated with the bilateral confocal scanning laser microscope', *Cytometry* 14, 105–114 (1993).

[VGB96] K. Visscher, S. P. Gross and S. M. Block, 'Construction of multiple-beam optical traps with nanometer-resolution position sensing', *IEEE J-STQE* 2(4), 1066–1076 (1996).

[wat00] `http://www.microscopyu.com/articles/optics/waterimmersionobjectives.html` (2000).

[WGP+98] M. A. Welte, S. P. Gross, M. Postner, S. M. Block and E. F. Wieschaus, 'Developmental regulation of vesicle transport in drosophila embryos: Forces and kinetics', *Cell* 92(4), 547–557 (1998).

[Yam07] K. Yamaguchi, *(Nikon Corporation), Inmersion microscope objetive lens, US Patent # 7262922* (2007).

[YG99] P. Yeh and C. Gu. *Optics of Liquid Crystal Displays*. John Wiley & Sons, New York (1999).

[YL99] K. Yang and M. Lu, 'Nematic liquid crystal modes for si wafer-based reflective spatial light modulators', *Displays* 20, 211–219 (1999).